



National Library  
of Canada

Bibliothèque nationale  
du Canada

Canadian Theses Service

Service des thèses canadiennes

Ottawa, Canada  
K1A 0N4

## NOTICE

The quality of this microform is heavily dependent upon the quality of the original thesis submitted for microfilming. Every effort has been made to ensure the highest quality of reproduction possible.

If pages are missing, contact the university which granted the degree.

Some pages may have indistinct print especially if the original pages were typed with a poor typewriter ribbon or if the university sent us an inferior photocopy.

Reproduction in full or in part of this microform is governed by the Canadian Copyright Act, R.S.C. 1970, c. C-30, and subsequent amendments.

## AVIS

La qualité de cette microforme dépend grandement de la qualité de la thèse soumise au microfilmage. Nous avons tout fait pour assurer une qualité supérieure de reproduction.

S'il manque des pages, veuillez communiquer avec l'université qui a conféré le grade.

La qualité d'impression de certaines pages peut laisser à désirer, surtout si les pages originales ont été dactylographiées à l'aide d'un ruban usé ou si l'université nous a fait parvenir une photocopie de qualité inférieure.

La reproduction, même partielle, de cette microforme est soumise à la Loi canadienne sur le droit d'auteur, SRC 1970, c. C-30, et ses amendements subséquents.

THE UNIVERSITY OF ALBERTA

Characteristics of Auroral Surges in the Evening Sector

by

Stephen R. Kidd



A THESIS

SUBMITTED TO THE FACULTY OF GRADUATE STUDIES AND RESEARCH  
IN PARTIAL FULFILMENT OF THE REQUIREMENTS FOR THE DEGREE OF

MASTER OF SCIENCE

DEPARTMENT OF PHYSICS

EDMONTON, ALBERTA

FALL 1989



National Library  
of Canada

Bibliothèque nationale  
du Canada

Canadian Theses Service

Service des thèses canadiennes

Ottawa, Canada  
K1A 0N4

## NOTICE

The quality of this microform is heavily dependent upon the quality of the original thesis submitted for microfilming. Every effort has been made to ensure the highest quality of reproduction possible.

If pages are missing, contact the university which granted the degree.

Some pages may have indistinct print especially if the original pages were typed with a poor typewriter ribbon or if the university sent us an inferior photocopy.

Reproduction in full or in part of this microform is governed by the Canadian Copyright Act, R.S.C. 1970, c. C-30, and subsequent amendments.

## AVIS

La qualité de cette microforme dépend grandement de la qualité de la thèse soumise au microfilmage. Nous avons tout fait pour assurer une qualité supérieure de reproduction.

S'il manque des pages, veuillez communiquer avec l'université qui a conféré le grade.

La qualité d'impression de certaines pages peut laisser à désirer, surtout si les pages originales ont été dactylographiées à l'aide d'un ruban usé ou si l'université nous a fait parvenir une photocopie de qualité inférieure.

La reproduction, même partielle, de cette microforme est soumise à la Loi canadienne sur le droit d'auteur, SRC 1970, c. C-30, et ses amendements subséquents.

ISBN 0-315-60401-8

THE UNIVERSITY OF ALBERTA

RELEASE FORM

|                          |  |
|--------------------------|--|
| NAME OF AUTHOR           | Stephen R. Kidd  |
| TITLE OF THESIS          | Characteristics of Auroral Surges<br>in the Evening Sector |
| DEGREE                   | Master of Science  |
| YEAR THIS DEGREE GRANTED | FALL 1989  |

Permission is hereby granted to the UNIVERSITY OF ALBERTA to reproduce single copies of this thesis and to lend or sell such copies for private, scholarly or scientific research purposes only.

The author reserves other publication rights, and neither the thesis nor extensive extracts from it may be printed or otherwise reproduced without the author's written permission.

*Stephen R. Kidd.*

Stephen R. Kidd

Permanent Address : 8 Craighton Gardens

Milngavie

Glasgow G62 7AS

Scotland

Date *25<sup>th</sup> July 1989*

"There are strange things done in the midnight sun

By the men who moil for gold;

The Arctic trails have their secret trails

That would make your blood run cold;

The Northern Lights have seen queer sights,

But the queerest they ever did see ...."

From "The Cremation of Sam McGee" by

Robert Service.

THE UNIVERSITY OF ALBERTA  
FACULTY OF GRADUATE STUDIES AND RESEARCH

The undersigned certify that they have read, and recommended to the Faculty of Graduate Studies and Research for acceptance, a thesis entitled *Characteristics of Auroral Surges in the Evening Sector*, submitted by Stephen R. Kidd in partial fulfilment of the requirements for the degree of Master of Science in Physics.

.....  
Supervisor

.....  
.....  
.....

Date. June 19 1989

## ABSTRACT

The VIKING satellite mission of 1986, coordinated by Sweden, was aimed at studying magnetospheric processes. One of the experiments onboard this satellite was a pair of CCD cameras capable of imaging auroral emissions, with each camera having a fixed wavelength passband in the vacuum UV part of the spectrum. Image data analysed in this thesis were exclusively taken in the wavelength range of 1345 Å to 1900 Å, where auroral emissions in this range are predominantly from the LBH bands of  $N_2$ . The cameras had an effective exposure time of one second and images of the aurora occurring in the northern polar regions of the Earth were recorded typically once every 1 to 2 minutes (though occasionally images were acquired as rapidly as once every 20 seconds).

After defining an auroral surge in terms of the VIKING image data, a comparison was made between surges falling under this definition, and auroral forms previously defined as surges in terms of ground based magnetic records. Image data were analysed in two independent sets, each involving data from 50 orbits of the satellite, and a statistical survey of surges occurring in the evening sector of the auroral oval was carried out for each data set. Results of this survey showed that the most probable zone in which surges were found was 2300-2400 MLT and that this zone contained at least one surge  $\approx 15\%$  of the time that it was viewed. Images that showed multiple occurrences of surges led to the observation that  $\approx 35\%$  of surges occurred as individual forms. A few images showing a large number of surges occurring simultaneously were analysed by Fourier transform

techniques and periodicities were found with a wavelength of  $\approx 400$  km.

The results were interpreted within the framework of two different models of substorm dynamics : the Near Earth Neutral Line Model and the Boundary Layer Dynamics Model. While little in the way of firm conclusions could be drawn, both of these models were found to give plausible explanations of the results.



### **Acknowledgements**

I would like to take this opportunity to thank a number of people who have been directly involved with the work contained in this thesis. My supervisor, Dr. Gordon Rostoker, has provided advice and guidance with enthusiasm when I have needed it, as well as being my mentor.

SYSTEM, the principal software tool used to analyse VIKING satellite images, was written by Dr. Sandy Murphree in the Space Physics group at the University of Calgary. This group also gave me some much needed technical assistance in the preparation of the images reproduced in the colour plates found in this thesis.

Martin Connors provided numerous pieces of software and technical advice, as well as implementing several very useful additions to the SYSTEM software.

Finally, there are many more people who I would like to thank, who have given me support and encouragement during my stay in Canada, but time and space prevents them being recognised here.

## Table of Contents

| Chapter   | Page |
|---|------|
| 1 INTRODUCTION .....  | 1    |
| 1.1 Overview of the Solar Terrestrial Interaction .....       | 1    |
| 1.2 The Solar Wind .....                                      | 4    |
| 1.3 The Magnetosphere .....                                   | 7    |
| 1.4 Energy Transport into the Magnetosphere .....             | 10   |
| 1.5 Internal Regions of the Magnetosphere .....               | 12   |
| 1.6 Morphology of Magnetospheric Dynamics and Substorms ..... | 18   |
| 1.7 Theories of Substorm Dynamics .....                       | 28   |
| 1.8 The VIKING Satellite Project .....                        | 35   |
| 1.9 Objectives of Thesis .....                                | 36   |
| 2 DATA ACQUISITION .....                                      | 38   |
| 2.1 UV Camera Design .....                                    | 38   |
| 2.2 Camera Parameters .....                                   | 42   |
| 2.3 Camera Calibration Determination .....                    | 43   |
| 2.4 Data Collection and Storage .....                         | 44   |
| 3 ANALYSIS .....  | 47   |
| 3.1 Outline of Analysis .....                                 | 47   |
| 3.2 Definition of a Surge .....                               | 48   |
| 3.3 Compilation of Data on Surge Position and Intensity ..... | 56   |
| 3.4 Distribution of Surges with Magnetic Local Time .....     | 57   |
| 3.5 Absolute Levels of Surge Activity .....                   | 61   |
| 3.6 Surge Multiplicity .....                                  | 64   |
| 3.7 Fourier Analysis of Surge Multiplicity .....              | 70   |
| 3.8 Substorm Development .....                                | 77   |

|                  |  |     |
|------------------|--|-----|
| 4                | DISCUSSION AND CONCLUSIONS .....               | 83  |
| 4.1              | Summary of Results .....                       | 83  |
| 4.2              | Discussion of Surge Multiplicity .....         | 84  |
| 4.3              | Discussion of the Distribution of Surges ..... | 94  |
| 4.4              | General Comments on Substorm Development ..... | 99  |
| 4.5              | Concluding Remarks .....                       | 100 |
| REFERENCES ..... |  | 103 |
| APPENDIX I       | Glossary and Definitions .....                 | 107 |
| APPENDIX II      | MHD Equations .....                            | 112 |
| APPENDIX III     | 2-D Spatial Fourier Transforms .....           | 118 |

## **List of Tables**

| <b>Table</b>  | <b>Page</b> |
|---|-------------|
| 1.1 Mariner 2 Measurements of the Solar Wind .....            | 6           |
| 3.1 Summary of Surge Multiplicity Analysis .....              | 66          |
| 3.2 Summary of Fourier Analysis .....                         | 76          |
| 4.1 Limits of the Kelvin-Helmholtz Instability Parameters ... | 92          |

## List of Figures

| Figure   | Page   |
|--|--------|
| 1.1 Large scale structure of the magnetosphere .....   | 2      |
| 1.2 Chapman - Ferraro current system .....   | 9      |
| 1.3 Magnetic field line topology for Dungey reconnection ....  | 11     |
| 1.4 Internal regions of the magnetosphere .....  | 13     |
| 1.5 The auroral oval .....   | 17     |
| 1.6 The Akasofu substorm development .....   | 21     |
| 1.7 All-sky camera and magnetogram signatures of a surge ...   | 25     |
| 1.8 Modelled ionospheric current systems of surges .....   | 26     |
| 1.9 Modelled latitude and longitude magnetic perturbations<br>associated with surges .....   | 27     |
| 1.10 Plasmoid formation and ejection .....   | 32     |
| 1.11 The Kelvin-Helmholtz scenario in the magnetosphere .....  | 34     |
| <br>2.1 Schematic of the VIKING camera .....   | <br>39 |
| <br>3.1 Magnetic signature corresponding to a surge seen<br>with VIKING .....  | <br>52 |
| 3.2 Ground based magnetic data for a surge detected by VIKING<br>that shows an apparent absence of a magnetic surge<br>signature ..... | 54     |
| 3.3 Ground based magnetic data that shows a magnetic surge<br>signature where no apparent surge was seen by VIKING ....                | 55     |
| 3.4 Raw histograms of surge distribution .....   | 58     |
| 3.5 Graphs of normalised and smoothed surge distribution ....  | 59     |

|       |   |     |
|-------|---|-----|
| 3.6   | Two dimensional histogram of surge distribution at<br>different surge threshold intensity levels .....              | 62  |
| 3.7   | Scatter plot of surge intensity versus MLT position .....   | 63  |
| 3.8   | Graphs of absolute levels of surge activity .....   | 65  |
| 3.9   | Histograms of surge multiplicity .....  | 67  |
| 3.10  | Histograms of surge multiplicity at threshold<br>levels of 200 DN and 220 DN for data set B .....                   | 68  |
| 3.11  | Histograms of surge multiplicity at threshold<br>levels of 240 DN and 255 DN for data set B .....                   | 69  |
| 3.12  | Diagram outline of a geometric transformation .....   | 71  |
| 3.13  | Plots of substorm development and AE records .....  | 78  |
| 3.14  | Plots of substorm development and AE records .....  | 79  |
| 3.15  | Two dimensional histogram showing maximum distance<br>moved by surges as a function of time .....                   | 82  |
| 4.1   | Poleward steps of the westward electrojet .....   | 86  |
| 4.2   | Plots of Tsyganenko model field line tracing into<br>the magnetotail .....  | 88  |
| 4.3   | Geometry of the mapping model .....   | 90  |
| 4.4   | Plot of neutral sheet crossings vs MLT for field lines<br>originating from the poleward edge of the auroral oval .. | 91  |
| III.1 | Arrangement of 2-D Fourier transform data .....   | 123 |

## List of Plates

| Plate   | Page |
|---|------|
| 2.1 .....   | 46   |
| 2.1(a) Sample VIKING Image  |      |
| 2.1(b) Orientation of VIKING image  |      |
| 2.1(c) VIKING surge with no magnetic signature                                  |      |
| 2.1(d) VIKING surge with no magnetic signature                                  |      |
| 3.1 .....   | 53   |
| 3.1(a) Colocation of a VIKING surge with a ground<br>based magnetic observatory |      |
| 3.1(b) Colocation of a VIKING surge with a ground<br>based magnetic observatory |      |
| 3.1(c) Magnetic surge signature with no accompanying<br>VIKING surge            |      |
| 3.1(d) Magnetic surge signature with no accompanying<br>VIKING surge signature  |      |
| 3.2 .....   | 75   |
| 3.2(a) Example of surge multiplicity  |      |
| 3.2(b) Example of surge multiplicity  |      |
| 3.2(c) Geometrically transformed sub-image                                      |      |
| 3.2(d) Two dimensional spatial Fourier transform of<br>sub-image                |      |

## 1 : INTRODUCTION

### 1.1 : Overview of the Solar-terrestrial Interaction

The magnetic field of the Earth, implied from observations of the field on and close to its surface, is predominantly dipolar in form, with the axis of the dipole not colinear with the rotation axis, but at an angle of  $\approx 11^\circ$  to it. (There are other higher order multipole components to the internal field, but these contribute little to the total field.) However, the dipolar shape of the Earth's field does not extend to infinity and at distances beyond  $\approx$  four Earth radii ( $R_E$ ) the shape of the magnetic field is modified considerably by the presence of the *solar wind*. This wind consists of a tenuous magnetised plasma of electrons and protons that are streaming away from the Sun in all directions with plasma characteristics that determine the wind to be both supersonic and super-Alfvénic. (see Appendix I for definitions of these terms.)

When this supersonic and super-Alfvénic flow encounters the Earth's magnetic field (which is essentially static), a standing shock wave on the Sunward side of the Earth, called the *bow shock*, is set up. Behind it, the Earth's field is drawn out into a long tail like structure called the *magnetotail*, as shown in figure 1.1. This figure shows roughly the cavity to which the Earth's magnetic field is confined (though it is thought that some field lines, particularly from the polar cusps, "leak out" into the solar wind). The term



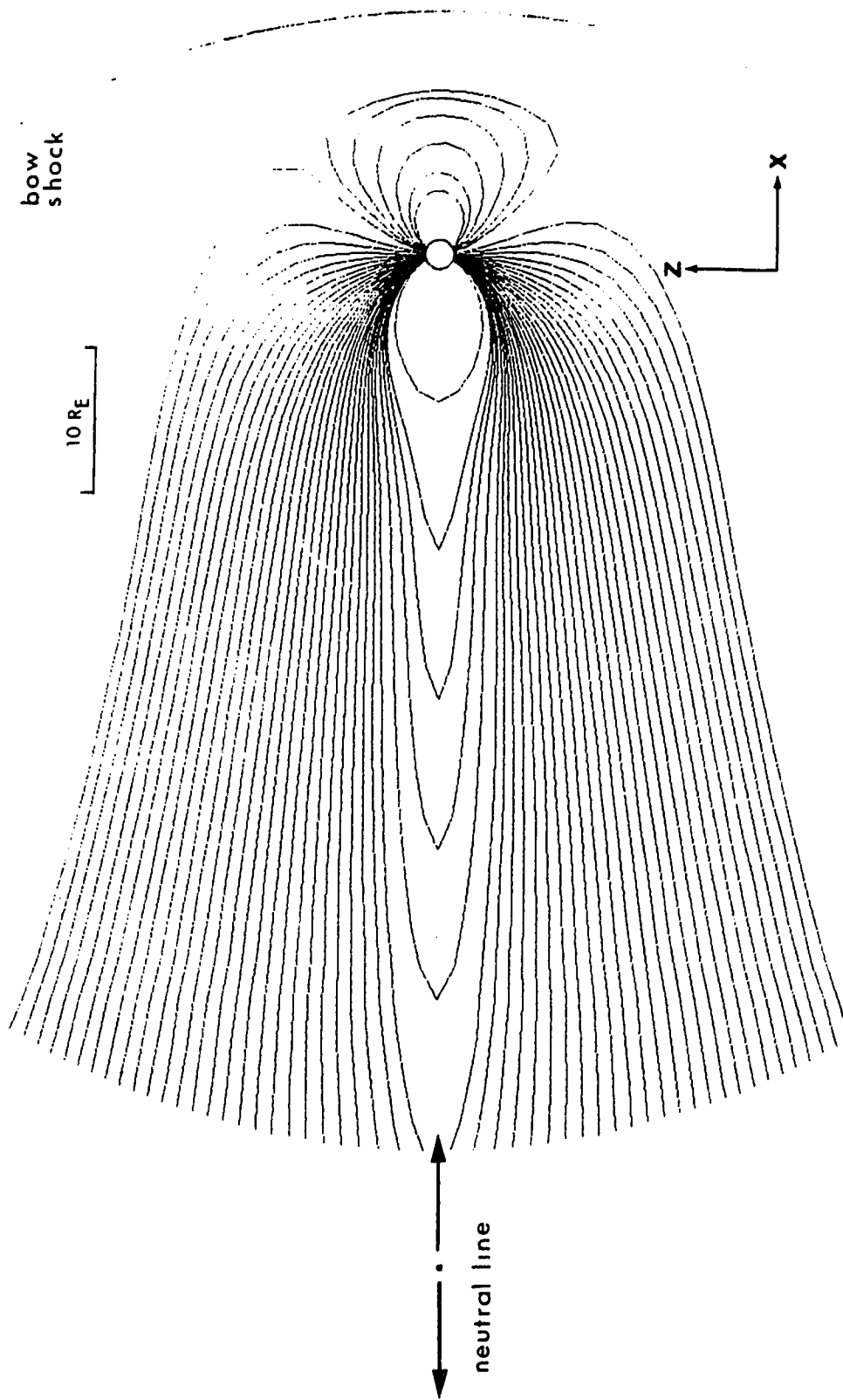


Figure 1.1 : The bow shock and the shape of the Earth's magnetic field, as determined from the Tsyanenko (1987) model, plotted in the XZ plane of GSM coordinates. The flaring away from the neutral line of magnetic field lines originating at high geomagnetic latitudes is an artefact of the Tsyanenko model.

applied to the volume and contents of this cavity is the *magnetosphere*. The coordinate system used in figure 1.1 is called the Geocentric Solar Magnetospheric system, referred to hereafter as GSM. (See Appendix I for definitions of coordinate systems used.)

The coupling of the solar wind to the magnetosphere and the coupling among various internal regions within the magnetosphere is responsible for a wide variety of geomagnetic phenomena detected in the vicinity of the Earth. There are occasions when the plasma processes taking place in the magnetosphere give rise to large magnitude geomagnetic disturbances and visible aurora. When these events occur, they can have noticeable effects on man-made systems. Radio wave communications can be disrupted because of ionospheric disturbances and electrical power distribution networks can suffer surges causing them to fail.

The complexity of the solar-terrestrial interaction is such that decades of research have not yet produced a unified model for all the interactions and processes that have so far been observed to take place. Problems in analysing processes and characteristics of the magnetosphere have been exacerbated because there has been no way to reliably remotely sense all of the different regions of the magnetosphere. With new and ambitious research projects planned for the near future, including attempts to remotely sense the magnetosphere by imaging techniques (e.g. utilising neutral oxygen

atoms, as described by Roelof, 1987), perhaps it will not be long before the puzzle is solved.

## 1.2 : The Solar Wind

The idea that particle emissions from the Sun propagate through the interplanetary medium to the Earth and that they might be associated with auroral displays is centuries old. Even when the first theories of the magnetosphere were proposed by Chapman and Ferraro (1932), it was envisaged that solar emissions only reached the Earth intermittently. Biermann (1956) is credited with developing the notion that the solar wind flowed continuously, based on observations of comets, and this theory was then verified by satellite measurements. These measurements not only showed a continuously flowing wind, but also that its flow was supersonic and super-Alfvénic (which settled a division in the scientific community of the time as to the nature of the flow).

Current theories of the solar wind suggest that the wind is generated by the outer layer of the Sun being continuously and rapidly expelled into surrounding space. This process is not yet fully understood, but it has been shown by Parker (1963) that the combination of the gravitational field of the Sun and pressure gradients close to its 'surface' provide a choking mechanism which results in mass being accelerated away from the Sun. Once started on

its journey, the solar wind flows out from the Sun in all directions, carrying with it, the magnetic field associated with the solar corona. This magnetic field of the solar wind is termed the Interplanetary Magnetic Field (IMF). The solar wind flows out through the solar system, enveloping all of the planets as it goes and carrying the IMF embedded within it. Large scale disturbances on the Sun, often occurring in regions of sunspot activity, cause large disturbances in the particle and field properties of the solar wind. What actually causes these disturbances, whether it be solar flares, prominences or coronal holes, is not yet agreed upon (Hundhausen, 1989), but when the disturbances propagate and are carried by the solar wind and interact with the magnetosphere, they can induce sizeable increases in the level of geomagnetic activity.

Table 1.1 gives typical values and ranges for a number of solar wind parameters, taken from Neugebauer and Snyder (1966). The range of values quoted is the nominal range and not the extreme range, for example,  $B$  has been measured as high as 100 nT and  $v$  as fast as 2000 km/s but virtually all of the time, the flow velocity is fast enough that it is both supersonic and super-Alfvénic.

| Table 1.1 : Mariner 2 Measurements of the Solar Wind |        |                             |   |
|--|--------|-----------------------------|---|
| Parameter  | Symbol | Typical Value               | Usual Range                               |
| Velocity   | $v$    | 500 km/s                    | 250 - 800 km/s                            |
| Magnetic Field                                       | $B$    | 5 nT                        | 1 - 20 nT                                 |
| Density  | $n$    | $7 \text{ cm}^{-3}$         | $2 - 10 \text{ cm}^{-3}$                  |
| Electron Temp. *                                     | $T_e$  | $2 \times 10^5 \text{ K}$   |   |
| Proton Temp.   | $T_p$  | $1.5 \times 10^5 \text{ K}$ | $3 \times 10^4 - 6 \times 10^6 \text{ K}$ |

\* Taken from Brandt, 1970.

If certain plasma characteristic parameters, such as the electron and ion gyroradii and the collision frequency, are computed from the data in table 1.1, it becomes evident that the interaction of the solar wind plasma with the Earth's environment cannot be treated by looking only at particle collisions. Both the solar wind plasma and the plasma inside the magnetosphere can be treated as magnetised fluids and so, in principle, a magnetohydrodynamic (MHD) description of the interaction between the solar wind and the magnetosphere should be used. Appendix II outlines a derivation of the MHD equations and also provides a commentary on their range of validity. In addition to the MHD fluid description of the interaction, there are wave-wave and wave-particle interactions which perform important roles in the creation of the bow shock on the sunward side of the magnetosphere.

### 1.3 : The Magnetosphere

The magnetosphere is a large and complex system with many different plasma regimes, inside which, a diverse range of plasma processes are thought to occur. To understand all facets of its behaviour is not yet possible, nor is it likely that a such a complete description of the magnetosphere is possible. In order to get an understanding of some of the global properties of the magnetosphere, some basic physics can be introduced as follows.

The surface of the magnetosphere, termed the *magnetopause*, represents the boundary between the solar wind and the region of space occupied by the Earth's magnetic field and is the surface of pressure balance between them. An equation relating the parameters of magnetospheric plasma and fields to those of the solar wind can readily be developed and following an approach used by Fairfield (1987), equating the total pressures on each side of the magnetopause leads to

$$\left[ K \rho v^2 \sin^2 \vartheta + n k T + \frac{B^2}{2\mu_0} \right]_{sw} = \left[ n k T + \frac{B^2}{2\mu_0} \right]_{mag} \quad (\text{Eqn 1.1})$$

where  $K$  is a constant describing the transfer of momentum from the solar wind to the magnetosphere ( $K=2$  for elastic and  $K=1$  for inelastic collisions),  $\rho$  is the mass density of the solar wind,  $\vartheta$  is the angle between the solar wind velocity and the tangent to the magnetopause,  $n$

is the plasma number density,  $T$  is the sum of plasma electron and proton temperatures,  $B$  is the magnetic field,  $k$  is Boltzmann's constant and  $\mu_0$  is the permeability of free space.

This equation can be used in a number of ways : it can be used to estimate the location of the magnetopause on the dayside of the Earth to first order if,  $B_{\text{mag}}$  is assumed to be the sum of the dipolar field originating from Earth and the field produced by the Chapman Ferraro currents (see below), and suitable values for the other parameters are used; it can be used to describe in a semi-quantitative way, the flaring of the magnetotail; and it makes semi-quantitative predictions of the effect of changes in solar wind pressure on the magnetosphere.

The dipole field of the Earth is distorted because of the existence of circulating electric currents flowing on the magnetopause. The magnetic field produced by these *Chapman-Ferraro currents* is superposed on the dipole field and the resulting magnetotail field is obtained. Production of the Chapman-Ferraro currents is governed by the equation

$$J_{\perp} = \frac{B \times \nabla P}{B^2} \quad (\text{Eqn 1.2})$$

where  $\nabla P$  is the pressure gradient. A sketch showing the configuration of Chapman-Ferraro currents is shown in figure 1.2.

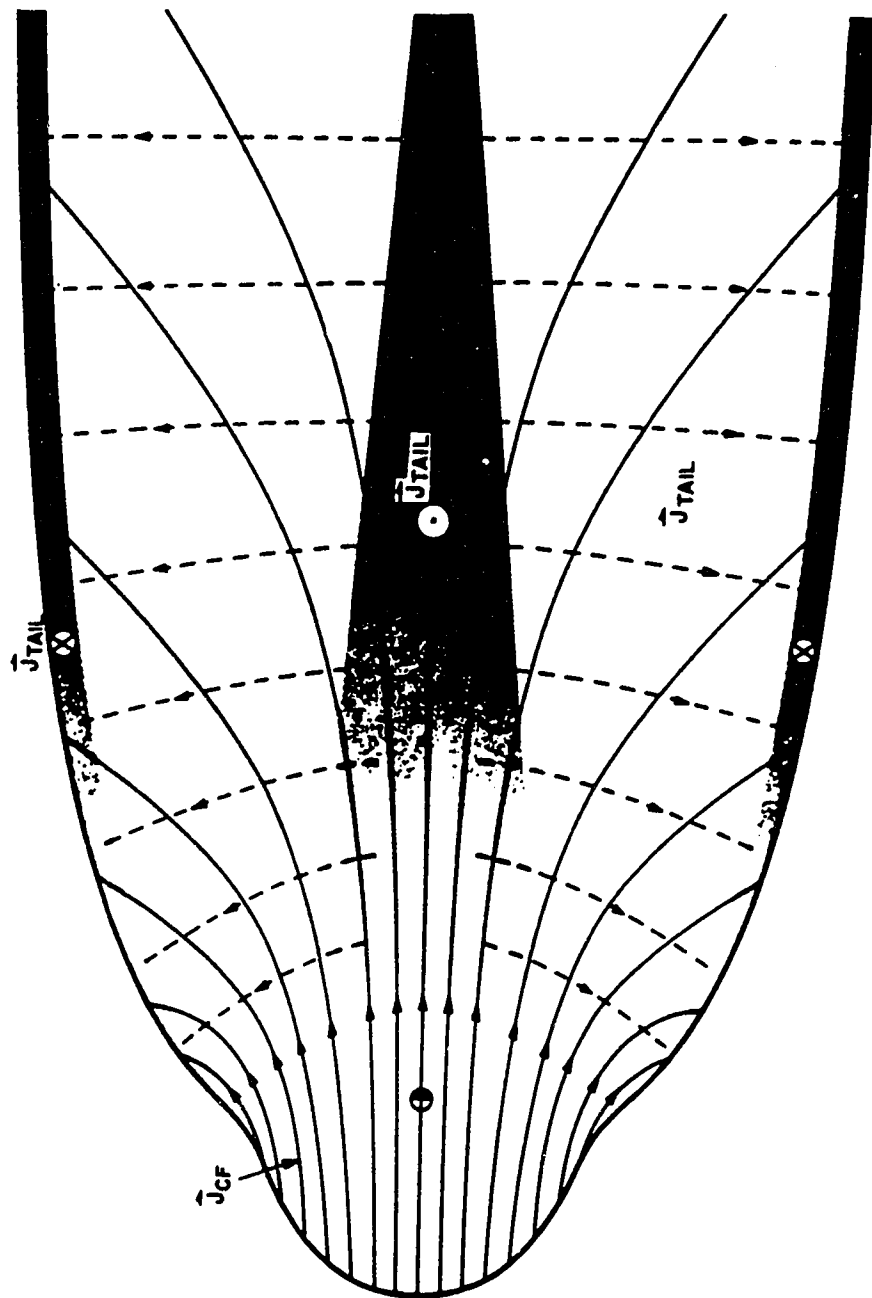


Figure 1.2 : The Chapman Ferraro current system on the magnetopause.  
From Axford et al. (1965).



#### 1.4 : Energy Transport into the Magnetosphere

Both energy and mass are transported across the magnetopause and the two principal mechanisms by which this happens (except for direct entry of particles into the polar cusps) are magnetic reconnection (first proposed for the magnetosphere by Dungey, 1961) and viscous magnetic fluid interaction (Axford and Hines, 1961). Miura (1984) has developed numerical simulations of the magnetic viscous interaction, and has shown that momentum transport can occur across the magnetopause. However, this fluid interaction does not take into account turbulence and does not allow for mass transport. It is now thought that magnetic reconnection is responsible for transporting roughly 90 % of the energy acquired by the magnetosphere (from the solar wind) across the magnetopause and that the viscous fluid interaction is responsible for the remainder (Baumjohann and Haerendel, 1986). Observations made by satellites crossing the dayside magnetopause have found little evidence though to support continuous reconnection over large areas of the dayside magnetopause, and so a modified theory of reconnection has been proposed by Russell and Elphic (1979), whereby dayside reconnection takes place through many localised events termed flux transfer events (FTE's).

On the nightside, magnetic reconnection is also thought to take place in the equatorial plane of the magnetotail along what is termed a neutral, or X line. Dungey (1961) considers the neutral line to be

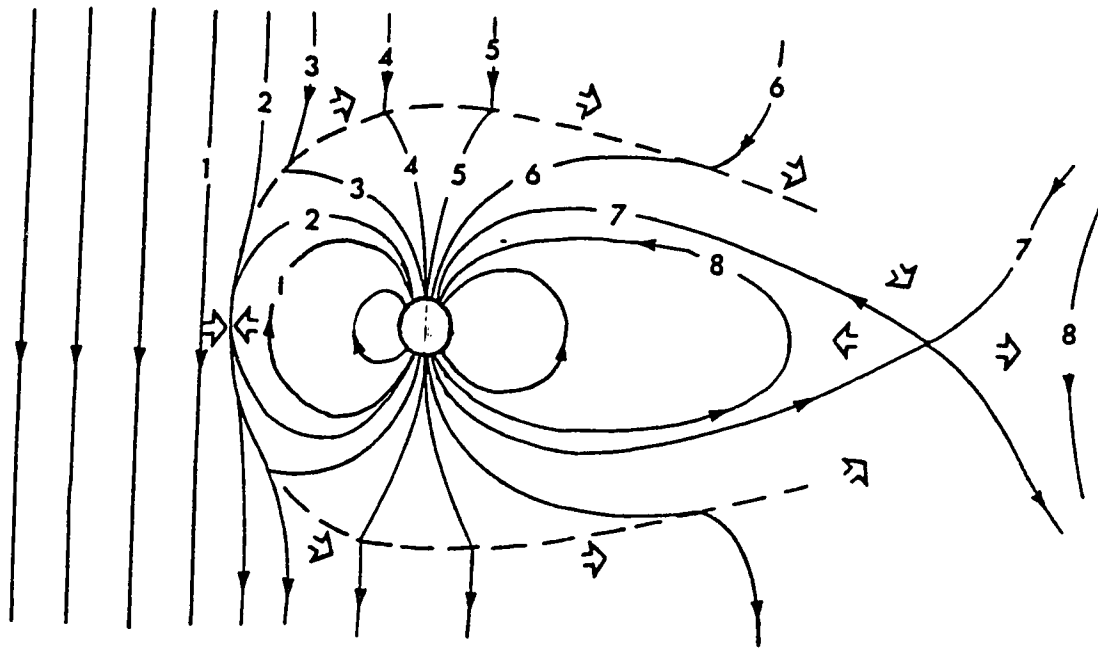


Figure 1.3 : The topology of the magnetic field reconnection at both the day and night side of the magnetosphere, from Dungey (1961).

the separator line between two regions, one containing closed field lines originating on the Earth, and the other containing field lines that do not close anywhere near the Earth. Figure 1.3 shows the topology of the field lines when the IMF has a southward component.

The entry of energy into the magnetotail is enhanced when the  $B_z$  component of the IMF is aligned anti-parallel to the Earth's magnetic field. When the  $B_z$  component turns northward and is aligned with the Earth's field, the entry of solar wind energy is reduced, often accompanied by a rapid release of energy from the magnetotail into the atmosphere (though northward turnings of the IMF are not uniquely responsible for this triggering). Such an episode of energy deposition from the magnetotail to the ionosphere is termed a *substorm expansive phase* and it is during these storms that large magnetic disturbances and intense aurora are frequently recorded.

### 1.5 : Internal Regions of the Magnetosphere

Inside the magnetopause, the magnetosphere can be subdivided into many regions, each region reflecting different plasma characteristics. Figure 1.4 shows one such subdivision of the magnetosphere due to Rostoker (1989) and shows the bulk flow of plasma in the different regions. Of the numerous different regions, only the Central Plasma Sheet (CPS) and the Low Latitude Boundary Layer (LLBL) will be discussed here in any detail, these being the regions most relevant to

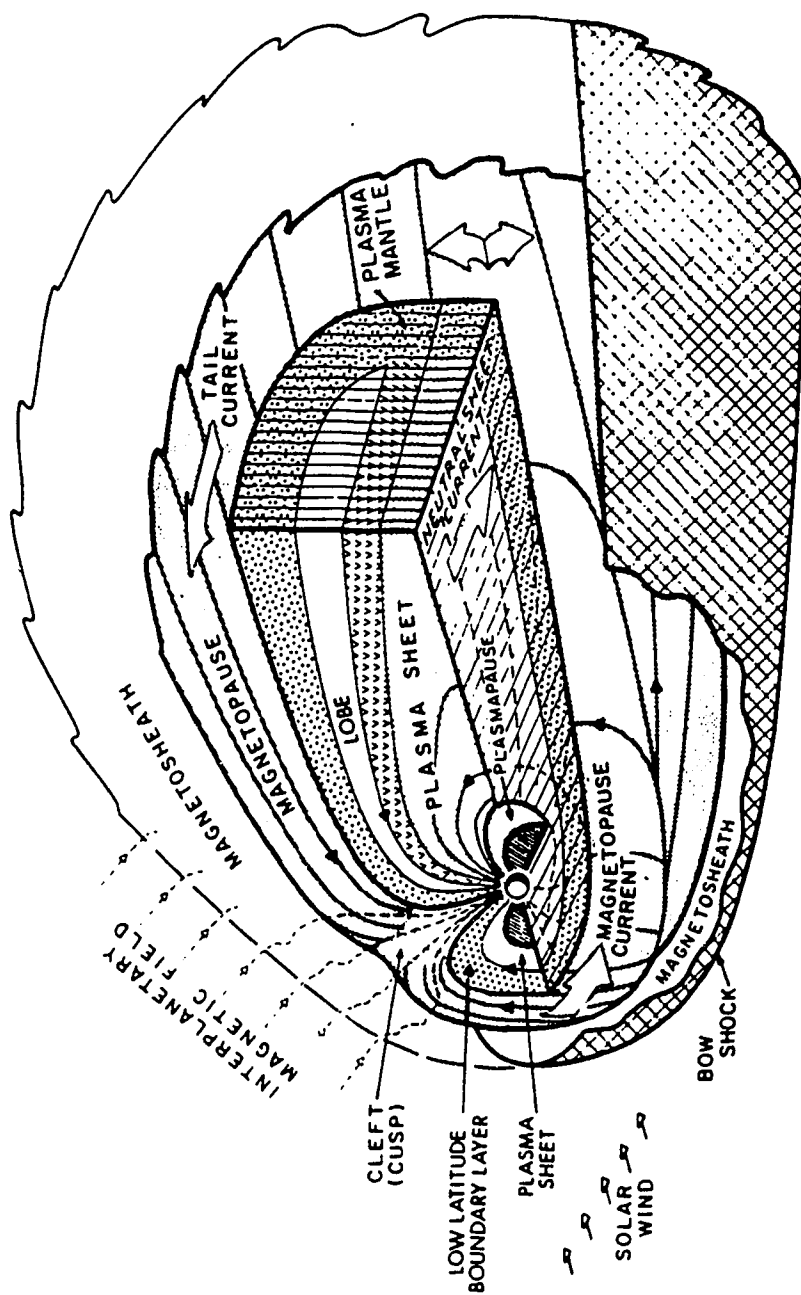


Figure 1.4 : Internal regions of the magnetosphere, after Rostoker (1989).

the research conducted.

The CPS is a region containing 'warm' (1 to 10 KeV electrons and protons) isotropic plasma drifting towards the Earth at a few tens of km/s. This approximately constant drift results from having an approximate balance of forces on the plasma. For an ideal MHD plasma (described in appendix II), this can be expressed as

$$\nabla P \approx J \times B \quad (\text{Eqn 1.3})$$

where  $\nabla P$  is the pressure gradient encountered as the Earth is approached,  $J$  is the dawn to dusk cross tail current and  $B$  is the magnetic field. As the plasma sheet particles move Earthward, they are influenced by electric field,  $\nabla B$ , and curvature guiding centre drifts which are summarised in equation 1.4, where  $v_{\perp}$  and  $v_{\parallel}$  are the respective particle velocities perpendicular and parallel to the magnetic field,  $m$  and  $q$  are the charge and mass of the particle species respectively,  $E$  is the electric field and  $R$  is the radius of curvature of the magnetic field in the region of the particle drifts.

$$V_{(g)} = \frac{\frac{1}{2} m v_{\perp}^2}{q B^3} B \times \nabla B + \frac{m v_{\parallel}^2}{q B^2} B \times \left[ \frac{R}{R^2} \right] + \frac{E \times B}{B^2} \quad (\text{Eqn 1.4})$$

In regions where the radius of curvature of the magnetic field is not known, but the field is known (or assumed) to be curl free, then after applying some vector identities equation 1.4 becomes

$$V_{(g)} = \frac{m}{2 q B^3} \left[ v_{\perp}^2 B \times \nabla B + 2 v_{\parallel} B \times (B \cdot \nabla) B \right] + \frac{E \times B}{B^2} \quad (\text{Eqn 1.5})$$

While equation 1.5 is strictly only applicable in regions where no currents are flowing, it shows that the guiding centres of energetic electrons will drift to the dawn side of the magnetosphere as they approach the Earth, and the guiding centres of energetic protons will drift to the dusk side. While the guiding centres of ions and electrons drift approximately parallel to the magnetotail equatorial plane in accordance with equation 1.5, the particles themselves oscillate on magnetic field lines above and below the midplane of the magnetotail. As the particles approach the Earth on these field lines, they enter a region of higher magnetic field strength. If the ratio of  $v_{\parallel}$  to  $v_{\perp}$  is small (this ratio is normally quoted in terms of the pitch angle  $\alpha$ , where  $\alpha = \tan^{-1}(v_{\parallel}/v_{\perp})$ ), then the particles will be reflected (mirrored) before they reach the ionosphere. Alternatively if the pitch angle is large enough, then the particles are in what is termed the *loss cone* and will precipitate into the auroral ionosphere.

In a plasma, the net result of the guiding centre motion and the particle gyrational motion about the guiding centre gives rise to a magnetisation current. For the plasma drifts and motion in the magnetotail, this results in the formation of what is known as the *ring current*. On the nightside of the magnetosphere, this current

resides in the CPS (at an average distance of  $\approx 4R_E$  though it can vary considerably from this) and on the dayside, the current closes to form a complete ring of current round the Earth.

The CPS is bounded at its high latitude edges by the Plasma Sheet Boundary Layer (PSBL), with the Low Latitude Boundary Layer bounding its flanks. The LLBL contains cold particles primarily of solar wind origin, drifting anti-sunward, perpendicular to  $B$  and with velocities of typically  $\approx 150$  km/s.

The visible auroras observed in the polar regions of the Earth are caused by particles that have pitch angles that allow them to reach the ionosphere before they are mirrored. This particle precipitation occurs along belts located round the magnetic north and south poles called *auroral ovals* (see figure 1.5). While particles are following field lines to the ionosphere, the electrons are accelerated and acquire energies, ranging from hundreds of eV to many tens of keV. In the distant magnetotail, energisation of the plasma population takes place by adiabatic contraction of earthward moving flux tubes. Closer to the Earth, precise details of the electron acceleration mechanism located between 1 and 2  $R_E$  (Mozer et al., 1977) are not known, but soliton waves, stochastic heating, electrostatic double layers and wave - particle interactions are all thought to contribute. When the electrons collide with the particles of the upper atmosphere (e.g. atomic oxygen and molecular nitrogen) excitation, followed by

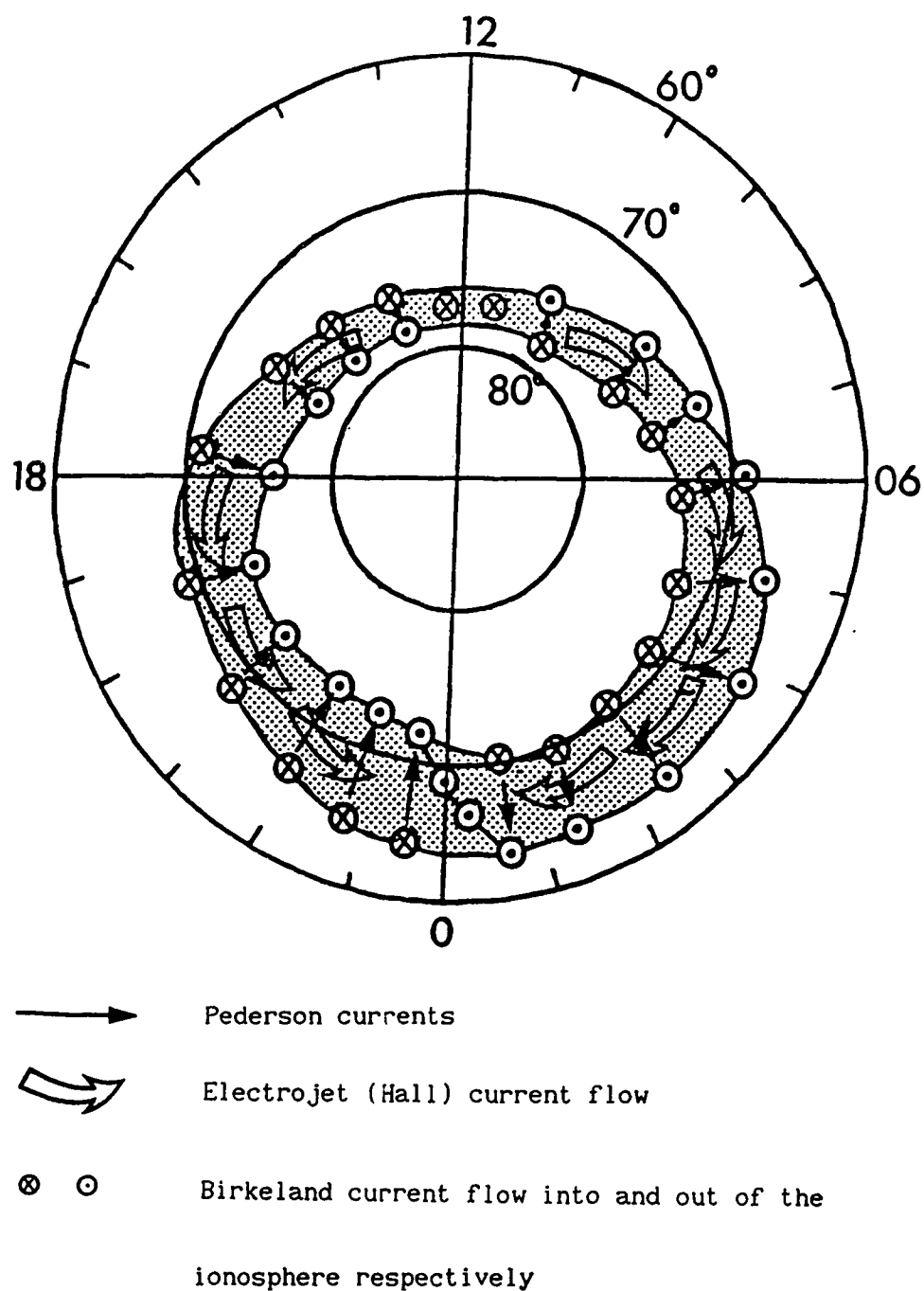


**Figure 1.5 :** Average position of the auroral oval, current flow into and out of the ionosphere and the electrojet current systems. The azimuthal coordinate is Magnetic Local Time and the radial coordinate is geomagnetic latitude. Modified from de Groot-Hedlin (1986).



relaxation causing photo emission, occurs. The wavelength range spanned by these emissions is considerable; from the far infra-red (IR) to the far ultra-violet (UV). Prominent optical emissions occur at 5577 Å (a green colour) corresponding to an electronic transition in atomic oxygen and at 6300 Å (red), also from atomic oxygen.

### 1.6 : Morphology of Magnetospheric Dynamics and Substorms

The magnetosphere behaves in a very similar manner to a windsock blowing in the wind : a change in the solar wind direction will cause the magnetosphere to move and align itself with the new solar wind direction. In addition to this motion, the midplane of the tail has oscillatory motion normal to the ecliptic plane as the Earth's dipole field precesses about the spin axis. Also, changes in the amount of flux contained inside the magnetotail can alter its cross section and the distance down tail of the neutral line (see figure 1.1). This additional flux in the magnetotail comes from the day side of the magnetosphere, so that the total amount of flux contained inside the magnetosphere remains constant. It is worth noting that the neutral line moves in the opposite sense from what might be expected due to changes in the flux contained in the magnetotail, e.g. an increase of flux will cause the neutral line to move Earthward. This occurs because the rate at which particles in the plasma mantle convect to the neutral sheet is dependent primarily on the electric field strength in the tail (though the rate is also affected to a much

smaller degree by the magnetic field). Increased electric field will cause this convection to take place more rapidly and because the particles carry the magnetic field with them (the frozen field characteristic discussed in appendix II), the position of the neutral line will then be closer to the Earth. Thus the boundaries shown in figure 1.4 are subject to continuous movement and may be difficult to discern at a particular time.

Historically, there has been considerable debate as to what constitutes a substorm, but there is now agreement on the main definitions and terminology used, as described by Rostoker et al. (1980, 1987.) A *substorm* represents a period of increased deposition of energy into the auroral ionosphere. In the cycle of energy being extracted from the solar wind and dissipated in the auroral ionosphere or returned to the solar wind, there appear to be two classes of processes at work. The *driven process* involves the redistribution of energy that is extracted from the solar wind and deposited in the ionosphere with no time lag between extraction and deposition except that due to the inherent inductance of the system. The *storage and release process* (often referred to as the *loading and unloading process*) involves the storage of energy from the solar wind as magnetic field energy by increasing currents flowing in the distant magnetotail. Some time later, this energy is deposited impulsively into the auroral oval. The triggering of the release of the stored energy often occurs when the IMF turns northward, but there may also

be internal magnetotail or ionospheric processes (c.f. Kan et al. 1988) which may initiate the release process. The time scale for the storage and release processes is typically a few minutes to an hour.

The first generalised picture of substorm development was due to Akasofu (1964). In this picture of a substorm, the substorm process was thought to represent a single episode of energy deposition into the ionosphere. *Onset* took place close to midnight magnetic local time (MLT, see appendix I for the definition of this coordinate) with the sudden brightening of an auroral form (or *auroral arc*) in the poleward portion of the auroral oval. After this so-called *auroral breakup*, the region that had brightened expanded westward across the evening sector to 1800 MLT during the *expansion phase*. The bright structure that moved in this manner was termed a *Westward Travelling Surge* (WTS). The *recovery phase* was the period of time when activity in the oval subsided and the arcs began to drift equatorward. These events are shown pictorially in figure 1.6.

Now however, this picture of substorm development has changed. In the course of a single substorm, it is recognised that both the loading and unloading processes can, and do, occur repeatedly, providing multiple onsets within a substorm expansion phase. Commencement of the substorm is taken to occur when the auroral oval undergoes its first breakup, and the substorm is deemed to have finished when the level of activity due to driven processes subsides

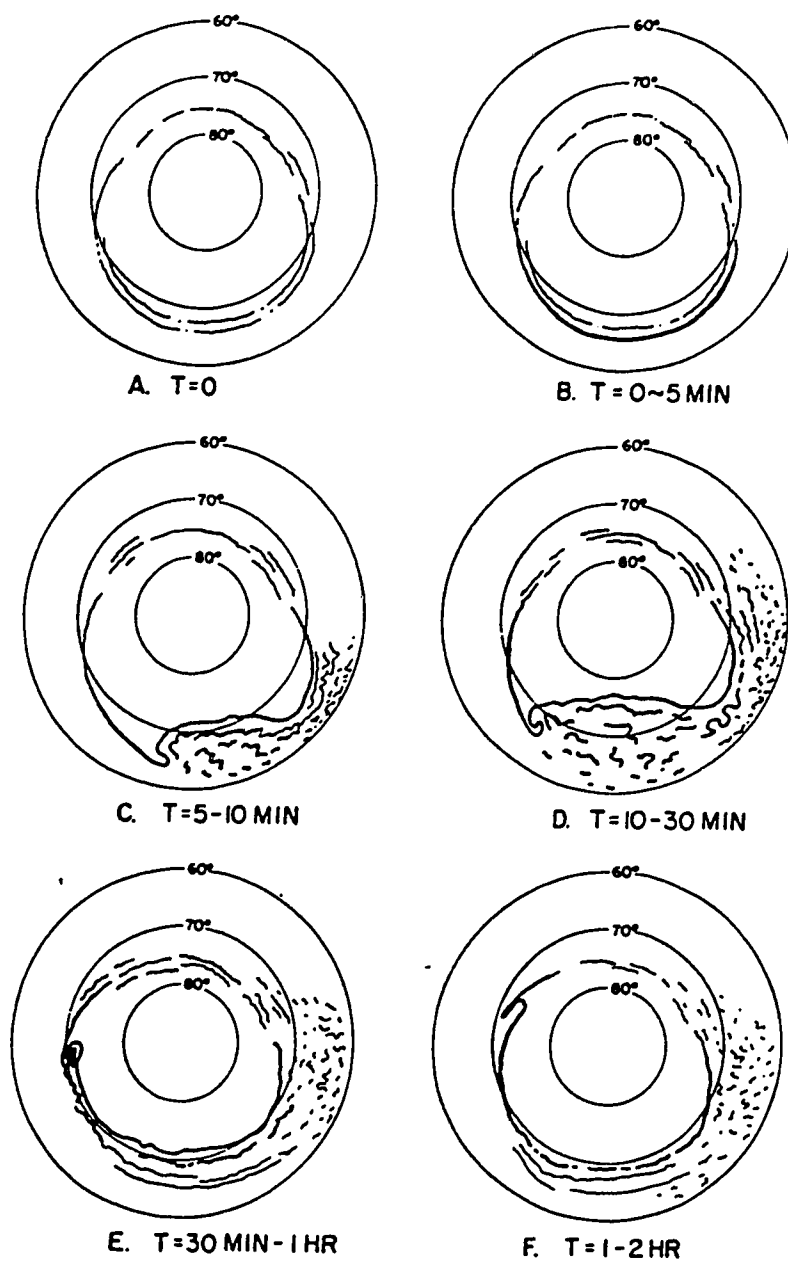


**Figure 1.6** : Substorm development as first envisaged by Akasofu (1964).

to that close to which it started from.

Both the driven and storage/release processes involve the transfer of energy from the magnetotail to the near Earth environment and this is achieved through the action of MHD waves and three dimensional current systems involving current flow parallel to magnetic field lines. The effects of the arrival of this energy close to the Earth have been studied using both all-sky camera and magnetometer networks spanning the auroral oval and adjacent regions. It is worthwhile to discuss briefly the nature of these observations and how they relate to the processes of energy deposition.

The driven process of a substorm manifests itself in a number of ways, of which the principal ones are increasing the magnitude of the ring current and increasing the current flowing in the *auroral electrojets* (shown in figure 1.5). These electrojets are Hall currents resulting from the electric field associated with the flow of direct (Pederson) current across the auroral oval, which is, in turn, linked to field aligned currents (termed *Birkeland currents*) originating in the magnetotail. The Hall effect results from a difference in mobility between the ions and electrons at the altitude of the Pederson currents ( $\approx 80$  km to  $\approx 160$  km), electrons being the more mobile charge carriers. The Hall current is then given by

$$\mathbf{J}_H = \vec{\sigma}_H \cdot \frac{\mathbf{B} \times \mathbf{E}_\perp}{B} \quad (\text{Eqn 1.6})$$

where  $\vec{\sigma}_H$  is the Hall conductivity tensor and  $E_\perp$  is the perpendicular component (to the magnetic field  $B$ ) of the electric field responsible for driving the Pederson currents. The sense of the electrojet currents is eastward on the dusk (pre-midnight MLT) side of the oval and westward on the dawn side. The magnetic perturbation observed when the electrojet currents are increased can be readily worked out and is dependent on the location of the observation point with respect to the electrojets. The magnitude of this magnetic perturbation is not as large as one might initially think. The combined Pederson and Birkeland current systems have the approximate topology of a solenoid, so the magnetic perturbations produced by these current systems, and measured on the ground at high geomagnetic latitudes, will be small because the point of observation is external to the solenoidal configuration. At mid-latitudes though, the solenoidal configuration is not seen as such a good approximation and observations of FAC at mid-latitudes have been made by Clauer and McPherron (1983). At times of increased electrojet activity, there is increased particle precipitation into the auroral oval ionosphere. This precipitation causes the formation of *auroral arcs* - longitudinally aligned and latitudinally confined areas of enhanced optical emissions.

With regard to signatures of the storage/release processes that occur during a substorm, it is the release process that is easily recognisable on the Earth. The key signature that the energy release process is taking place is termed a (*auroral*) *surge*. Optically, this

is seen as a localised, explosive intensification of auroral luminosity occurring at the poleward edge of the oval. The intensification of the surge is associated with an increased upward (i.e. out of the ionosphere) field aligned current (FAC). The FAC spans the interface region between the westward and eastward electrojets, termed the *Harang discontinuity*. The discontinuity in Hall current flow and the intense FAC combine to give a distinctive magnetic signature at suitably located magnetic observatories, as described by Rostoker and Hughes (1979). An example of a magnetogram showing the characteristic surge magnetic signature is shown in figure 1.7, along with an accompanying all-sky camera image. Figure 1.8 shows the ionospheric current systems involved in a surge and figure 1.9 gives the longitude and latitude profiles of the magnetic perturbations as the surge is traversed.

The scale size of a surge and how many surges can occur at any one time have been subject to much debate and revision during the last two decades. Currently, there is still no universally accepted definition of a surge. The reason for the debate is primarily because of the advent of satellite global imaging of the aurora. While this occurred a number of years ago, there has still not been a complete integration of satellite and ground based data. Until this happens, definitions of auroral features like surges will continue to be debated. However, the broad trend in defining surges has been to move away from the Akasofu surge (which was defined before satellite images

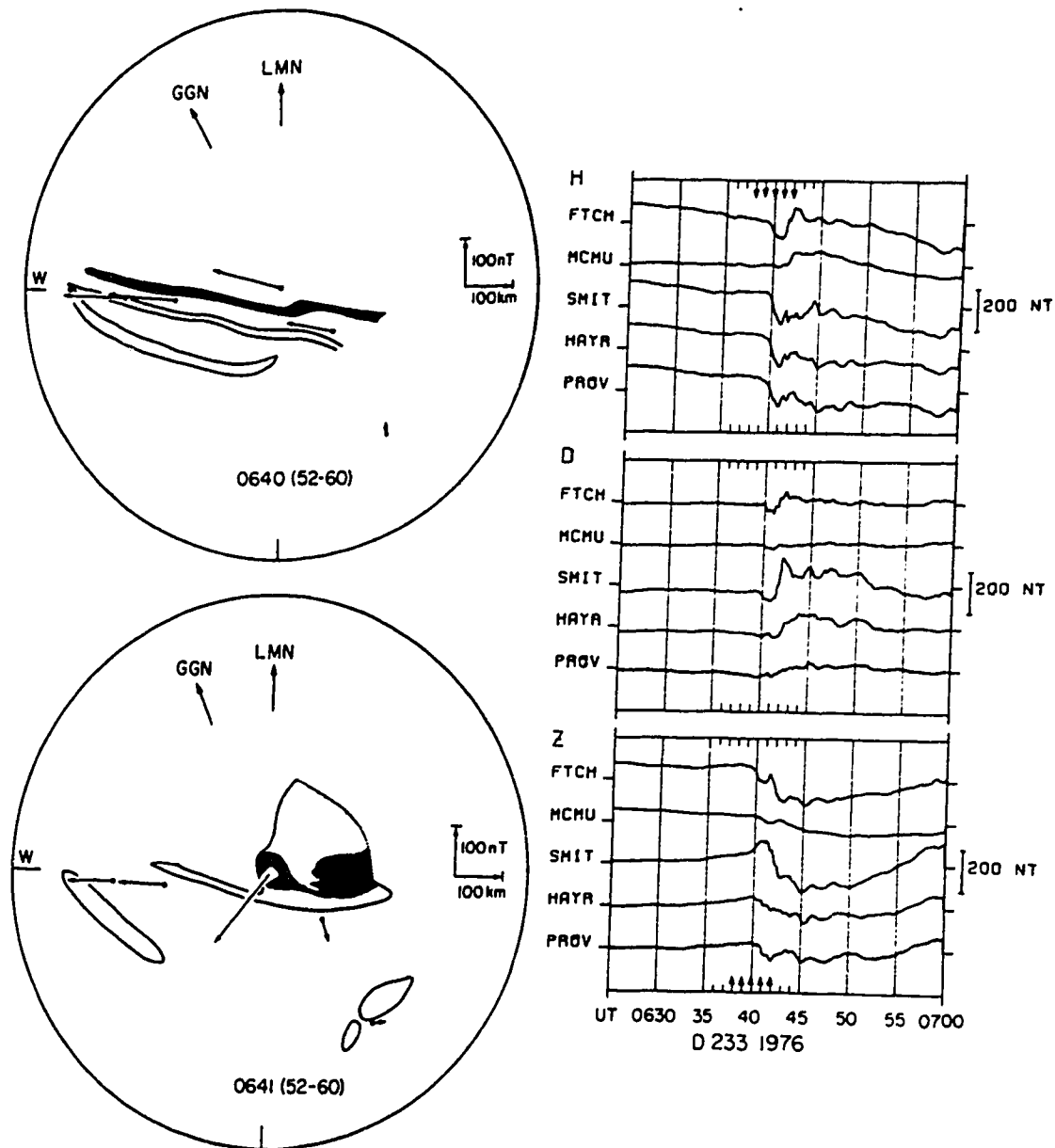


**Figure 1.7** : Two all-sky camera images of a surge and the magnetograms of the same event, from Kawasaki and Rostoker (1979). The magnetometer stations are located approximately on one meridian line of geographic longitude. The all-sky camera data is from station SMIT and shows the expansion and intensification of an auroral arc. (Intense regions of arcs are depicted with dark shading.) Magnetic field vectors, local magnetic north (LMN) and geomagnetic north (GGN) are also indicated.



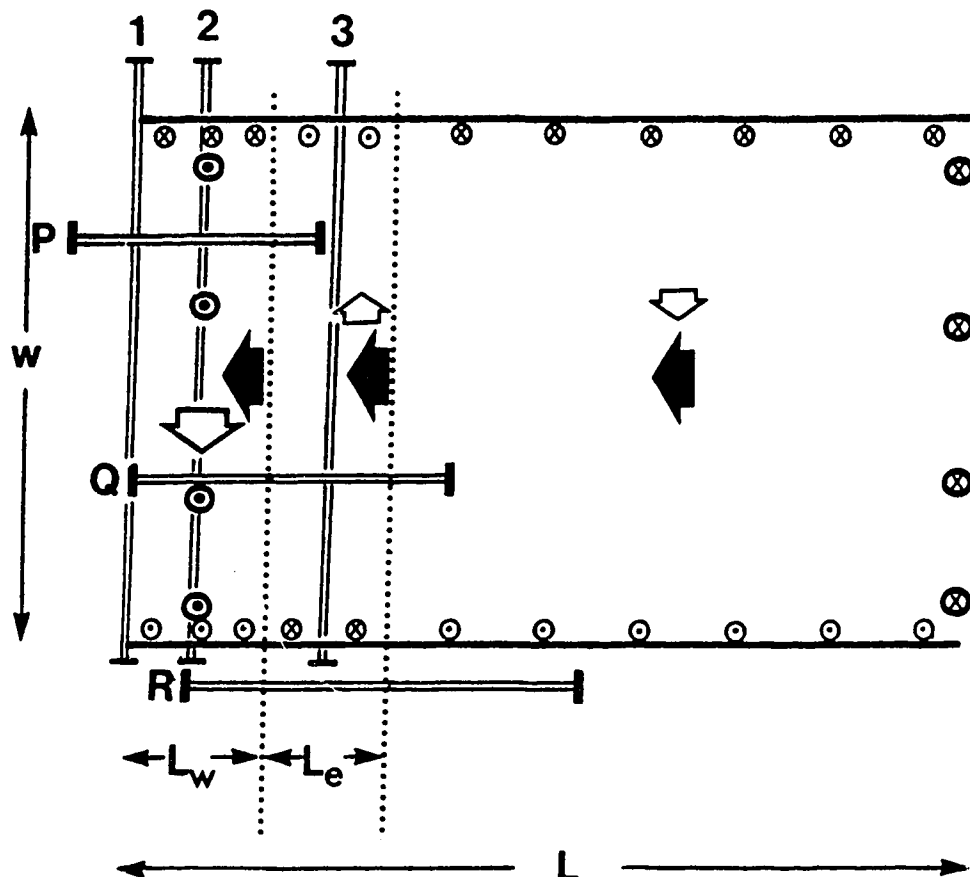
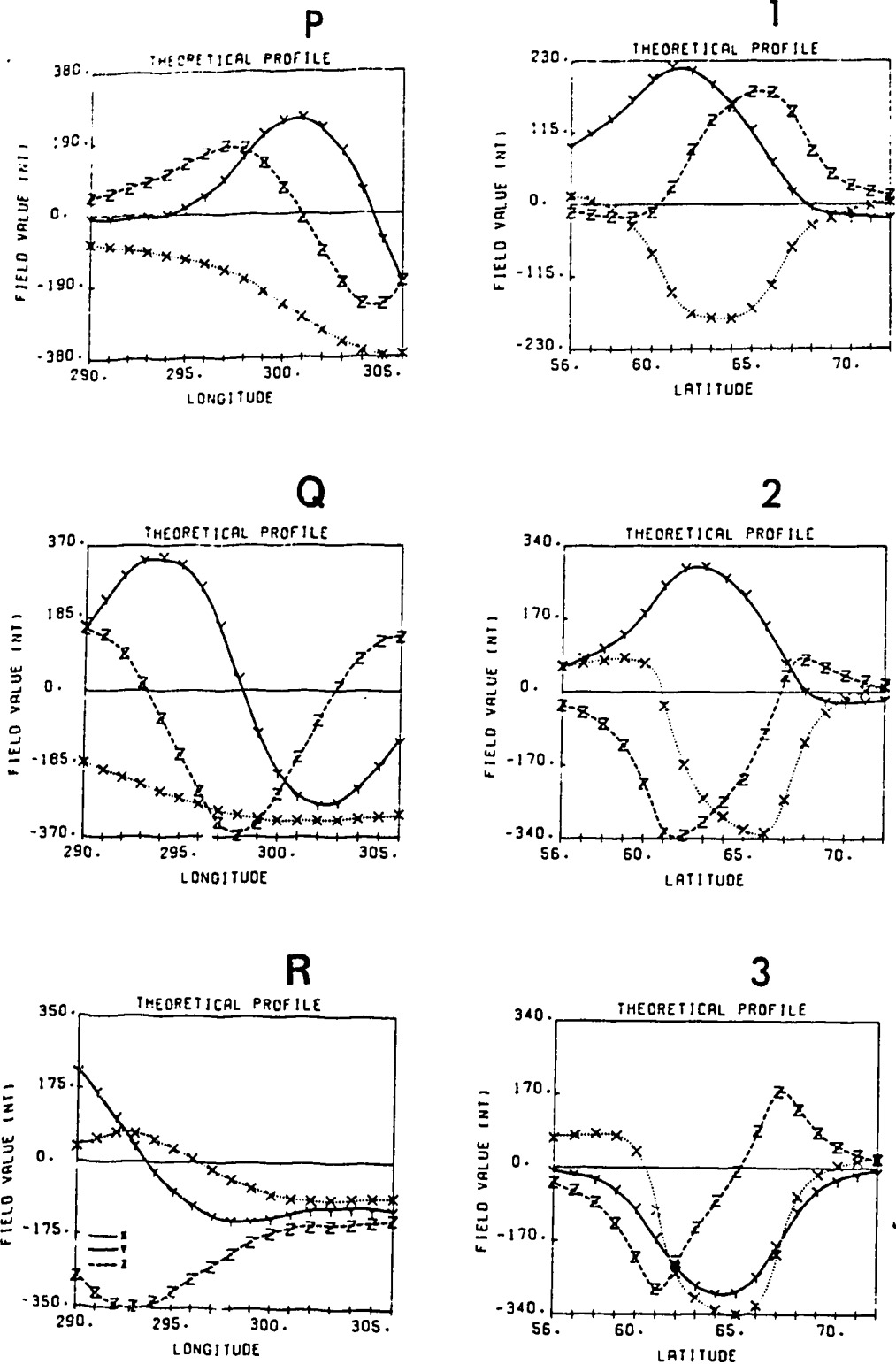


Figure 1.8 : Modelled ionospheric current systems associated with a surge (Tighe and Rostoker 1981).  $L$  and  $W$  are the length and width of the westward electrojet. Solid arrows represent the westward electrojet current. Intense upward current, associated with precipitating electrons is located along the profile line labelled 2.  $L_w$  is the width of a region of equatorward current flow at the 'head' of the surge and  $L_e$  is the width of poleward current flow behind the surge head.



**Figure 1.9 :** Profiles of magnetic perturbations of a surge based on the current systems shown in figure 1.7, (Tighe and Rostoker 1981)

existed) towards smaller scale sizes and shorter time scales. The "Akasofu surge" was a large monolithic structure with a scale size in excess of several hundred km that formed close to midnight (MLT). It then propagated westward for up to thousands of km (the so-called westward travelling surge) and represented the western most boundary of expansive phase activity in the evening sector, as depicted in figure 1.5. The typical lifetime of a surge in this scenario was anywhere from 20 minutes to 2 hours. Satellite data now suggest that a more appropriate view of surges is that they are smaller scale structures, often with several occurring simultaneously and having lifetimes averaging several minutes. The problem of defining a surge in more detail is dealt with in § 3.2.

### 1.7 : Theories of Substorm Dynamics

While there is a growing consensus in the scientific community as to the general morphology of substorms and features of substorms, e.g. surges, there is still intense debate over a unified theory that explains all the features of substorms. Indeed, of the currently contending theories, none of them purport to explain all the phenomena associated with substorms, but rather they concentrate on a subset of substorm phenomena and data. However, because surges are thought to represent one of the principal mechanisms signalling the redistribution of stored magnetotail energy, their generation is a key feature of any substorm theory or model. Of equal importance to surge

generation for substorm models is a mapping of field lines from the different regions of the magnetotail to the ionosphere.

There are four partial theories of substorms that are under debate and scrutiny. The common names applied to these theories and their principal originators are the *Thermal Catastrophe Model* (Smith et al., 1986), the *Magnetosphere - Ionosphere Coupling Model* (Kan and Sun, 1985; Kan et al., 1988.) the *Near Earth Neutral Line Model* (Hones, 1984) and the *Boundary Layer Dynamics Model* (Rostoker and Eastman, 1987). With the exception of the Thermal Catastrophe model, each model is linked in some way to ionospheric processes or ionospheric signatures of magnetotail processes, so because the data for this thesis are images of the ionosphere, the thermal catastrophe model will not be discussed further. A brief description of remaining three models follows, with more details being given for the Boundary Layer Model, because it is in the context of this model that a discussion of the results shown in § 3 can most easily be made. The reader is referred to Rostoker (1989) for a more thorough discussion on the competing substorm theories.

#### 1) Magnetosphere - Ionosphere Coupling Model

Basically a numerical simulation of plasma wave propagation that is still under development, this model has yielded encouraging results regarding onset and subsidence of substorms and the generation of

surges.

The basis of the simulation is the modelling of Alfvén waves reflected between the ionosphere and the outer magnetosphere. The origin of the waves is presumed to be enhanced magnetospheric convection which occurs as the result of substorm processes. The waves then propagate along field lines to the ionosphere of each polar region of the Earth, where they are reflected. Electric fields and conductivity patterns in the ionosphere then determine the reflection and polarisation of the wave that will return to the outer magnetosphere. Reflection in the distant magnetosphere is then determined by whether or not the field line is open or closed.

#### ii) Near Earth Neutral Line Model

As discussed in §1.4, magnetic reconnection at a neutral line is thought to be one of the many processes occurring in the magnetosphere and the existence of a neutral line in the magnetotail is now generally agreed upon (c.f. Slavin et al., 1985).

Satellite measurements in the magnetotail of apparent anti-Earthward plasma flow, near the midplane of the tail, initiated the development of this model. To get such a flow of plasma, it was proposed that a second neutral line is formed close to the Earth at  $< 20 R_E$  and extending azimuthally only over a portion of the

magnetotail. As with the original neutral line, magnetic reconnection of field lines occurs at the near Earth neutral line, resulting in the jetting of plasma both Earthward and anti - Earthward. When enough field lines have been reconnected, a portion of the CPS then becomes magnetically isolated from both the Earth and the solar wind. Such a configuration has been termed a magnetic island or plasmoid. When the last field line required to form the plasmoid closes, the plasmoid is then free to move down tail with a velocity of  $\approx 5 - 10 R_E / \text{minute}$ , forced by plasma pressure gradients and the lobe magnetic field. The onset of reconnection of lobe field lines marks the onset of the expansive phase of the substorm. Schematically, this sequence of events is shown in figure 1.10.

### iii) Boundary Layer Dynamics Model

As with the Near Earth Neutral Line Model, the Boundary Layer Dynamics model (BLD model) addresses magnetic reconnection during the period of substorm activity. However, the BLD model does not require the formation of a second neutral line. Rather it suggests that reconnection, and hence the jetting of plasma away from the (distant) neutral line, is increased during substorms. The resultant enhanced Earthward flow causes an instability to grow at the interface of the CPS and LLBL (where the plasma flow is in the opposite direction to that of the CPS). This phenomenon is called the Kelvin - Helmholtz instability (KHI) and it is similar to the wind-over-water instability

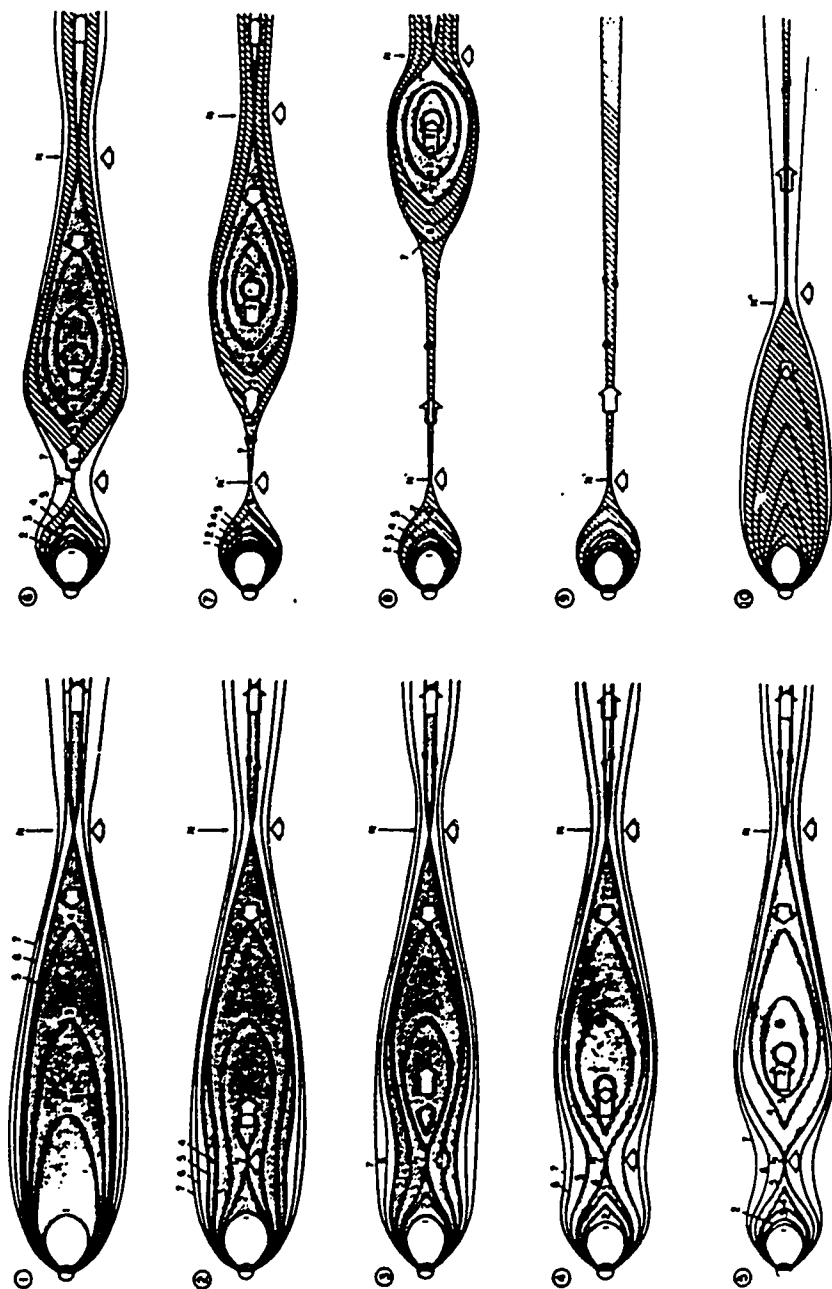


Figure 1.10 : Schematic representation of plasmoid formation and subsequent ejection downtail (Hones, 1979).

that raises waves on the sea. When the KHI occurs in magnetised plasma, there are predictions (Thompson, 1983; Salingaros, 1987) that FAC will flow on field lines threading the region of the instability. Rostoker and Samson (1984) suggest that this current flows in order to try and stabilise the wave growth and that it leads to, among other things, the formation of surges in the evening sector.

Following the figures and notation used by Rostoker and Eastman, figure 1.11 shows the proposed scenario for the generation of the KHI at the CPS/LLBL boundary. If the plasma at this boundary is treated as in ideal MHD plasma (as described in appendix II), then the growth of the KHI is described by a growth rate coefficient,  $\gamma$ , where

$$\gamma^2 = \frac{\rho_1 \rho_2}{(\rho_1 + \rho_2)^2} \left[ \mathbf{k} \cdot (\mathbf{v}_2 - \mathbf{v}_1) \right]^2 - \frac{(\mathbf{B}_1 \cdot \mathbf{k})^2 + (\mathbf{B}_2 \cdot \mathbf{k})^2}{\mu_0 (\rho_1 + \rho_2)} \quad (\text{Eqn 1.7})$$

with the subscripts 1 and 2 referring to the LLBL and CPS respectively. The other variables are mass density  $\rho$ , convective flow velocity  $\mathbf{v}$ , wave number  $\mathbf{k}$  and local magnetic field  $\mathbf{B}$ . If the KHI does indeed grow, the resultant surface wave motion relative to the original source of the instability is characterised by a phase velocity  $\mathbf{V}_p$  where

$$|\mathbf{V}_p| = \frac{\hat{\mathbf{k}}}{(\rho_1 + \rho_2)} \cdot \left[ \rho_2 \mathbf{v}_2 + \rho_1 \mathbf{v}_1 \right] \quad (\text{Eqn 1.8})$$

where  $\hat{\mathbf{k}}$  is the unit  $\mathbf{k}$  vector.  $\mathbf{V}_p$  is directed along the LLBL/CPS



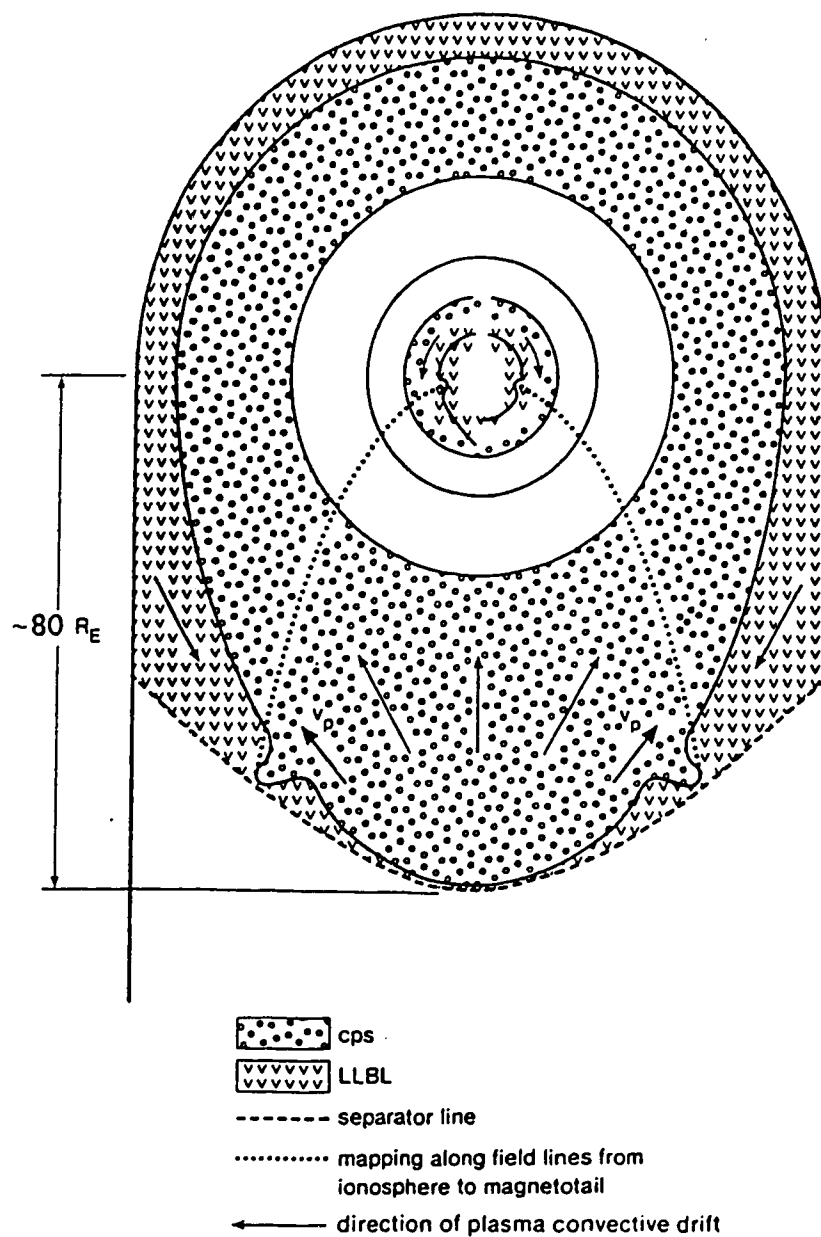


**Figure 1.11** : A likely scenario for the generation of the Kelvin-Helmholtz instability, after Rostoker and Eastman (1987).

interface in the direction of greater momentum density.

From equations 1.7 and 1.8, it is evident that both the KHI growth and propagation can be modulated by changes in the momentum density contrast between the CPS and the LLBL and by the orientation of  $\mathbf{B}$  to the wave vector  $\mathbf{k}$ . The growth rate is a maximum when  $\mathbf{B}_1$  and  $\mathbf{B}_2$  are perpendicular to  $\mathbf{k}$ , and the waves will propagate earthward or anti-earthward, depending on whether the magnitude of the momentum density in the CPS is greater or less than that of the LLBL. It is the possibility of this modulation that provides the opportunity for the BLD model to explain many of the observed features of substorms.

### 1.8 : The VIKING Satellite Project

The VIKING satellite was a multi-national collaborative project coordinated by Sweden. Launched in February 1986, the satellite carried a number of experiments to investigate the magnetospheric plasma and the generation of aurorae. The general design philosophy of all the experiments was to increase the time and instrument resolution for measurements of parameters such as magnetic field and electric field vectors, energetic particle energy spectra, pitch angle distribution and the distribution function of energetic particles and high and low frequency plasma waves. The imager contained two charge coupled device (CCD) cameras (see chapter 2), each covering a different wavelength range in the ultra-violet (UV). The camera with a

bandpass of 1345 - 1900 Å (corresponding to some of the LBH transition bands of  $N_2$ ) was the source of the images analysed in this project, and it is described in some detail in chapter 2.

The highly eccentric orbit (perigee of 817 km, apogee of 13,527 km) was configured so that, at least for the first few months of operation, VIKING had just passed perigee as it started transmitting images of auroral regions in the northern hemisphere. This maximised the spatial resolution of the camera when it was able to send data to Earth, because the satellite contained no onboard recording equipment and only one tracking and monitoring station, located in northern Sweden, was used during the duration of the VIKING project. With the satellite orbit varying in altitude over  $\approx 2 R_E$ , an opportunity was provided to study in detail the accelerator region of the auroral electrons.

### 1.9 : Objectives of Thesis

The work carried out during the course of this thesis project was aimed at studying the characteristics of auroral surges using UV images of the aurora taken by VIKING. To date, there have been few publications of work similar to this based on VIKING data, which is why there was the intention to analyse only somewhat broad characteristics of surges. It was hoped this work would reveal information about any underlying structure related to the occurrence

of surges at different locations around the nightside auroral oval, and whether, during the course of a substorm, surges maintain any systematic motion. In addition to this, a proposed study of how often multiple surge features appear, and some measure of the absolute rate of occurrence of surges was undertaken in, the hope that it would yield useful and meaningful results. Such results could then be compared with previous satellite and ground based studies of surges. Furthermore, such results might be more readily explained by one particular model of substorms than another.

## 2 : DATA ACQUISITION

### 2.1 : UV Camera Design

In keeping with the general philosophy of the the VIKING project, the imagers designed and built for the satellite were a noticeable improvement over previous auroral imagers in terms of both spatial and temporal resolution of images acquired. The improvement in resolution was a result of using now relatively well established charge coupled device (CCD) technology. The desire of the experimenters to obtain images of the dayside auroral oval, and to observe the nightside oval with the sun close to the camera field of view led to the development of an imager that was sensitive only to vacuum UV wavelengths (where solar emission and atmospheric reflection are very low). A compact camera design with low power requirements were also important design considerations and favoured the use of CCD's.

A schematic diagram of the VIKING camera design is shown in figure 2.1 and some comments on the design and its mode of operation are in order. More detailed information regarding the camera can be found in Anger et al. (1987.)

The layout of camera optics, namely that of an inverse Cassegrain Burch system, was first used by Burch (1947) in the design of microscope objectives. The advantage of this design is that angular

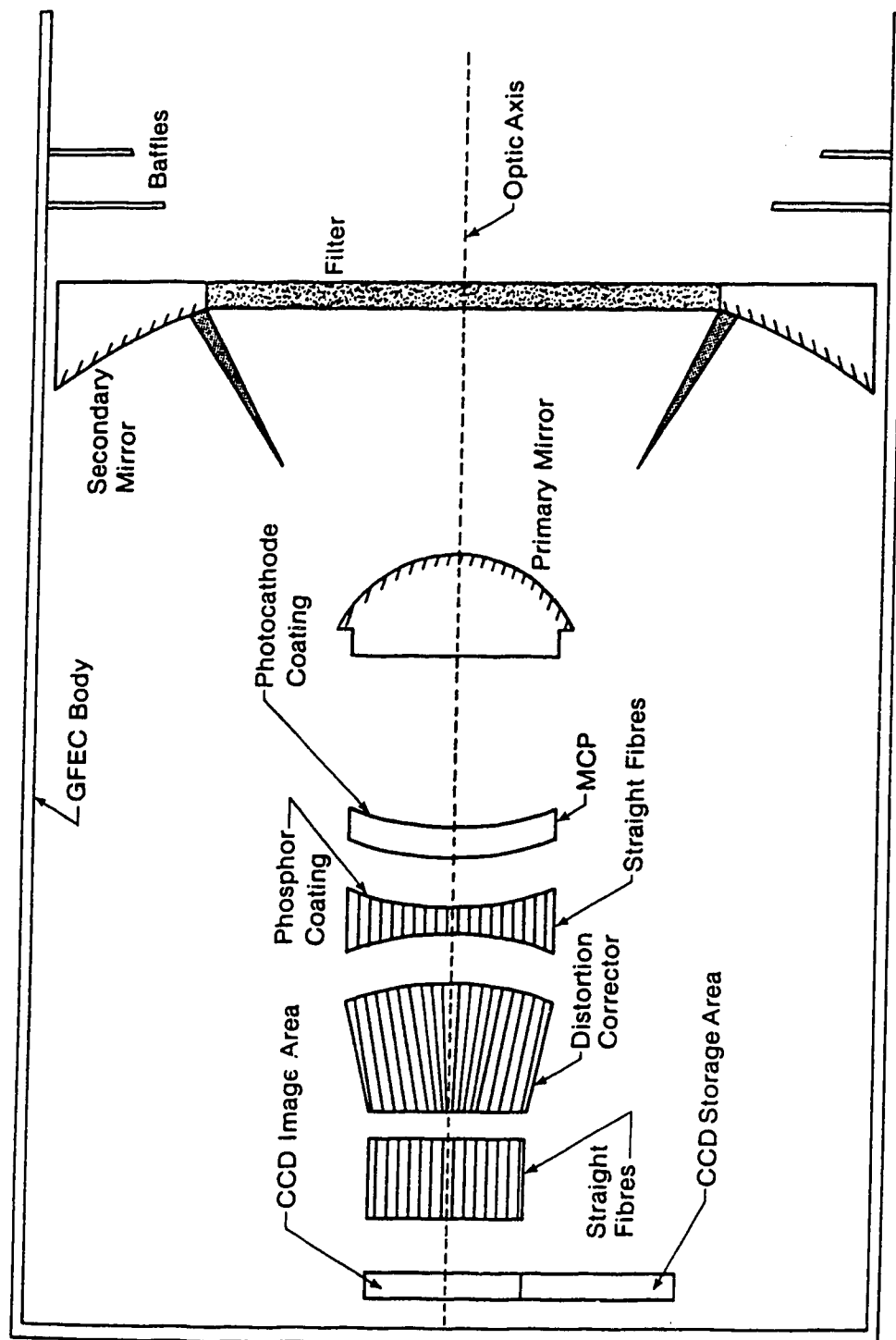


Figure 2.1.1 : Schematic diagram of the VIKING UV camera, adapted from Anger et al. (1987).

distortion of the image is minimal. However, whereas most optical imaging devices produce a plane image surface, the inverse Cassegrain configuration results in a spherical image surface. By having an image intensifier that conforms to the spherical image and then using a tapered fibre optic bundle to map the spherical image onto the flat CCD array, a distortion free projection of the intensified image is possible.

The system works as follows : the spherical mirrors produce an image on the spherical cathode on the front surface of the microchannel plate (MCP), which is in effect an array of electron multipliers. Electrons released from the photocathode cascade through the channels of the MCP and form an electron image on the phosphor coated surface of the fibre optic bundle. Photons from the phosphor travel the length of a straight fibre optic bundle and enter a second (tapered) bundle which acts as a distortion corrector, and the image is finally formed on the planar CCD array.

Details of CCD operation and CCD arrays can be found in a number of publications, e.g. Howes and Morgan (1979) so only the most basic discussion of CCD array operation will be given here. A single element of a CCD array is effectively a capacitor, with one metal plate and one plate of semiconductor material. The dielectric between the plates is a metal oxide. One of the basic properties of the arrangement, as with any other capacitor, is that it can store charge. The origin of the charge on the capacitor varies for different applications of CCDs,

but for imaging applications, photons incident on the image plate can liberate electrons which are then stored by the capacitor. Ideally, the net charge accumulated by the capacitor is proportional to the total number of photons incident. To make a CCD array, a square array of capacitors is manufactured on a single piece of semiconductor substrate. For such an array, all accumulated charge at one capacitor site (or *pixel*) can be made to flow into adjacent locations if suitable control voltages are applied to the array.

For the CCD array in the VIKING camera, as with most CCD arrays, the image pixel data are read out by applying a clock pulsed voltage across the array. This causes the charge accumulated at each pixel site to move one pixel in the direction of the applied voltage during each clock pulse. The data comprising the image are then read out one row at a time from one edge of the array. Normally, the CCD array is allowed to integrate the optical signal for some fixed time interval, with the image then clocked and read out very quickly so that a uniform exposure time across the array is maintained. However, for the VIKING camera, a slightly different readout process was used. Because the satellite rotates (with a spin period of 20s) the optical image focussed on the CCD plate will move across it. Image data were clocked across the array and read out at the same rate the optical image moved. This resulted in an effective exposure time of 1s for the images. This electronic despinning required the CCD array to have its axes very accurately aligned relative to the satellite spin axis, i.e. one axis of the CCD array aligned parallel to the spin axis.



## 2.2 : Camera Parameters

The Cassegrain mirrors result in an f1 camera lens of focal length 22.4 mm. Angular resolution of the collected images is ultimately limited by the spacing of the MCP channels and the pixel size of the CCD array, which gives a resolution of  $0.076^\circ$  by  $0.076^\circ$ . Intensity resolution was set by the 8 bit range of the CCD's readout analogue-to-digital converter (ADC), thus giving a dynamic range of 0 to 255 digital numbers (DN.) However, during operation of the camera, images that were actually telemetered to the ground receiving station consisted of 2x2 pixel averages of the CCD array, termed *superpixels* (Vallance Jones et al., 1987). This made the effective size (in terms of distances in the ionosphere) of one superpixel range from 20km x 20km to ~ 70km x 70km, depending on the altitude of the satellite.

Two cameras (referred to as cameras 0 and 1) of the same design were built and launched onboard VIKING. The difference between cameras was in the different materials used as filters and photocathodes, resulting in each camera having a different wavelength passband. Camera 0 had a passband from 1345 to 1900 Å, which meant that emissions from the Lyman-Birge-Hopfield (LBH) band of  $N_2$  and the 1493 Å NI line contributed significantly to the image intensity. Camera 1 had a passband of 1235 to 1600 Å, thus admitting the strong 1305 Å and 1356 Å multiplets of OI, as well as a small contribution from the LBH bands. The original intention of having two cameras with

differing passbands was to try and deduce the electron energy spectrum of auroral electrons, but, unfortunately, camera 1 ceased operating after ~ 3 months. It will not be discussed further in this thesis.

### 2.3 : Camera Calibration Factors

The CCD readout ADC had a number of different gain settings, which were switchable during real time control of the imager by the ground station. Commonly used settings were 50 and 100. Gain 50 was found to give the optimum balance between signal amplification and avoidance of ADC saturation. In order to ensure consistency of images that were analysed for this research, only images obtained with this gain setting were used.

An intensity calibration of the UV images in terms of conventional units used by ground based observers (i.e. kilo-Rayleighs; kR - see appendix I for definition) was carried out by Vallance Jones et al. (1987), in which they compared image data with ground based data. When a suitable set of images had been obtained, a comparison of image intensities of particular auroral features was made with simultaneously observed features by ground based scanning photometers. The direct cross referencing of VIKING camera and ground based data thus yielded an empirical calibration factor relating the UV intensity measured by the camera to the intensity of the aurora observed on the ground at optical wavelengths. This calibration factor is sensitive to the optical wavelength to which it refers, to the

energy spectrum of the incident auroral electrons and to the look angle of the camera with respect to the local horizontal in the region where the aurorae are being produced. A commonly used wavelength to which intensities are referred is the  $4278 \text{ \AA } N_2^+$  first negative band ( $\lambda 4278$ ), and at this wavelength, the calibration factor is  $60 \pm 10 \text{ DN/kR}$ . The variability of this calibration factor can be seen by noting that its value for  $\lambda 5577$  (an OI line) is  $14 \pm 2 \text{ DN/kR}$  and for  $\lambda 4709$  (part of the  $N_2^+$  First Negative band) is  $\sim 300 \text{ DN/kR}$ . This variation is due to the different production ratios of each line from a given incident electron energy distribution and by differing amounts of atmospheric absorption.

The empirical calibration was cross checked to some extent by predictions made by Vallance Jones et al. (1987) of image intensities using models of atmospheric composition, rates of auroral production and the wavelength response function of the camera (determined before launch using a secondary standard low intensity lamp.) Approximations that had to be made and the limitations of the models used restricted the analysis to yielding calibration factors accurate to not much better than an order of magnitude, but, these were consistent with the experimentally obtained factor.

## 2.4 : Data Collection and Storage

Once VIKING was in orbit and fully operational, UV images, as well as data from other experiments, were regularly transmitted to the

ground receiving station where they were stored on magnetic tape for duplication and distribution. In its normal mode of operation, images were acquired once every minute or so from alternate cameras and with alternating gain settings of 50 and 100. However, at certain times, images were acquired at their highest possible rate of one every 20s (which corresponds to the spin period of the satellite), with these images normally having the same gain setting. Control over where the camera was pointing could be determined in almost real time from the ground station, with this feature being used during observing campaigns involving collaboration among the various groups operating experiments onboard the satellite.

## Plate 2.1

|        |        |
|--------|--------|
| 2.1(a) | 2.1(c) |
| 2.1(b) | 2.1(d) |

The labelling under the images is

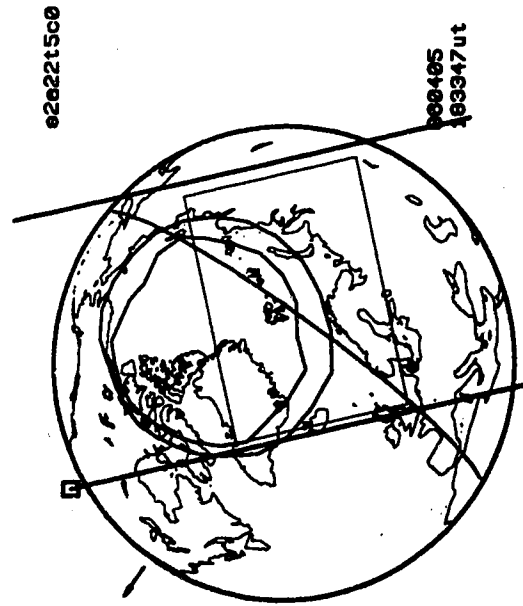
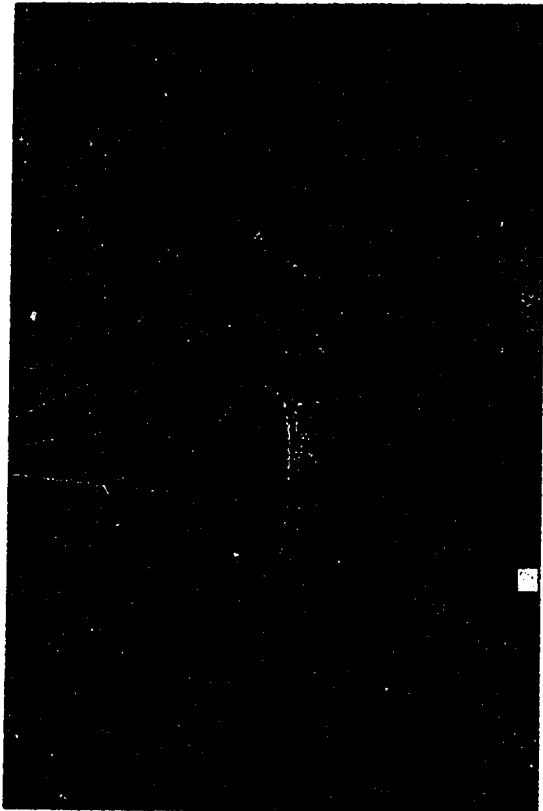
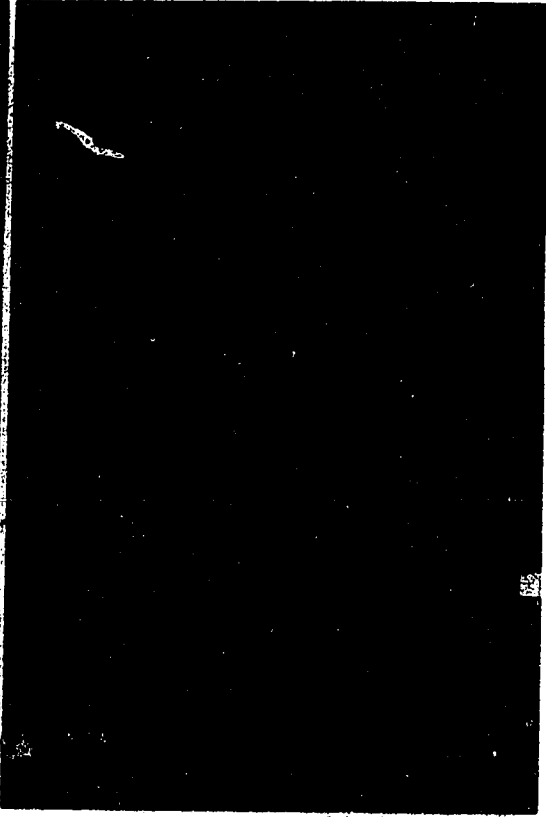
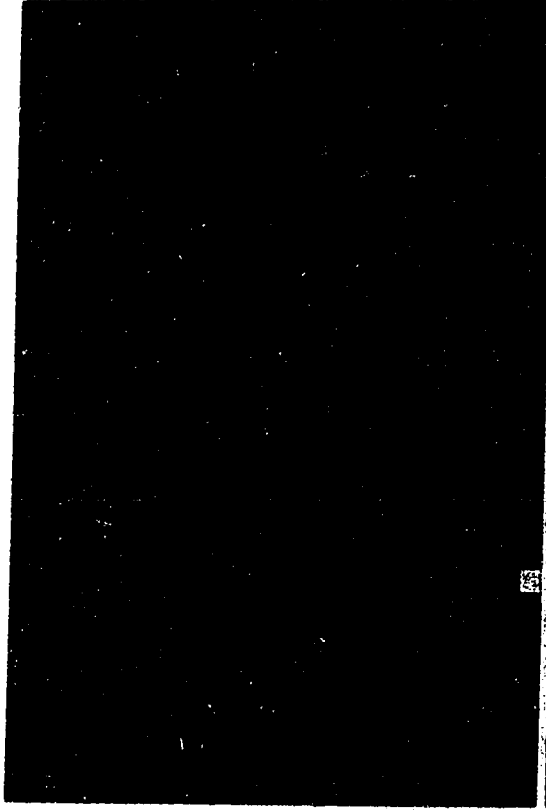
orbit/camera date(yyymmdd)/time(hhmmss) frame number

2.1(a) : A sample VIKING image. Magnetic local time meridians from 2100 to 0000 are drawn on, as well as two lines of geomagnetic latitude at 59 and 68 degrees. The colour bar represents a linear intensity scale from 0 to 255 DN.

2.1(b) : A drawing showing where the VIKING image in 2.1(a) is located on the earth. It indicates the position of the image, the average position of the auroral oval, an arrow indicating the direction of the sun and the day/night terminator.

2.1(c) : An image taken showing the quiescent oval just prior to the intensification seen 6 minutes later in 2.1(d). The small white circle indicates the limit of the field of view 40 degrees from overhead at Churchill, Manitoba. Magnetograms from Churchill are shown in figure 3.2.

2.1(d) : An intensification within about 50 km from Churchill that saturated the camera sensitivity. Magnetograms of this event show that this event was unrecorded in terms of any magnetic signature.



### 3 : ANALYSIS AND RESULTS

#### 3.1 : OUTLINE OF ANALYSIS

The possible types of analysis that can be performed with a new data set are usually considerable, and with the substantial improvement that the VIKING images provide over existing data sets, there are a large number of analysis options open. Restricting the analysis to surges still left a large number of different options open, but it was decided to concentrate on some of the more basic statistical properties of surges, with additional analysis of particular surge formations and development being undertaken only for a small number of cases.

Four distinct, but related, forms of surge analysis were performed with a portion of the VIKING data set of images (the total data set consists of 47189 images from 1874 orbits), with the statistical analysis conducted with two separate sets of data each consisting of 50 consecutive orbits of the satellite. However, the first priority was to derive a working definition of a surge in terms of information contained within the images. Then, statistical details were compiled relating to the distribution of surges as a function of Magnetic Local Time (MLT) and to the occasions when more than one surge was present on a given image (viz surge multiplicity). Surge multiplicity was investigated in greater depth for a number of images

by performing spatial two dimensional Fourier analysis of images in the region containing surges, while the distribution of surges with MLT was treated in more detail by examining the position of surges at various stages during substorm development. This last part of the analysis was conducted to find out if surges maintained any systematic motion during substorm development, viz. the westward travelling surge.

### 3.2 : DEFINITION OF A SURGE

In previous studies of surges, the data have been primarily groundbased, in the form of magnetograms and all-sky camera pictures. It was from such information recorded at irregularly positioned observation points that most studies of the *auroral substorm* were conducted. With global imaging of the ionosphere now routinely available, it is reasonable to refine the definition of surges taking into account the advantages of the new data.

In terms of image data, a particular feature was called a surge if it satisfied the following conditions:

- 1) *It appeared at the poleward edge of the auroral oval.*
- 2) *The maximum intensity exceeded a threshold of 180 DN (equivalent to an intensity of  $\approx 3\text{kR}$  for  $\lambda 4278$  and  $\approx 13\text{ kR}$  for  $\lambda 5577$ ).*



3) *The minimum area of the feature that exceeded the threshold was one superpixel.*

4) *It was separated from adjacent features exceeding the threshold by at least one superpixel of intensity below the threshold.*

This definition of a surge was arrived at by considering the practical constraints of using images to define surges, and by considering previous definitions of surges, so some discussion on the meaning and interpretation of this definition is required.

Historically, surge forms have been defined as occurring at the poleward edge of the auroral oval and there seems no reason to change this aspect of the definition. Indeed, it is evident from the VIKING images that features occurring at the poleward edge of the oval often have different characteristics from auroral intensifications equatorward of the poleward edge, in what is known as the diffuse auroral region.

The threshold intensity of 180 DN was chosen because it was at about this intensity that well defined and localised features and structures of the oval were first observed. If a value of less than 180 DN had been chosen for the threshold level, there would have been occasions where surges with this low level of intensity would have been obscured by the luminosity of the surrounding oval. Comparing this image threshold level to a corresponding intensity as observed

from the ground, the  $\lambda 5577$  intensity of  $\approx 13$  kR would be neither excessively bright nor extremely faint. The effect of changing this threshold will be discussed in § 3.7.

The scale size of features that are counted as surges in this study can be much smaller than in previous studies of surges. This is mainly due to the fact that surges have previously been studied, as mentioned previously, as  $\pi$  phenomena or optical forms. The size criterion of a surge being  $\pi$  as only one superpixel is somewhat arbitrary and was set by the design parameters of the camera and not by physical reasoning as to the scale size of a surge. However, when the images are contoured, it is found that in instances where only one superpixel exceeds the threshold criterion, there is still a structure to the contours surrounding this superpixel. Thus in cases where only the one superpixel exceeds the threshold, it is metaphorically only the 'tip of the iceberg' in terms of surge structure and form. It should also be emphasised that a superpixel is a  $2 \times 2$  average of 4 CCD pixels (as discussed in chapter 2, §2.2), so that in order for a superpixel to exceed the threshold, a number of CCD pixels have to record the enhanced intensity associated with the surge. This reduces the chances of spurious phenomena contaminating the image signal. (For example, cosmic rays and energetic auroral electrons have been found to affect the CCD image.)

As a check that the above definition of a surge is reasonable, images were sought that contained surges in local time sectors where

there were magnetic observatories. A comparison of the image data was then made with the magnetic variations recorded at these observatories. When this was done for a number of cases, a number of conflicting outcomes were observed. There were cases where both the magnetic and UV signature of the surge were seen, cases where there was a strong UV signature but no apparent magnetic signature, and finally cases where there were magnetic signatures but no apparent UV signatures. This rather puzzling picture can only partially be understood and what might lie at the heart of the solution is that the height of UV emissions in the ionosphere may be from roughly 180 km and down, and the height at which the electrojet currents flow (which are primarily responsible for the magnetic signature of a surge) is centred around 120 km. The energy spectrum of the precipitating auroral electrons in any given surge is not known and so the depth of penetration into the ionosphere and the spectrum of optical emissions they cause cannot be known *a priori*, nor is it easy to infer them from ground based measurements. Figure 3.1 shows the magnetograms of a positive correlation between magnetic and UV surges as shown in plate 3.1(a) and 3.1(b), while figure 3.2 displays magnetograms showing no magnetic signature of a surge seen by VIKING (plate 2.1(c) and 2.1(d)). Finally, figure 3.3 shows the case of a strong magnetic surge, but no surge, satisfying the intensity criterion, was observed by VIKING (plate 3.1(c) and 3.1(d) ).

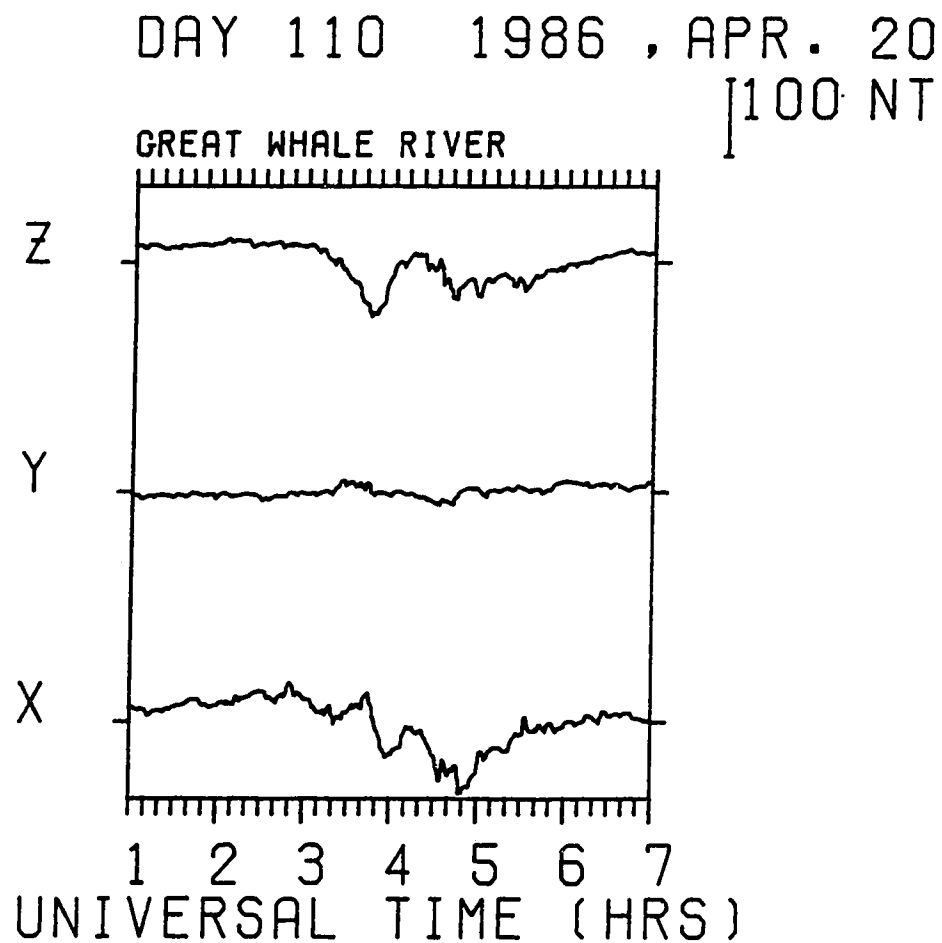


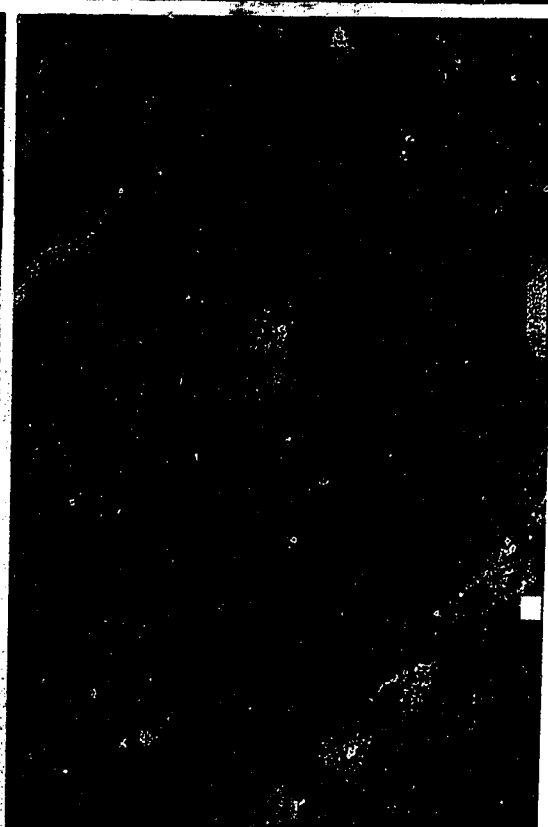
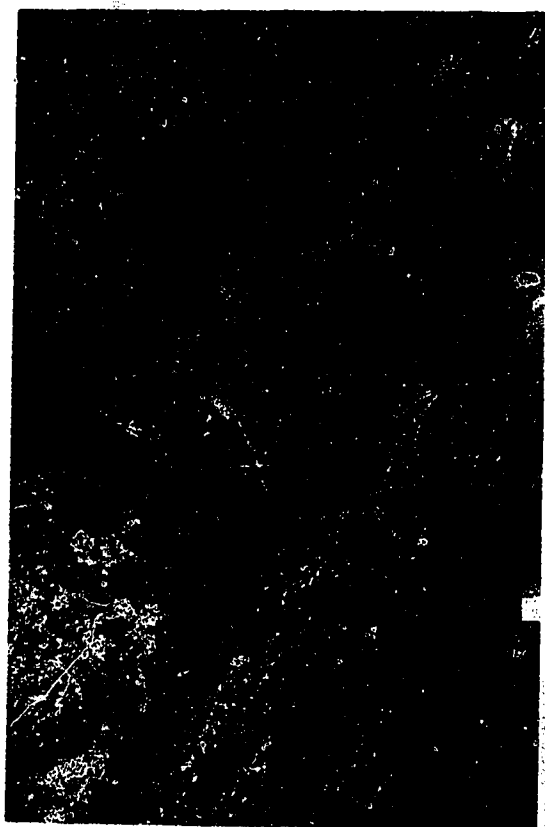
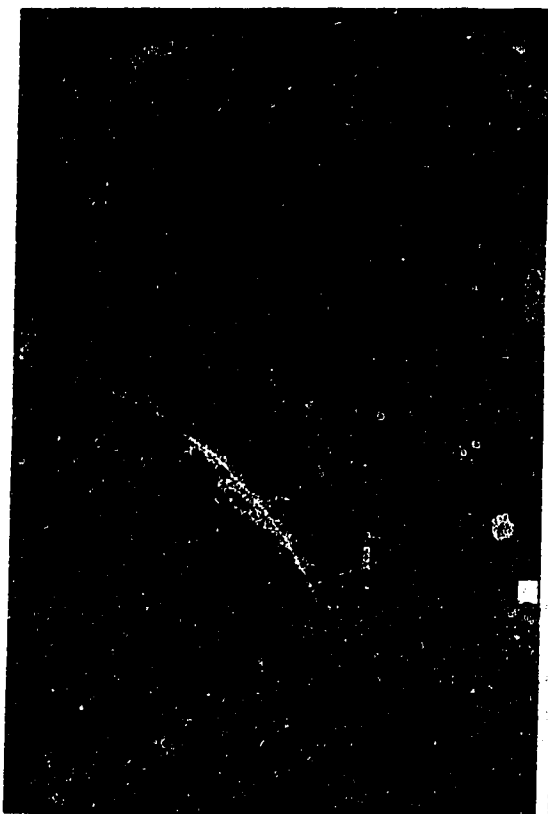
Figure 3.1 : Magnetogram showing a small surge signature at 0320 UT that corresponded to a surge detected by VIKING. See plate 3.1(a) and 3.1(b) for the corresponding images.

Plate 3.1

|        |        |
|--------|--------|
| 3.1(a) | 3.1(c) |
| 3.1(b) | 3.1(d) |

3.1(a) and 3.1(b) : Two images separated by almost 3 minutes showing the intensification of an auroral surge. Great Whale River (Poste de la Baleine) magnetic observatory is located at the intersection of the (geographic) latitude and longitude lines. The accompanying magnetogram for this event is shown in figure 3.1. It shows a small signature of a surge which started at 0320 UT.

3.1(c) and 3.1(d) : Two images of auroral intensifications. Great Whale River is located at the intersection of the latitude and longitude lines. The magnetogram from this station (shown in figure 3.3) shows a large magnitude signature of a surge at 0340 UT. However, the images show that there was no substantial brightening of the auroral oval or appearance of a surge feature in the vicinity of the station.



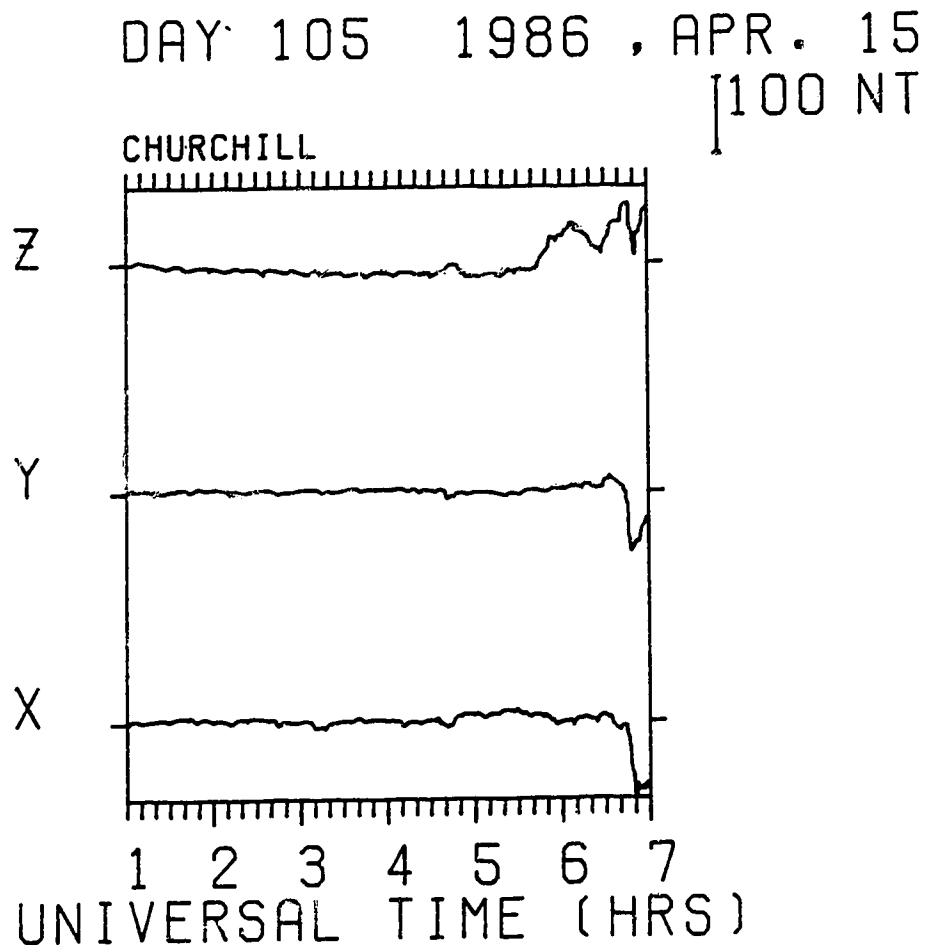


Figure 3.2 : Magnetogram showing apparent absence of a magnetic signature for a surge detected by VIKING between 0545 UT and 0551 UT. See plate 2.1(c) and 2.1(d) for the corresponding images.

DAY 112 1986 , APR. 22

100 NT

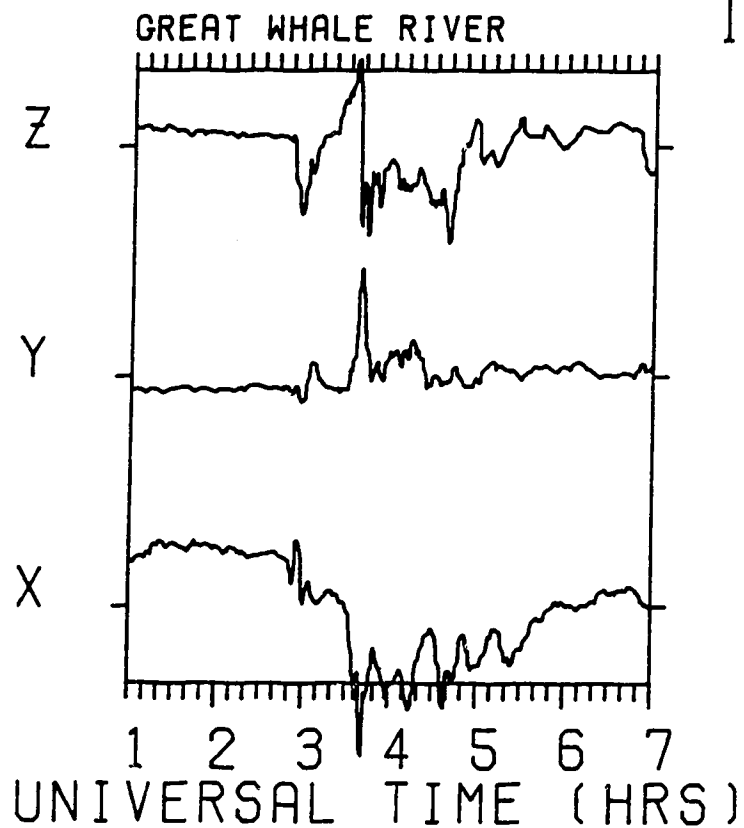


Figure 3.3 : Magnetogram showing a strong surge signature at 0340 UT where no intense surge was detected by VIKING. See plate 3.1(c) and 3.1(d) for the corresponding images.



### 3.3 : Compilation of Data on Surge Position and Intensity

With a working definition of a surge having been settled on, a data base consisting of surge position and intensity was constructed, containing data on all surges found in each of the two sets of 50 consecutive orbits that were analysed (hereafter referred to as data set A and data set B.) The reason for developing two independent sets of data was so that comparisons could be made between the final results of the statistical analysis.

In order to obtain these data, a satellite image analysis software package called SYSTEM was used to view and analyse VIKING images. If a surge was seen in an image, its location in terms of geographic and geomagnetic coordinates, as well as the MLT of the surge were recorded. Also, the Universal Time (UT) of the image and a number of ancilliary items of data (e.g. the orbit number and frame number of the image) were recorded.

For data set B it was also possible to record the intensity of surges but unfortunately, due to software deficiencies, it was not possible to obtain this information for the surges in data set A. Further limitations of software prevented background, distortion and vignetting corrections being applied to images before they were analysed. However, the effect of these corrections for the vast majority of data analysed is quite small. For example, background contributions to the regions of images that were analysed were small

because only the nightside oval was being investigated and distortion effects were minimal when the satellite look angle was close to the local perpendicular to the earth. Also, steps were taken to try and minimise the contribution of these effects to the data, viz vignetting effects were avoided simply by not analysing the auroral oval at the edges of images. When image distortion was clearly evident, those images were discarded.

### 3.4 : Distribution of Surges with Magnetic Local Time

To investigate the distribution of surges as a function of MLT, the auroral oval was segmented into  $\frac{1}{2}$  hour bins, from 1800 across midnight to 0100 MLT. Then, for both data sets A and B, the total number of surge events occurring in each time bin was evaluated and plotted. The resulting histograms of surge distribution in the evening sector of the oval are shown in figure 3.4. However, these histograms are not the relative probability distribution histograms of finding surges in a given MLT time zone because not all time bins in the evening sector were viewed the same number of times. In order to compensate for this, the number of times each bin was within the camera field of view was counted and these data used to weight the raw results. Finally, the histograms were smoothed by taking running mean three point averages of the MLT bins and this resulted in the plots shown in figure 3.5. These plots can be interpreted as follows : given that there was at least one surge present in the evening sector, each graph gives the relative probability of the surge(s) being located at

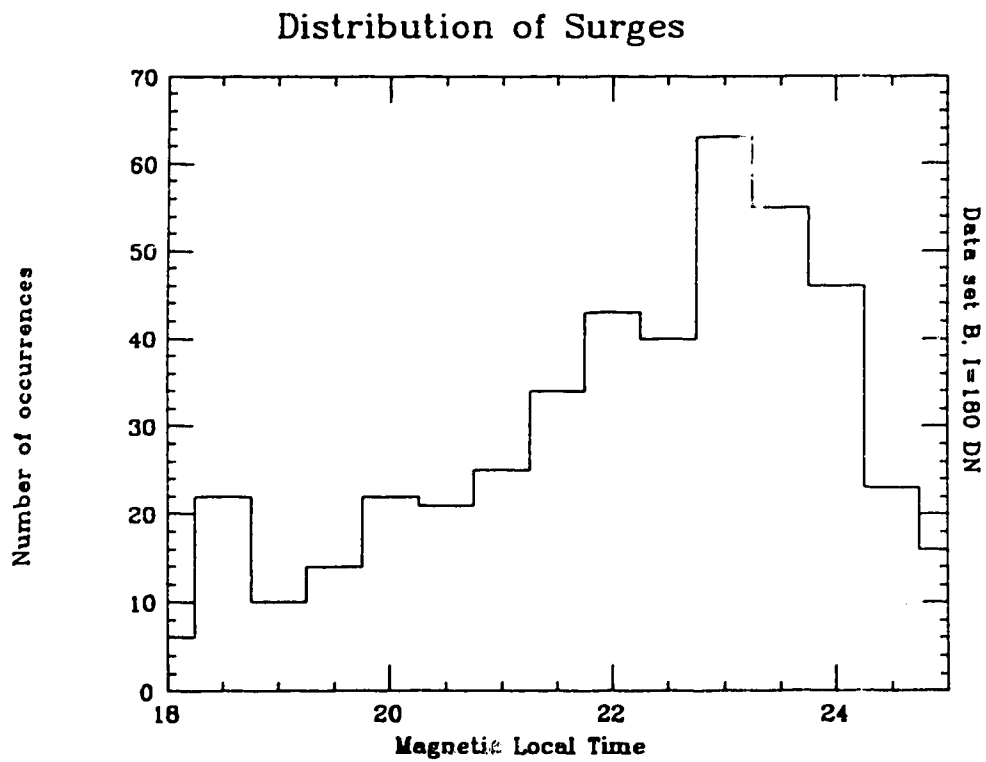
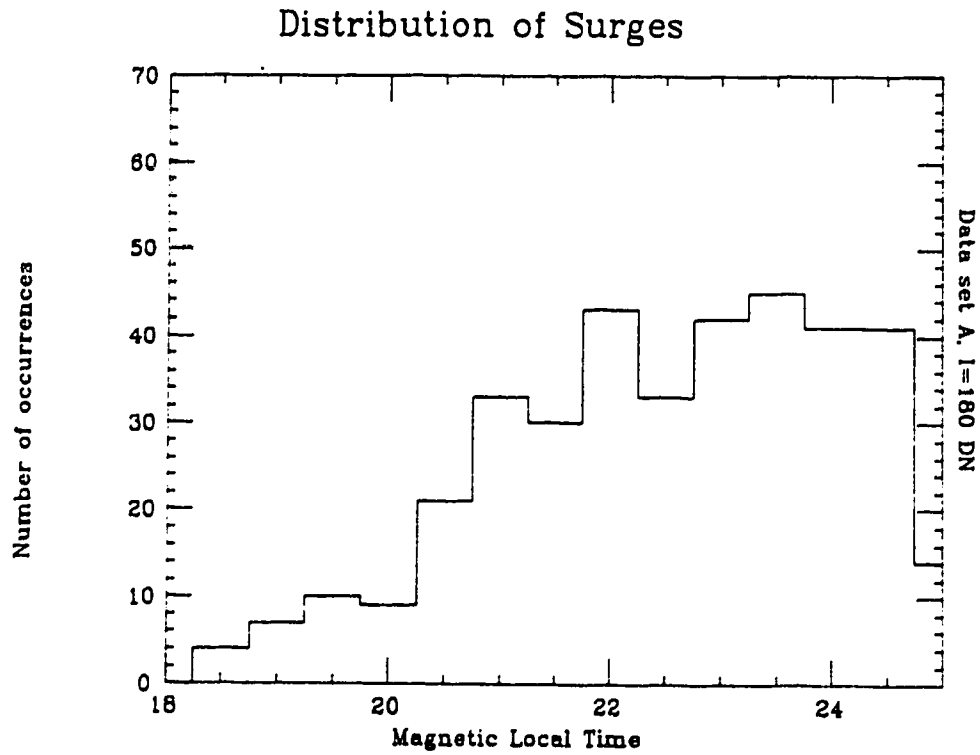


Figure 3.4 : Histograms of the raw data for surge distribution from data set A and data set B.

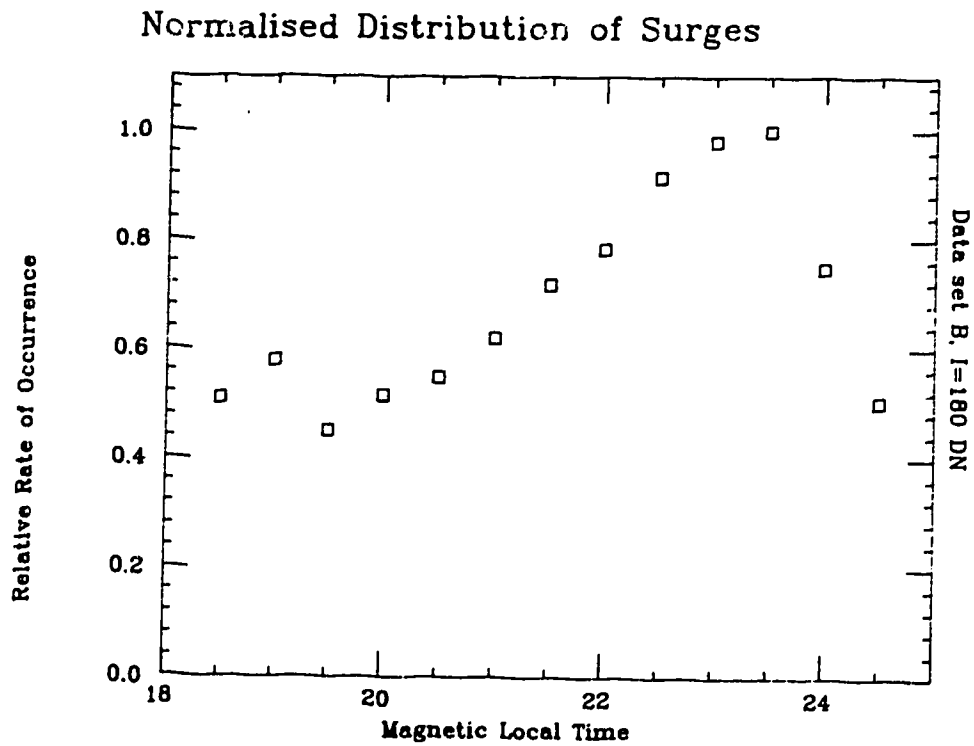
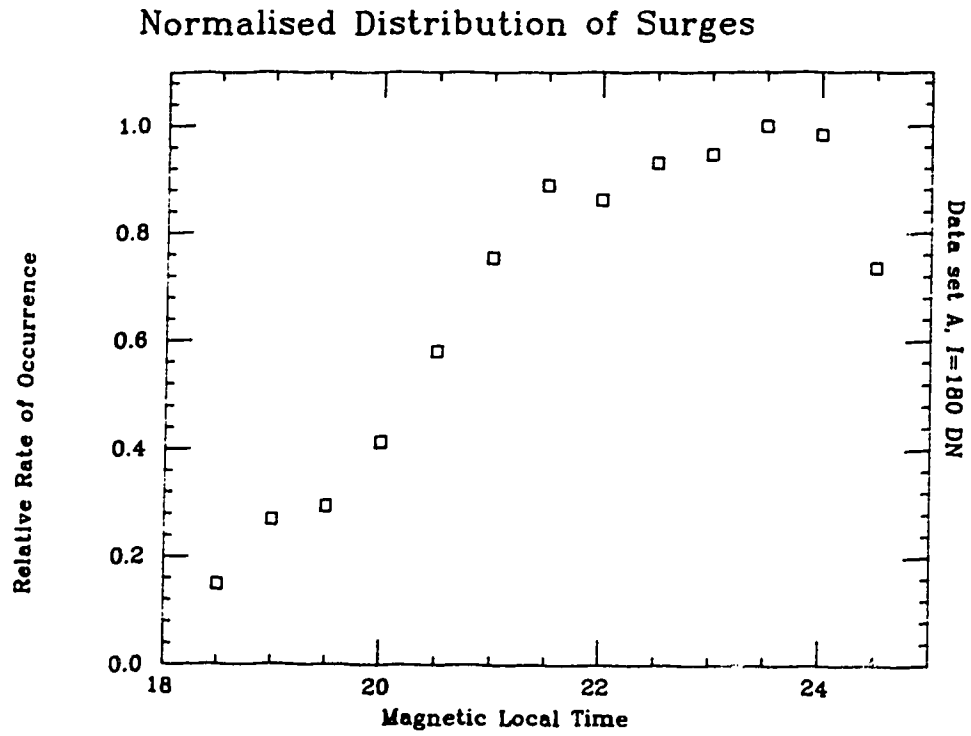


Figure 3.5 : Plots of surge distribution for data set A and data set B normalised and with a 3 point running mean smoothing filter applied.

various magnetic local times.

Although there are some differences between the two data sets, the underlying trend is the same in both cases. The most likely MLT zone in which surges were found is between 2300 and midnight, though for data set A the peak in the occurrence frequency plot is somewhat broader than for the second data set. On either side of midnight, there is a reduction in the probability of finding surges, with this drop in probability occurring more steeply as one moves towards the dawn sector as opposed to the evening sector. As one goes from midnight across the evening sector, both data sets display a drop in the relative occurrence of surges, with this drop being an almost monotonic function of MLT for data set A, while data set B has a small local maximum at 1900 MLT. Discussion of this local maximum can be found in § 4.3.

While no quantitative analysis of the statistics was performed to see if the results obtained were robust, two qualitative indicators were checked. The first and most basic of these was repeatability, which has already been demonstrated by the graphs shown in figure 3.5. The other test was to look at how the trends in the statistics changed with the threshold value of the surges. Given that the choice of threshold level (c.f. § 3.2) was set in a somewhat subjective fashion, the variation of the statistical trends as a function of this parameter is important. The raw data were replotted at successively increasing values of threshold level up to the saturation level of the

camera, and the result was the two dimensional histogram shown in figure 3.6. It shows that no significant changes in the distribution of surges took place as the surge threshold intensity was increased. For each level of threshold, the most probable MLT zone in which to find surges was still between 2300 and midnight. However, at the higher threshold levels, the number of surges seen in each MLT bin was low enough that (Poisson) random sampling errors could be significant (the fractional error in the counting of random events is  $\propto N^{-1/2}$  where  $N$  is the number of events counted).

By producing a scatter plot of surge intensity against MLT, further statistics relating to the location of surges in the evening sector were obtained. However, the scatter plot, shown in figure 3.7 does not reveal any meaningful trends. It should be noted that the dynamic range of intensity of the VIKING camera was not large enough to encompass the range of surge intensities produced, as verified by the large number of surge events that saturated the camera. Perhaps a scatter plot with a higher correlation between surge intensity and MLT would be produced if the full range of possible surge intensities could be handled by the camera.

### 3.5 : Absolute Levels of Surge Activity

As a follow up to the histogram results of the distribution of surges with MLT, the fraction of time that each evening time sector had surge activity in it was calculated. The procedure used for

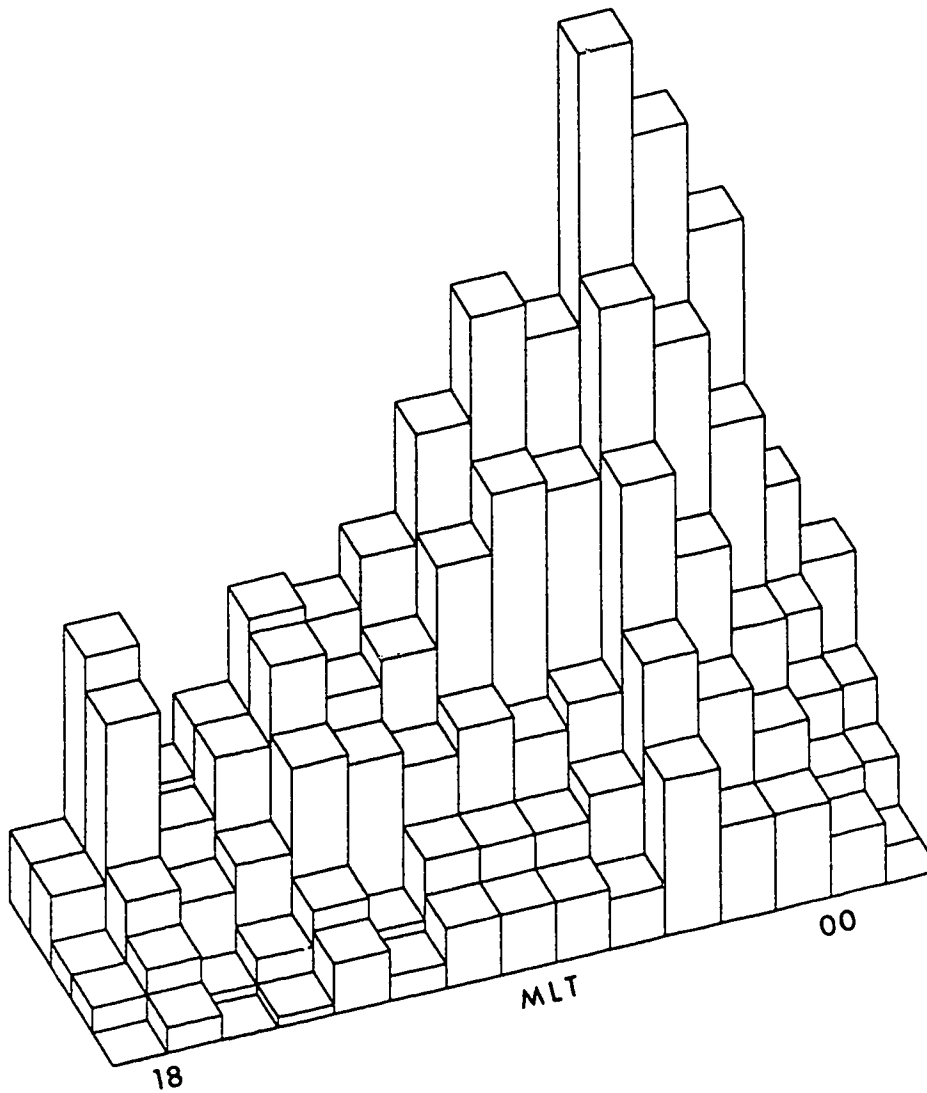


**Figure 3.6** : A two dimensional histogram of the raw data from set B plotted at various surge threshold intensity levels. The MLT bins run from 1800 to 0100 in 1/2 hour bins and vertically, the tallest peak represents 64 events. The threshold levels at which the data are plotted are 180 DN, 200 DN, 220 DN, 240 DN and 255 DN.

# Scatter Plot of Surge Position and Intensity

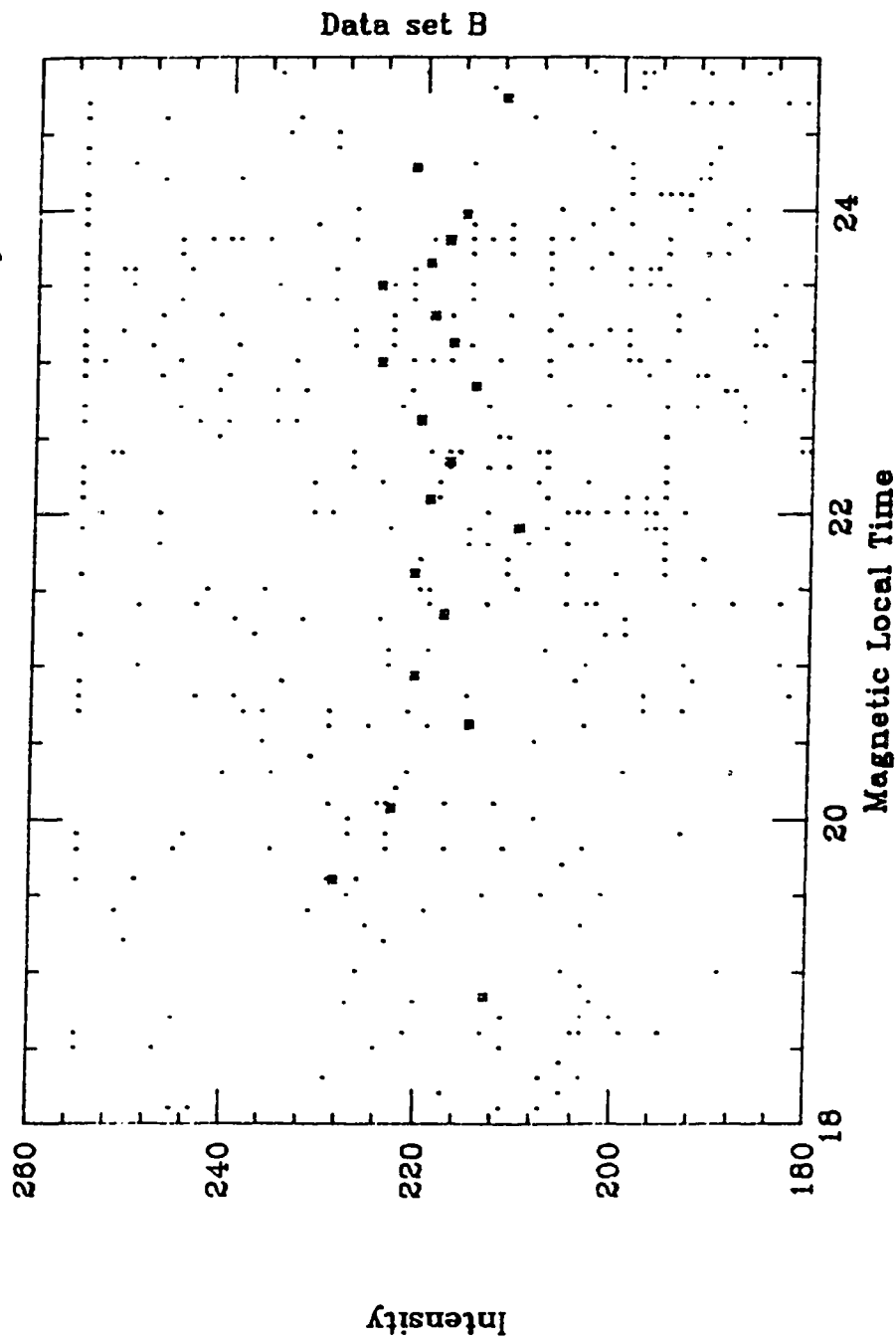


Figure 3.7 : Scatter plot of surge intensity versus MLT for data set B. The small points represent individual surge events and the larger points represent 20 point averages of the individual events.



determining these statistics was to produce contour plots of all the images in the two data sets, contoured at levels that made it easy to see if the threshold of surge activity had been exceeded. As a result of using this approach, the MLT time bins were one hour in size and not  $\frac{1}{2}$  hour time bins as used for the analysis of surge distribution.

The graphs resulting from this analysis are shown in figure 3.8. The most frequently active zone for data set A was centered on 2300 MLT while that of data set B was centered at 2200 MLT. The importance of the absolute activity frequency in the evening sector is that it gives a measure of the fraction of time that the magnetosphere is active (in terms of producing substorm features). For both data sets, the frequency of activity in the most active zone is  $\approx 15\%$ . Unfortunately, the frequency of activity across the entire evening sector cannot be readily calculated from the data presented here because the entire evening sector was not often within the field of view of the camera. However, a lower limit on the fraction of time that there is activity occurring somewhere in the evening sector is 15%, for a surge threshold level of 180 DN.

### 3.6 : Surge Multiplicity

The simultaneous occurrence of surges in the evening sector was investigated with the two data sets (A and B) by counting the number of times one surge, two surges, three surges etc. were simultaneously seen on images in each data set. The resulting histograms are shown in

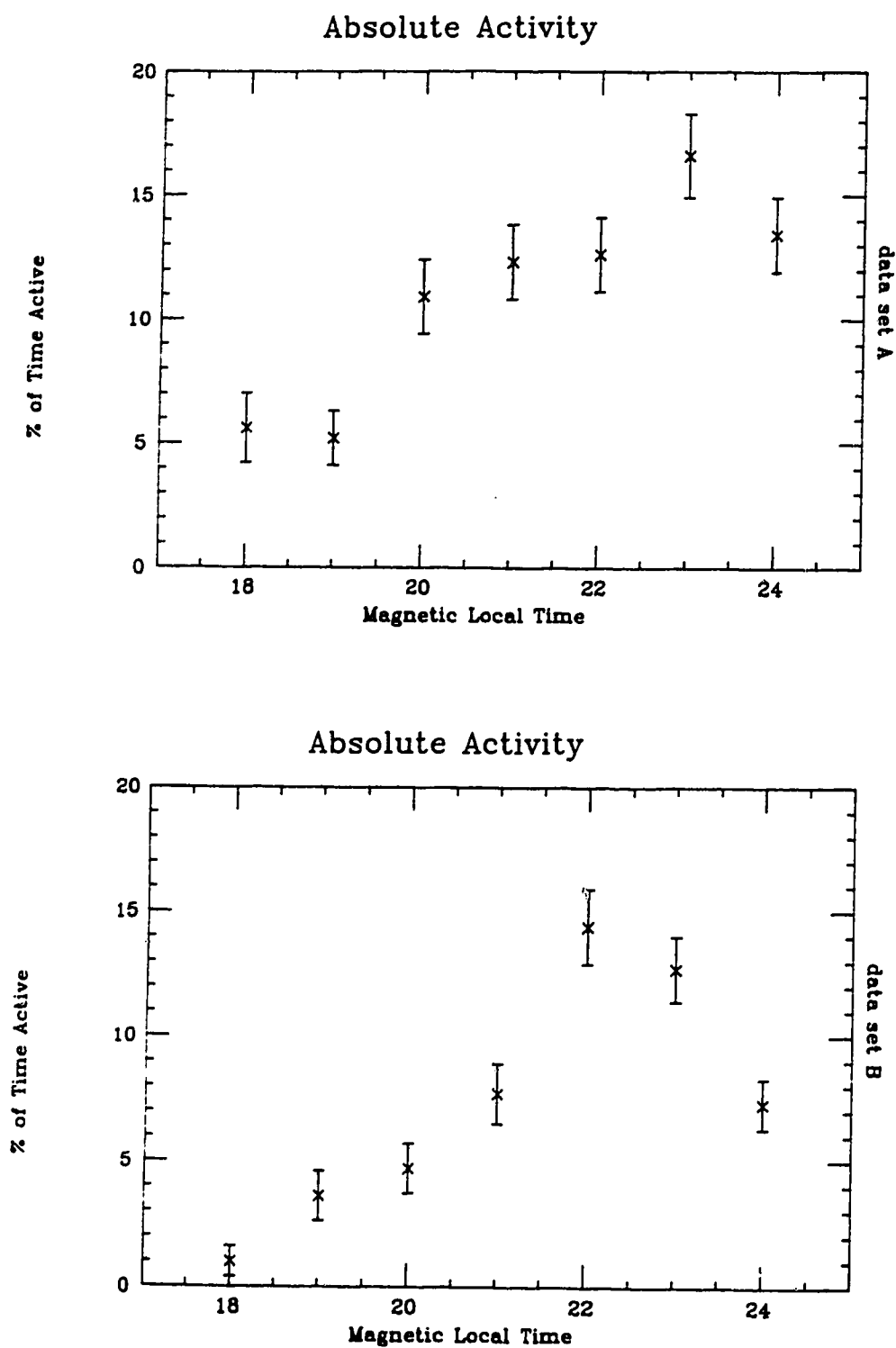


**Figure 3.8** : Graphs of the absolute levels of surge activity as a function of MLT for both data sets.

figure 3.9. While the graphs from both data sets show quite clearly that surges appeared more often as single forms as opposed to any particular number of multiple forms, there were also a large number of events where surges occurred at higher degrees of multiplicity. Table 3.1 details the results of the analysis, where the error margins are computed assuming random Poisson counting errors.

| Table 3.1 : Summary of Surge Multiplicity Analysis   |                        |            |             |
|--|------------------------|------------|-------------|
|  | Degree of Multiplicity |            |             |
|  | 1                      | 2          | 3           |
| Percentage of Occurrences with this degree or less : |                        |            |             |
| Data set A   | $37 \pm 5$             | $57 \pm 9$ | $75 \pm 12$ |
| Data set B   | $34 \pm 5$             | $60 \pm 8$ | $70 \pm 11$ |

As with the distribution of surges around the evening sector of the auroral oval, these multiplicity statistics were qualitatively tested to see if they were robust. The reproducibility of the statistics between the two data sets gives a lot of weight to their robust nature, so no more checking of this nature was done. However, the histograms for data set B were plotted for surge threshold levels up to the saturation level of the camera. These plots are displayed in figures 3.10 and 3.11 and show that there is little change in the broad trend of the data, though at higher threshold

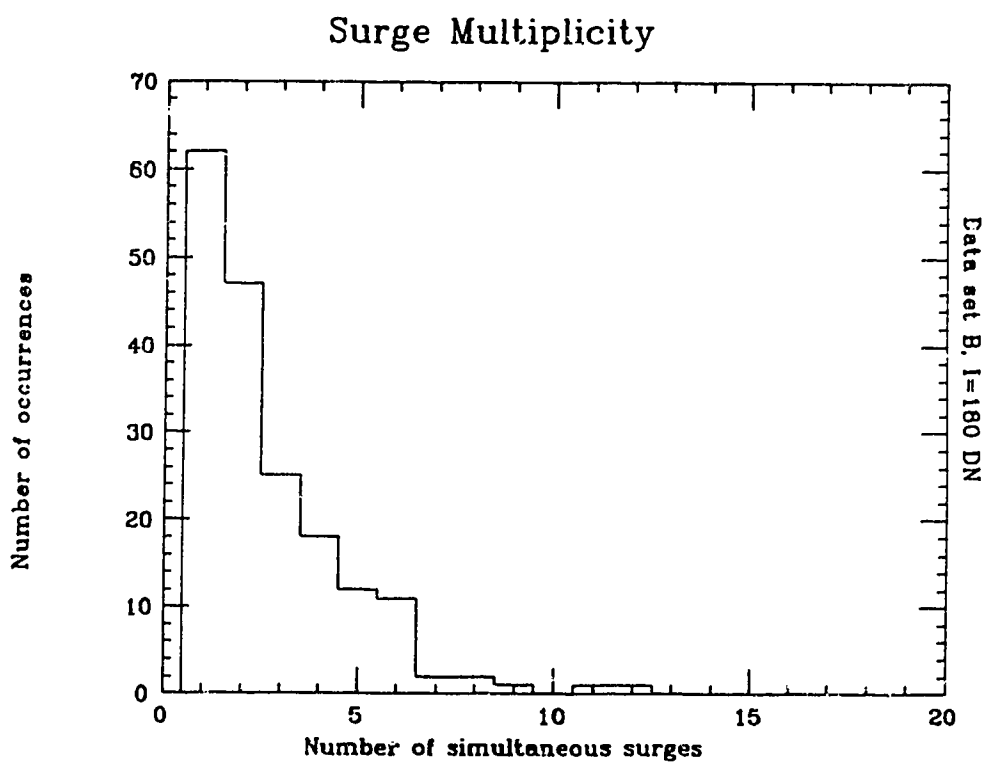
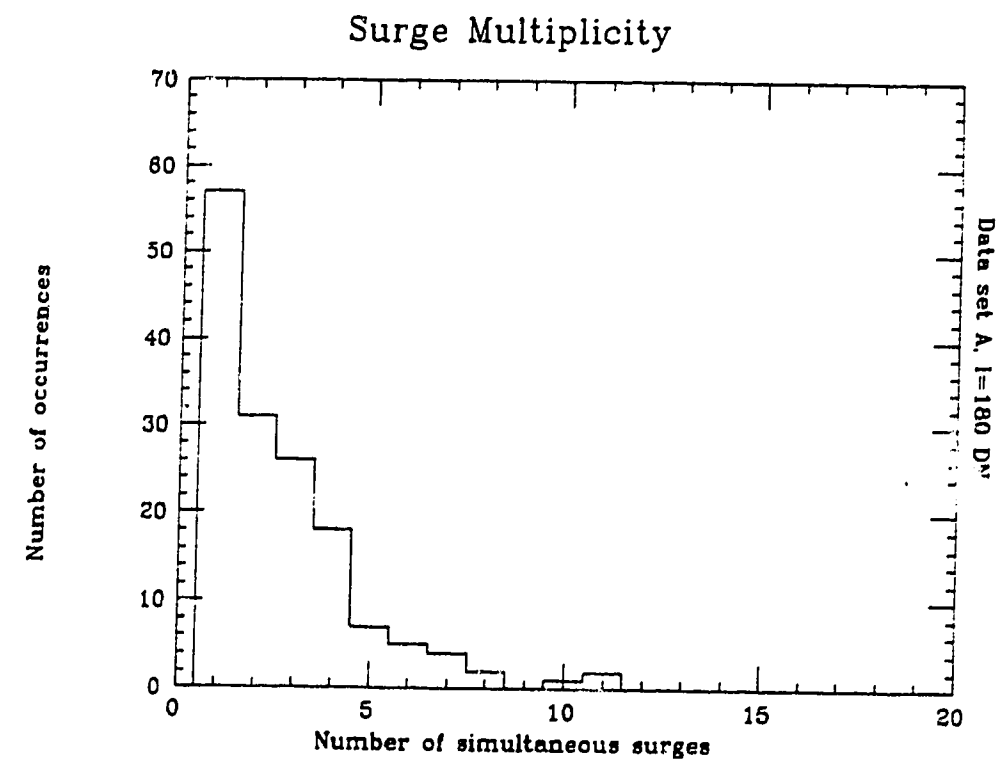
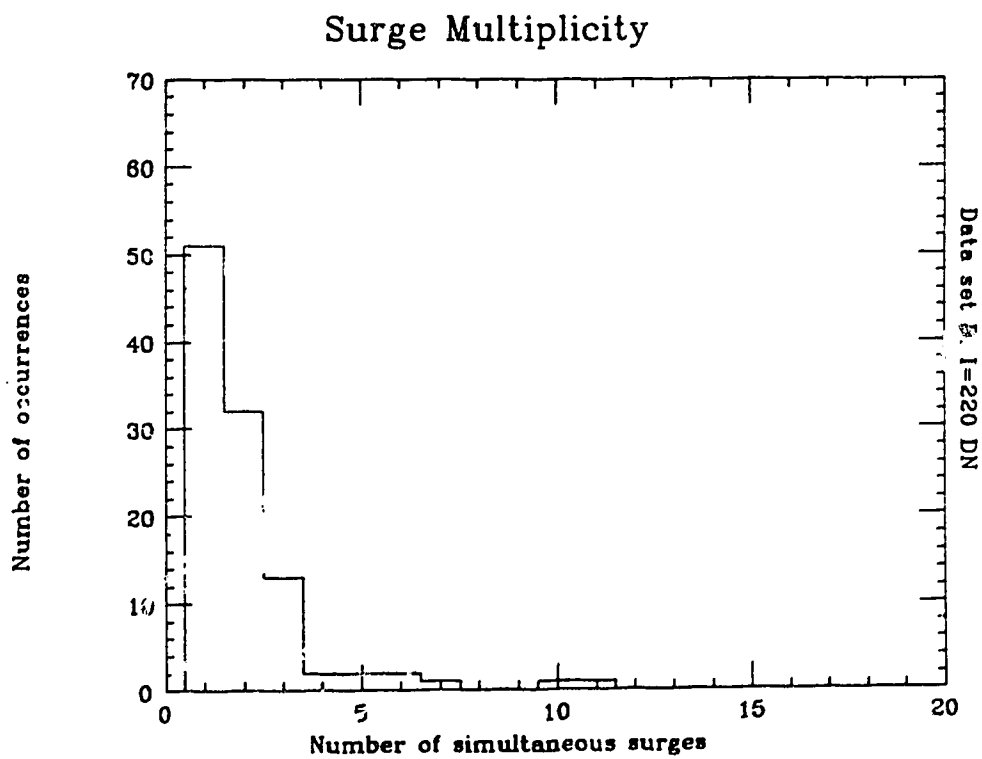
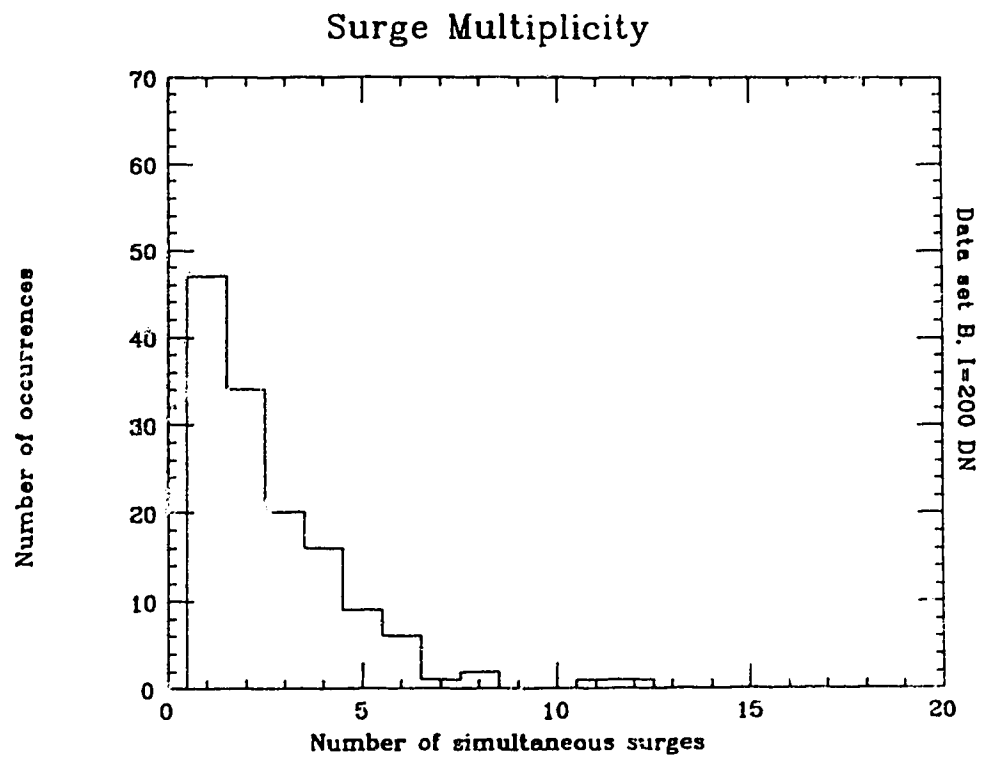


Figure 3.9 : Histograms of surge multiplicity



**Figure 3.10** : Histograms of surge multiplicity plotted at surge threshold intensity levels of 200 DN and 220 DN for data set B.

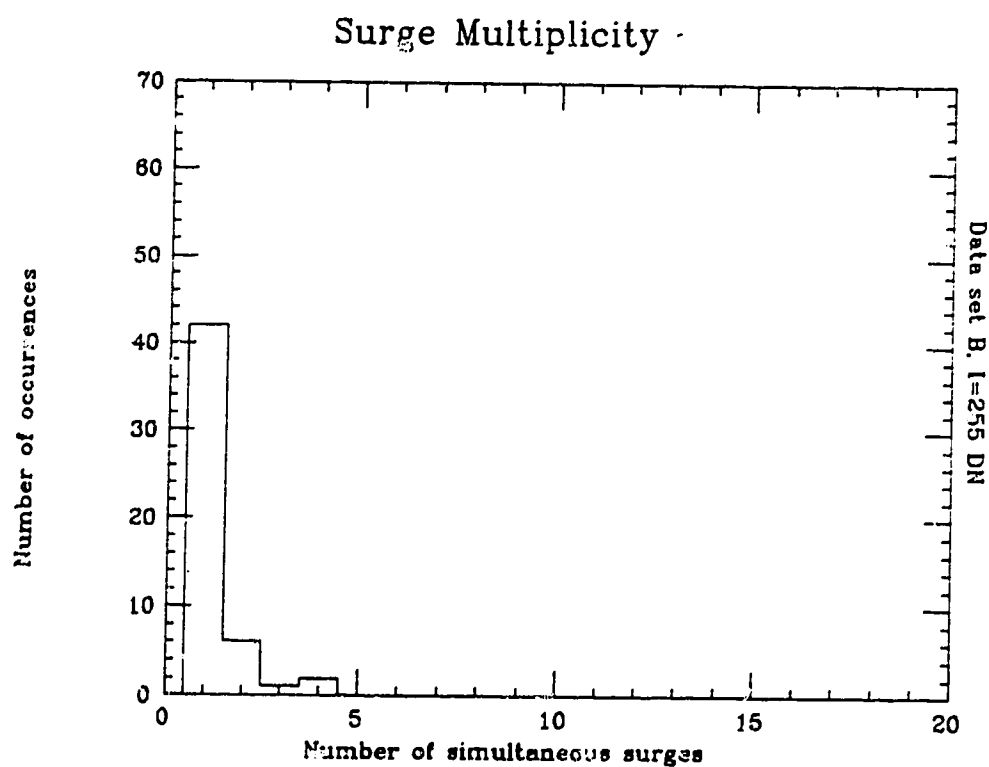
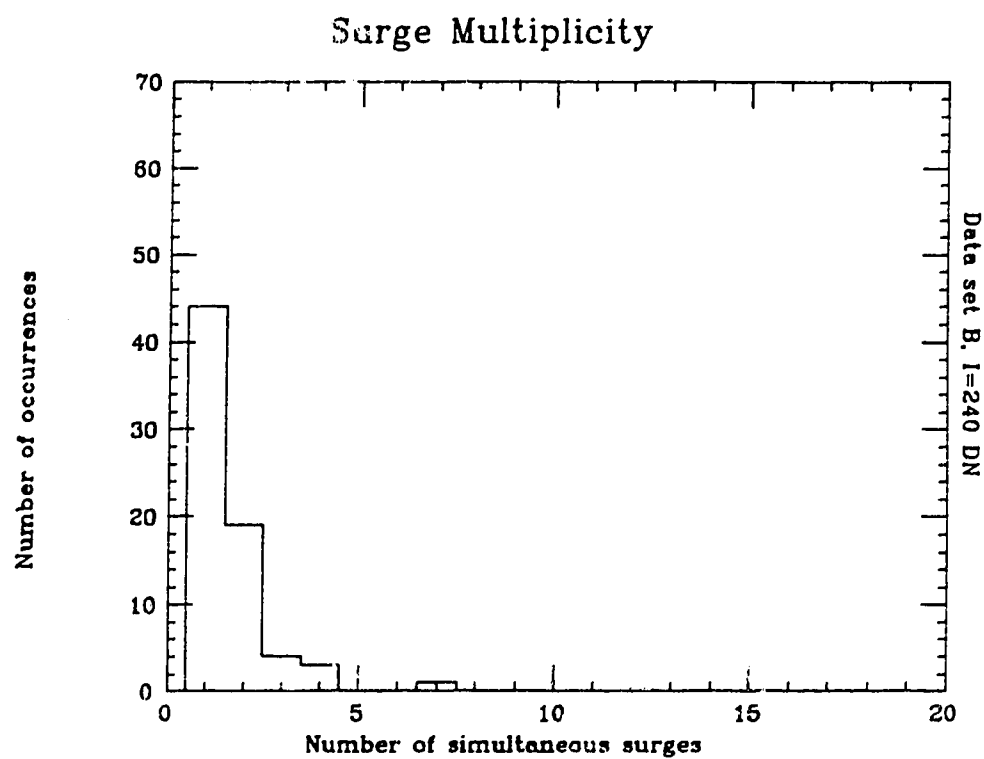


Figure 3.11 : Histograms of surge multiplicity plotted at surge threshold intensity levels of 240 DN and 255 DN for data set B.

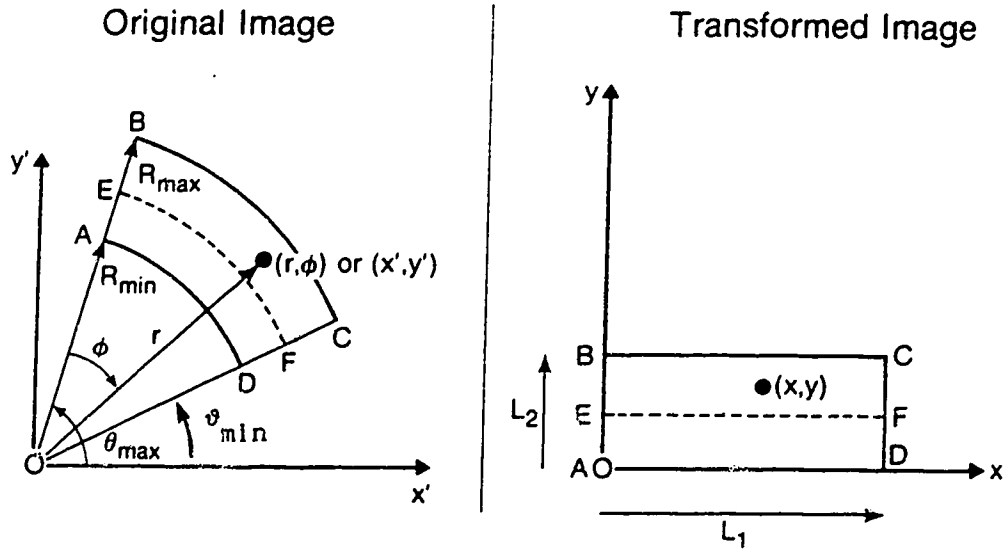
levels the percentage of events with high degrees of multiplicity is reduced.

### 3.7 : Fourier Analysis of Surge Multiplicity

In an attempt to analyse some of the features of surge multiplicity, two dimensional spatial Fourier transforms of selected images showing a high degree of surge multiplicity were performed. Previous attempts at transforming entire images to find periodic structures within the oval were unsuccessful in producing any significant results. As part of this project, an attempt was made to perform Fourier transforms, not of entire images but of portions of images embedded in the auroral oval. The approach adopted was as follows.

For each image, the region of the oval containing the surges was extracted. This was done by approximating the active section of the oval, as contained in the image, to a segment of a circle. The segment was extracted from the image by performing a geometric transformation that mapped it to a rectangular sub-image. Figure 3.12 shows diagrammatically the characteristics of the transformation and also gives the variables and coordinates that are used below to describe the transform mathematically.

The technique used to perform the image transformation numerically is called pixel filling and is defined as follows The



$L_1$  is chosen to equal the arc length EF

$L_2$  is chosen to equal AB

now with

$\phi \propto x$  and  $r \propto y$ , then

$$\phi = \vartheta_{\max} - \frac{x}{L_1} \left( \vartheta_{\max} - \vartheta_{\min} \right) \quad \text{and} \quad r = R_{\min} + \frac{y}{L_2} \left( R_{\max} - R_{\min} \right)$$

**Figure 3.12** : Diagram of outline of the geometric transformation from a circle segment to a rectangle.



final transformed image is defined on a set of coordinate axes  $X, Y$  with pixels referenced by discrete  $(x,y)$  coordinates and the original image is defined on a set of axes  $X', Y'$  with pixels referenced by discrete  $(x',y')$  coordinates. The transformation is defined in terms of two continuous functions  $f(x,y)$  and  $g(x,y)$  such that :-

$$x' = f(x,y)$$

$$y' = g(x,y)$$

In order to use the transformation, each pixel location  $(x,y)$  in the transformed image has its corresponding coordinates in the original image calculated from the functions  $f(x,y)$  and  $g(x,y)$ . However, these functions are not discrete and normally will not yield a discrete  $(x',y')$  location in the original image. Some form of interpolation is needed to find out which pixel value of the original image should be carried over to the transformed image. The simplest interpolation that can be performed is 'nearest neighbour' interpolation and this is what was actually used.

Finally, to perform the transformation, the functions  $f(x,y)$  and  $g(x,y)$  must be determined. These are the functions that, for the transformation that is required here, will yield a conversion from polar to Cartesian coordinates, including appropriate scaling factors. See figure 3.12 for geometry of this transformation. For this relatively simple case, an analytic expression for each function was found, though if this had not been the case, they could have been

approximated using numerical techniques. From inspection of figure 3.12, the basic form of the transformation can be seen. i.e.  $x$  varies linearly with the angular coordinate and  $y$  varies linearly with the radial coordinate. The basic polar to Cartesian transformation is given by :-

$$x' = r \cos (\theta_{\max} - \phi)$$

$$y' = r \sin (\theta_{\max} - \phi)$$

With the correct scaling factors applied, the transformation is defined explicitly as :-

$$x' = \left\{ \frac{y}{L_2} \left[ R_{\max} - R_{\min} \right] + R_{\min} \right\} \cos \left[ \theta_{\max} - \frac{x \phi_{\max}}{L_1} \right]$$

$$y' = \left\{ \frac{y}{L_2} \left[ R_{\max} - R_{\min} \right] + R_{\min} \right\} \sin \left[ \theta_{\max} - \frac{x \phi_{\max}}{L_1} \right]$$

By defining the bounds of a segment of the original image to be transformed, that segment could be extracted and appropriately transformed geometrically to form a rectilinear sub-image. This rectilinear sub-image was then Fourier transformed, with one axis of the transform representing information relating to structures concentric with the oval, and the other axis of the transform pertaining to structures aligned perpendicular to the oval.

One disadvantage of the technique was the approximation made in taking the active region of the oval to be the segment of a circle. Because the UV images were projections of the actual auroral oval, a certain amount of flattening and distortion of the oval took place when this essentially spherical surface was mapped onto the image plane. Approximating this projection distortion by a circle, rather than a sphere, was done in order to define the geometric transformation in relatively simple terms.

Distance scales of the sub-images were deduced by following control points in the image as it was extracted and transformed. The standard techniques of numerical Fourier analysis were followed when calculating the transforms of sub-images : linear trends in the data were removed by subtracting the best fitting plane from each sub-image (determined by a least squares method) and the data were appropriately windowed using a cosine bell. Details of these techniques are explained in appendix III.

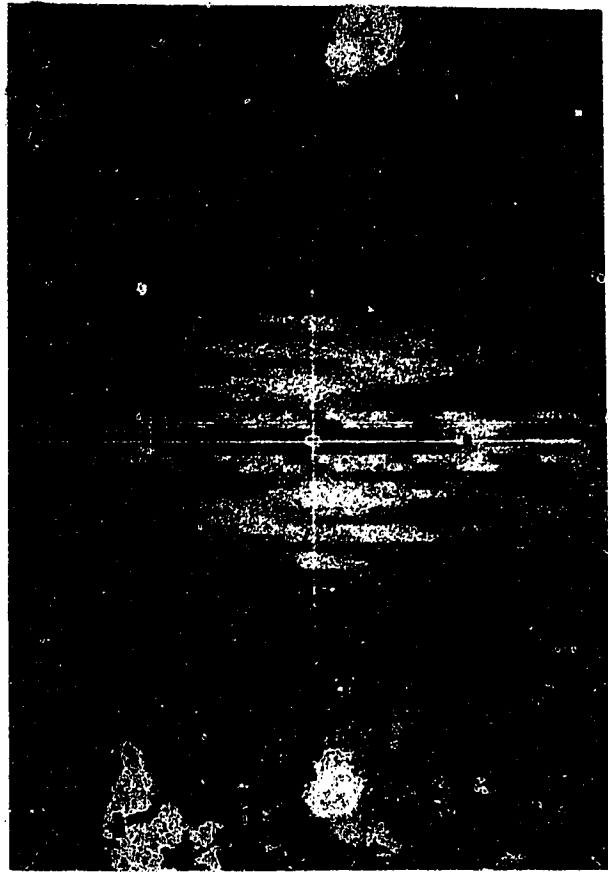
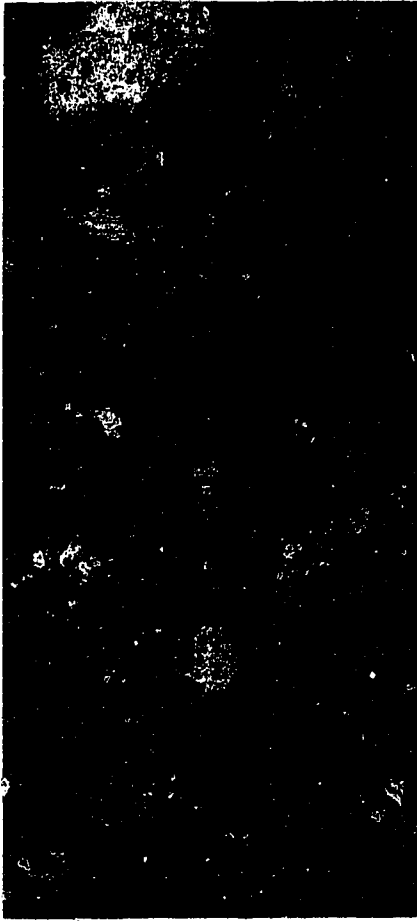
Three images showing a high degree of surge multiplicity were analysed : 236 21.009 (Plate 2.1(a)), 236 21.004 and 236 10.008 (plate 3.2(a) and 3.2(b), respectively). The resulting Fourier transforms showing a variety of spatial periodicities in surge location, are summarised in table 3.2.

Plate 3.2

|        |        |
|--------|--------|
| 3.2(a) | 3.2(c) |
| 3.2(b) | 3.2(d) |

3.2(a) : One of the images showing a high degree of surge multiplicity that was analysed for periodic structure by taking the two dimensional spatial Fourier transform of the active portion of the auroral oval.

3.2(b), 3.2(c) and 3.2(d) : A sequence of plates showing some of the stages of the two dimensional spatial Fourier transform analysis. 3.2(b) shows the original image, 3.2(c) shows the geometrically transformed and extracted sub-image of the active portion of the oval and 3.2(d) shows the result of taking the two dimensional spatial Fourier transform. The colour bar for the Fourier transform is logarithmic (base 10). Peaks in the intensity located at  $\pm 7$  pixels from the origin on the horizontal axis are thought to be the result of periodicity in the sub-image.



| Table 3.2 : Summary of Fourier Analysis of Surge Multiplicity |                              |                           |
|---|------------------------------|---------------------------|
| Image   | Arc length of sub-image (km) | Periodicities Found (km)  |
| 236 21.009  | 2700                         | 2700, 1350, 900, 540, 450 |
| 236 10.004  | 2900                         | 725, 580, 483, 414, 341   |
| 236 10.008  | 2900                         | 1160, 528, 387, 277       |

From these results, it is clear that despite taking all of the standard precautions normally adopted when working with Fourier transforms, the periodicities found reflect contamination from the replication periodicity of the sub-image. Of the periodicities listed in table 3.2, all of those listed for image 236 21.009 and all except the 341 km for image 236 10.004 are the result of integer divisions of the arc length of the sub-image.

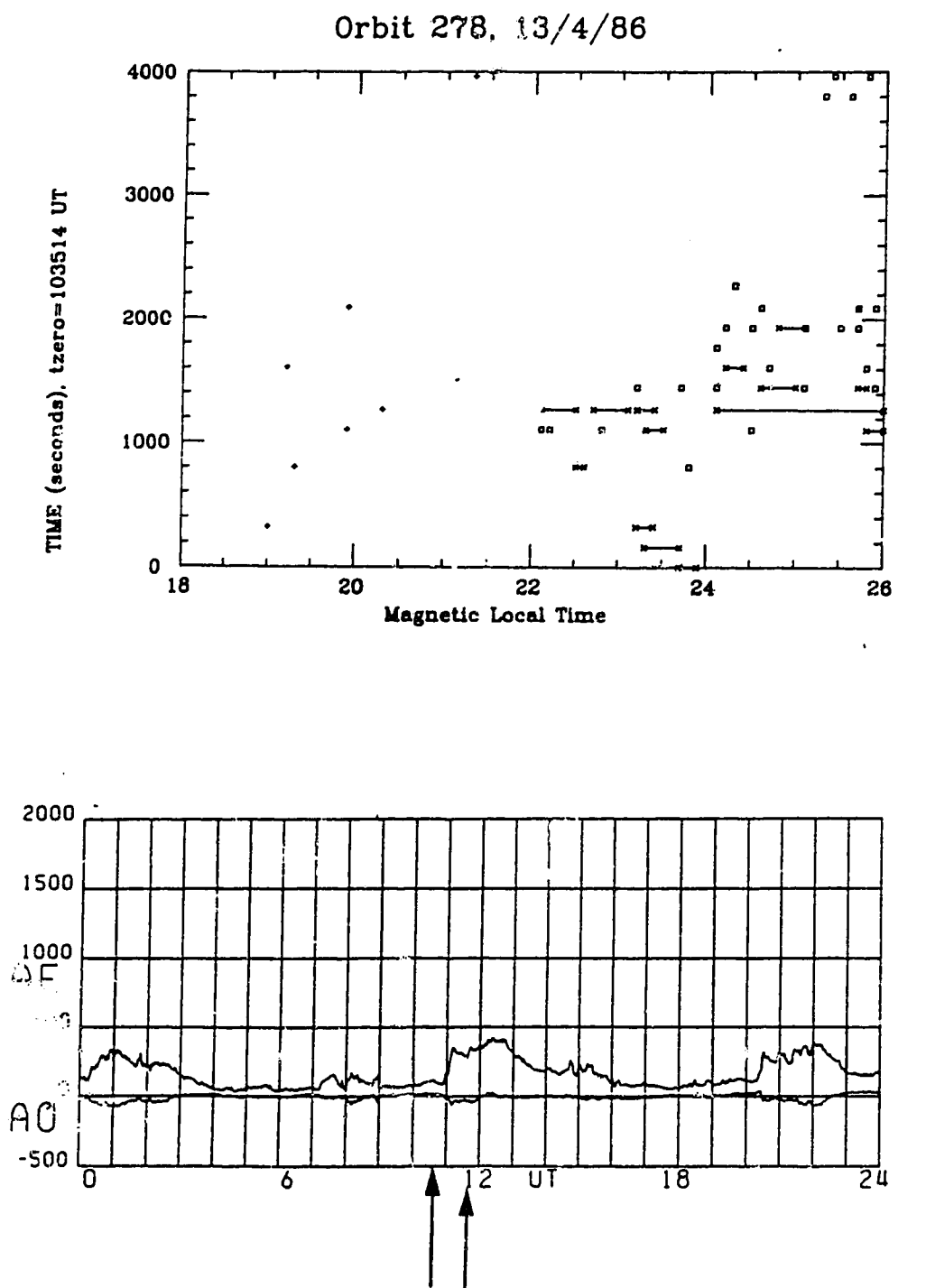
As an example of how the analysis technique was implemented, a typical sequence of analysis steps involving the original image, its extraction, geometric transformation and finally its amplitude spectrum, calculated from its Fourier transform, is shown in plate 3.2(b) to 3.2(d). Note that the zero frequency origin of plate 3.2(d) is located in the center of the square array of the amplitude spectrum.

In work that was carried out subsequent to the completion of

material for this thesis, the Fourier analysis of surge multiplicity was repeated using a slightly different algorithm to calculate Fourier transforms. Instead of using a standard Fast Fourier Transform routine, a 'mixed radix' routine written by Singleton (1968) was used. This routine did not require the number of data points to be transformed to be padded with zeros to the next integer power of two. The result of not padding the image data with zeros produced amplitude spectra that were free of much of the noise that is present in the spectra presented here, but still showed periodicities ranging from  $\approx 300$  km to  $\approx 500$  km.

### 3.6 : Substorm Development

VIKING provided relatively few sequences of images that showed the complete development of a substorm, but a number of sequences showing part of the lifetime of a substorm exist. In trying to analyse some of these sequences, the latitudinal position of surges was ignored and only the longitude co-ordinate tracked as time progressed. Plots of substorm evolution were then made by plotting the MLT co-ordinate of all surges within a given image along the abscissa and using the UT of the image as the ordinate. Figures 3.13 and 3.14 give some examples of this substorm evolution. Also shown with these examples are plots of the AE index of auroral zone activity (see Rostoker (1972) for a definition and discussion of this index). These AE plots are useful in that they show where the VIKING image sequences of substorms are located within the overall substorm.



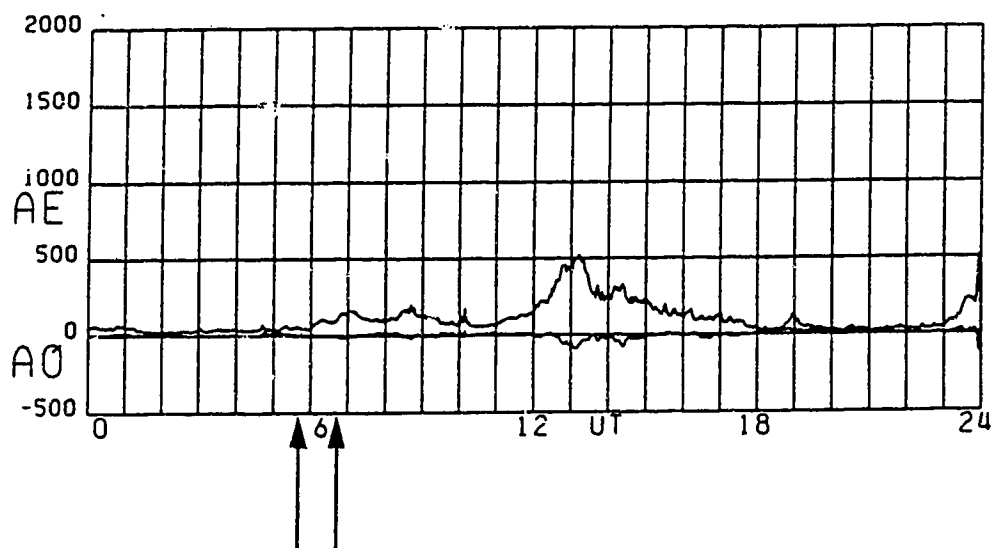
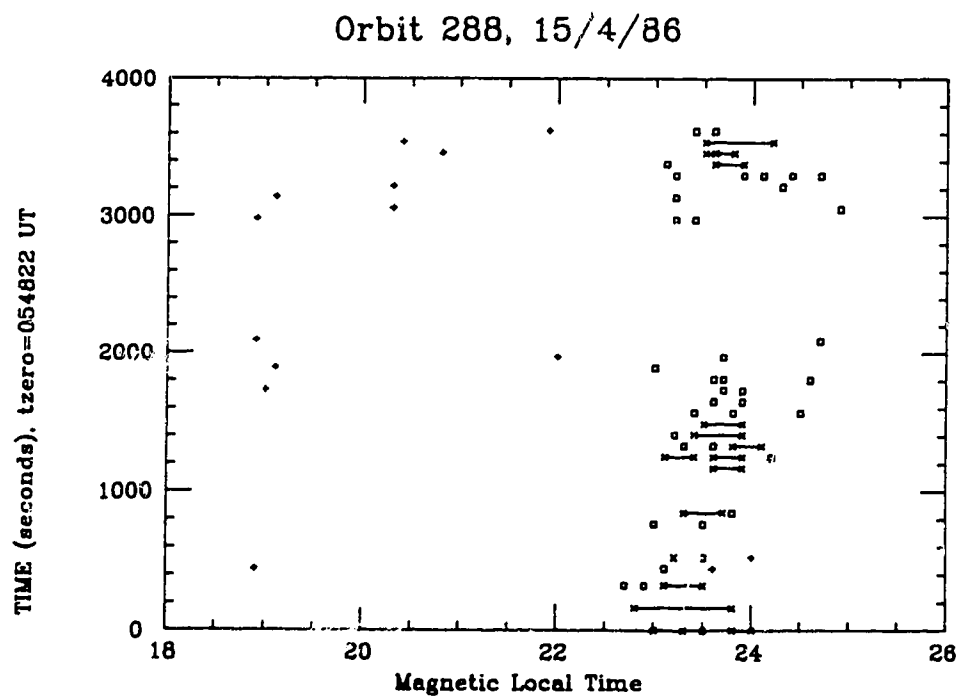
□ represent surges.

x—x represent large surge features, with an 'x' located each end of the feature.

+ represents the limit of the field of view of the camera

**Figure 3.13** : Example plot of substorm development with accompanying AE records.





- represent surges.
- x—x represent large surge features, with an 'x' located each end of the feature.
- + represents the limit of the field of view of the camera

**Figure 3.14** : Example plot of substorm development with accompanying AE records.

A couple of problems were encountered in trying to obtain sequences of substorm evolution. One difficulty was that the field of view of the camera often prevented the entire evening sector from being viewed, and the other problem centered on the determination of corresponding surges between successive images. Specifically, this was to do with deciding if a surge moved during the time interval between images, or whether a new surge form appeared at a location close to an existing surge with the previous surge dropping below the detection threshold.

Inspection of the AE plots and the evolution sequences reveals little that is new about the development of the substorm, but there are still some important points to be made. One case of the substorm evolution shows that there is activity taking place early in the evening sector, close to 1800 and 1900 MLT while there is no activity taking place at later times in the evening sector. Several cases also show that as the level of surge activity decreases, the last MLT sector to still contain surges may be close to midnight. It is stressed that this observation is based on very few cases and should not be taken as having been typical. For this to be done, many more sequences of substorm evolution would need to be analysed.

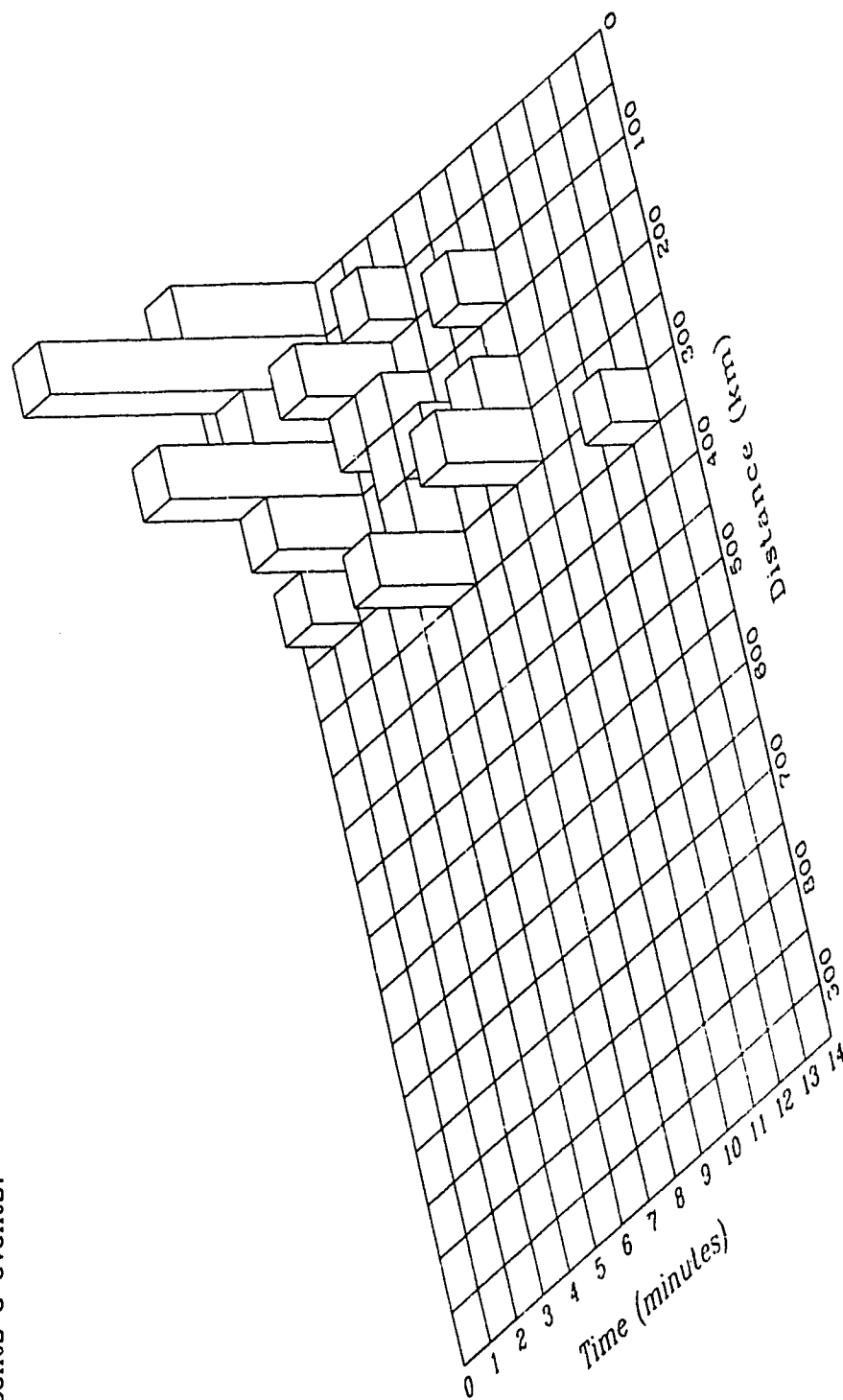
For cases where it was possible to track surge features from one image to the next, data were compiled on the maximum distance that surges moved in a westerly direction and the time it took for surges

to travel that distance. These results were then plotted on a two dimensional histogram and are shown in figure 3.15. This histogram shows that for the majority of cases, surges do not move very far. For the cases where it appeared surges had travelled several hundreds of km, careful inspection of the images showed that this westward motion was in actual fact the expansion of a region of surge activity, rather than the propagation of a surge feature. At no time was a single surge seen to propagate over a significant portion of the evening sector.

Tracking surges between successive images enabled the velocity at which surge features moved to be determined. When the data comprising figure 3.15 were analysed to find surge velocities, the most probable velocities were found to be between 20 km/min and 40 km/min. It should be noted that these velocities were corrected for the rotation rate of the Earth.

Finally, evidence gathered from part of one particular substorm shows that surges undergo significant changes in intensity between images even when the images are separated by only 20s. This pulsating of surge intensity does not appear to be the result of the VIKING camera and is genuinely a pulsation of localised auroral luminosity. Though not pursued in this thesis, these pulsating surge features warrant further investigation.

**Figure 3.15 :** A two dimensional histogram of the maximum distance moved in a westerly direction by surges versus time. Time zero is taken for each surge as the time it first was first detected. Time bins are 1 minute wide and distance bins are 50 km wide. Vertically, the tallest bin represents 6 events.



## 4 : DISCUSSION AND CONCLUSIONS

### 4.1 : Summary of Results

With a surge threshold intensity level of 180 DN, the statistical survey of surge distribution and multiplicity in the evening sector yielded a number of interesting results. The most probable MLT zone in which surges were found was from 2300 to midnight. Surge multiplicity was observed to occur frequently, with  $\approx 35\%$  of surges seen as individual and isolated features, though of the possible degrees of multiplicity, this was the most likely to occur. A lower limit to the absolute frequency of surge activity in the evening sector was set at 15%.

These statistical results are based on data from two 50 orbit sets of images from VIKING and were acquired between April 5 - 23, 1986. To check that the results apply to typical magnetospheric conditions, the average level of geomagnetic activity, as measured by  $K_p$ , (see Rostoker (1972) for a description of this index of activity) for each 50 orbit data set was calculated. For both data sets, this was found to be 2 $\circ$ , which is just below the generally accepted average value of 2+.

Two dimensional spatial Fourier analysis of the auroral luminosity distribution was carried out, but only for a small number of cases. This technique was tried as an example of a possible form of

analysis that may yield interesting results and could be repeated over a larger number of events if it looked promising. For the one event where Fourier analysis yielded relatively clear results, periodic structure in the intensity distribution along the auroral oval in the vicinity of surges was found with typical wavelengths ranging from 300 km to 500 km. These wavelengths were for structures in the oval occurring between 2250 and 0110 MLT.

Sequences of images showing parts of substorm development indicated that the Akasofu picture of substorm development described in chapter 1 (§1.6) did not generally apply : 1) no clearly defined westward travelling surges were seen; 2) there were a large number of events where there was a high degree of surge multiplicity. For cases where surges could be tracked between images, typical velocities ranged from  $\approx 20$  km/min to  $\approx 40$  km/min.

#### 4.2 : Discussion of Surge Multiplicity

The concept that more than one surge can be simultaneously observed in the evening sector of the auroral oval is not new and has been reported by a number of other researchers: e.g. Pytte et al. (1976) analysed magnetometer signatures of multiple substorm intensifications, Sergeev (1974) noted the existence of multiple surges and Frank and Craven (1988) observed multiple surges in global satellite images from the Dynamics Explorer 1 satellite. Wiens and

Rostoker (1975) have suggested that stepwise poleward motion of the westward electrojet (figure 4.1) results in multiple simultaneously observed regions of westward electrojet. At the discontinuities in current flow between these regions and the eastward electrojet they suggest surges are formed. The typical timescale of the stepping motion is  $\approx 10$  minutes. The degree of multiplicity observed with VIKING appears to be consistent with the degrees of multiplicity that could result from multiple electrojet regions.

If one interprets surge multiplicity in terms of the Boundary Layer Dynamics model of substorms, there will be a very close, if not direct, correspondence between the number of surges seen and the number of spatial locations at the LLBL/CPS interface where there is large wave amplitude resulting from the growth of the KHI. In other words, there should be a relationship between the wave number of the KHI at the LLBL/CPS interface and the spacing of surges in the ionosphere, and this relationship should be represented by just a scaling factor. Using this postulate, various parameters of the KHI and the parameters of a magnetic field mapping scheme between the magnetosphere and ionosphere can be checked for self consistency, as shown below.

Using the idea that field lines between the ionosphere and the locus of points representing the intersection of the equatorial plane and the LLBL/CPS interface are 'stretched' progressively with

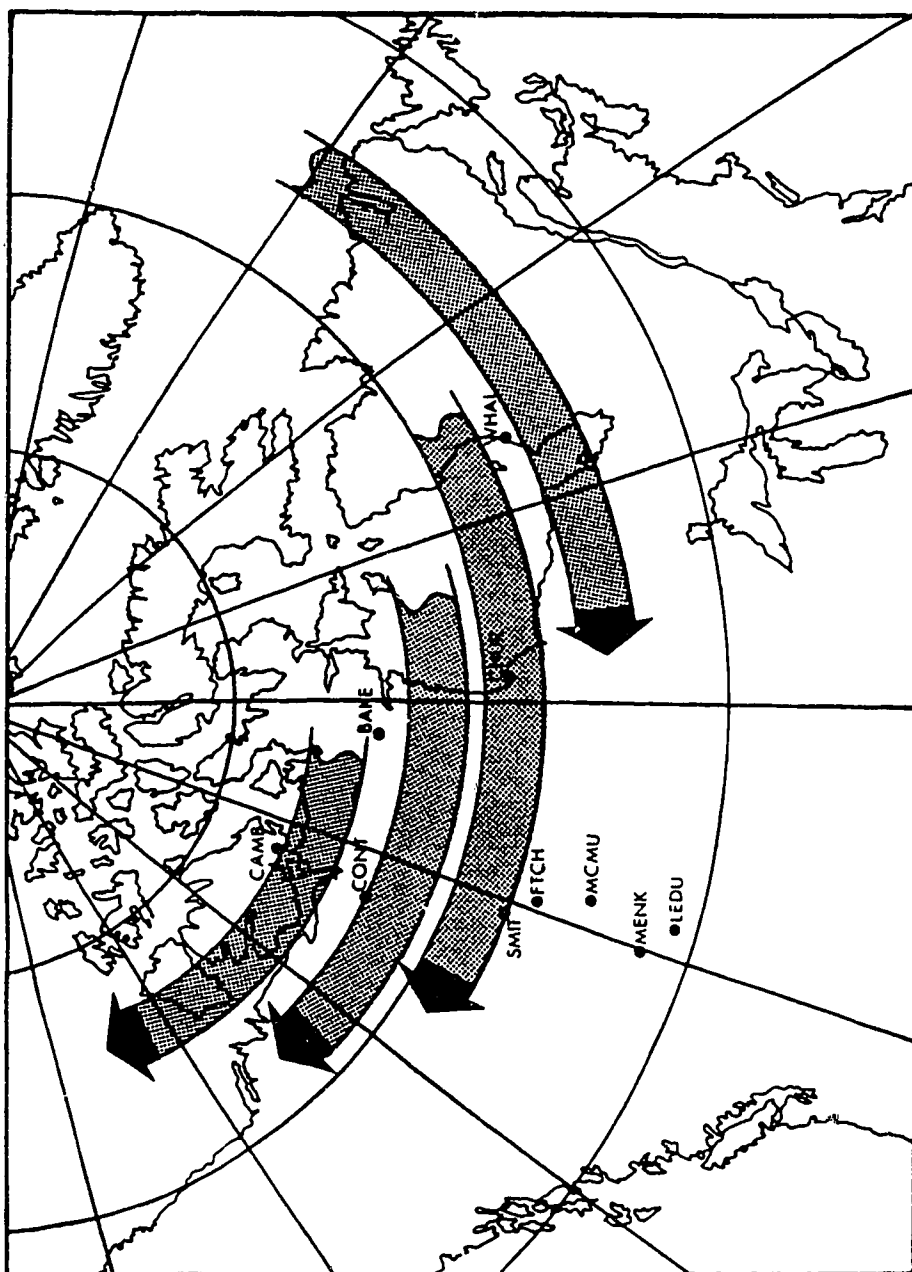


Figure 4.1 : Poleward steps of the westward electrojet, from Wlens and Rostoker (1975).



increasing MLT in the evening sector (an idea used by Rajaram et al. 1986), a crude model of a mapping between the two regions can be developed. Figure 4.2 shows the stretching that takes place for the field lines from the ionosphere to the LLBL/CPS interface as calculated by the Tsyganenko (1987) model of the magnetic field of the magnetosphere. These magnetic field lines are from the poleward edge of the auroral oval and map to the LLBL/CPS interface in the magnetotail (Lui et al. 1987; Rostoker 1983). The distance between successive field line crossings of the equatorial plane is clearly seen to increase with increasing distance downtail, i.e. with increasing MLT. Unfortunately the Tsyganenko model becomes less reliable the further away from the earth the field is modelled and so will not be used in this case to map from the ionosphere to regions close to the neutral line. Instead, a crude model of the field line stretching will be used. The ingredients of this model include the progressive stretching concept discussed above and a restriction that midnight MLT will map to the distant neutral line at around  $115 R_E$  (Slavin et al., 1985).

If the field line stretching is such that it is proportional to the distance between a field line foot in the ionosphere and where that field line crosses the neutral sheet, then the distance  $L_n$  from point 'n' in the ionosphere to the neutral sheet is given by

$$L_n = L_{n-1} + \alpha L_{n-1} \quad (\text{Eqn 4.1})$$

where  $\alpha$  is the fractional increase in distance from the ionosphere to

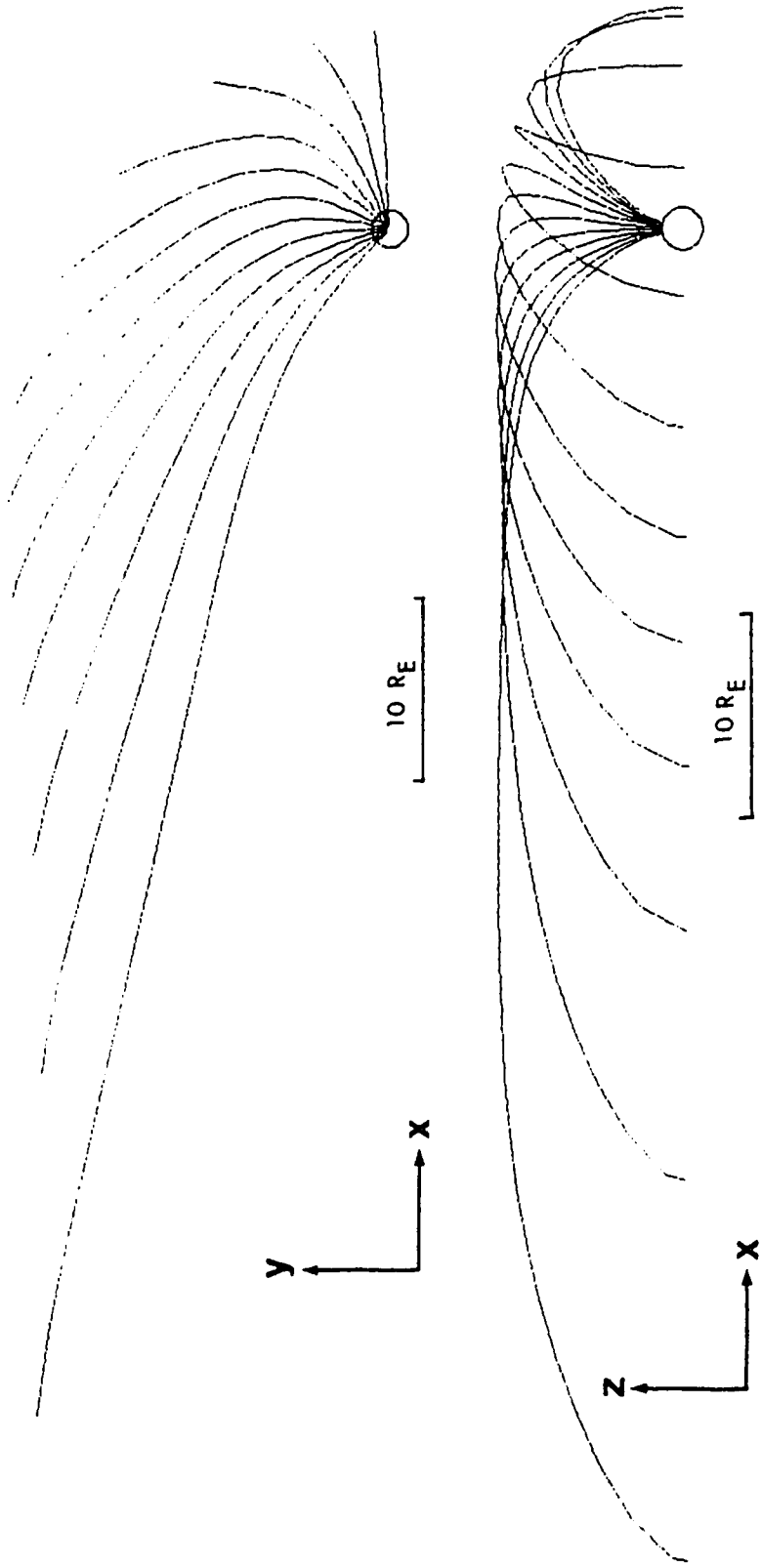


**Figure 4.2 :** Plots of the Tsyganenko model field line tracing into the magnetotail. The field lines originate in the ionosphere at a latitude of 65 degrees (eccentric dipole coordinates) and are spaced at 20 degree intervals of longitude. Courtesy of E. Donovan.

the neutral sheet. Figure 4.3 sets out the geometry of these distances in the equatorial plane of the magnetotail. The non-recursive form of equation 4.1 is

$$L_n = L_0 \sum_{m=0}^n \binom{n}{m} \alpha^m \quad (\text{Eqn 4.2})$$

where  $L_0$  is the distance between the ionospheric footprint and the neutral sheet crossing at  $n=0$  and the  $\binom{n}{m}$  are binomial coefficients.

To proceed further with this model, values of  $L_0$  and  $\alpha$  have to be introduced. The initial starting point of this model,  $L$  for 1600 MLT is  $\approx 15 R_E$ , was taken from the Tysganenko model and once  $L_0$  was fixed, then so was  $\alpha$  (for a given distance to the neutral line). A plot showing the distance from the ionosphere to the neutral sheet as a function of MLT for various values of distances to the neutral line is shown in figure 4.4. It should be stressed that this rather crude model of a mapping scheme has some serious limitations which are the result of the assumptions that the stretching factor  $\alpha$  does not itself change with distance and that the geometry employed is actually applicable. The mapping scheme should be able to yield order of magnitude estimates of corresponding distances along the LLBL/CPS interface to those in the auroral oval. The ratio of LLBL/CPS distances to the ionospheric distance is termed the *mapping factor*.

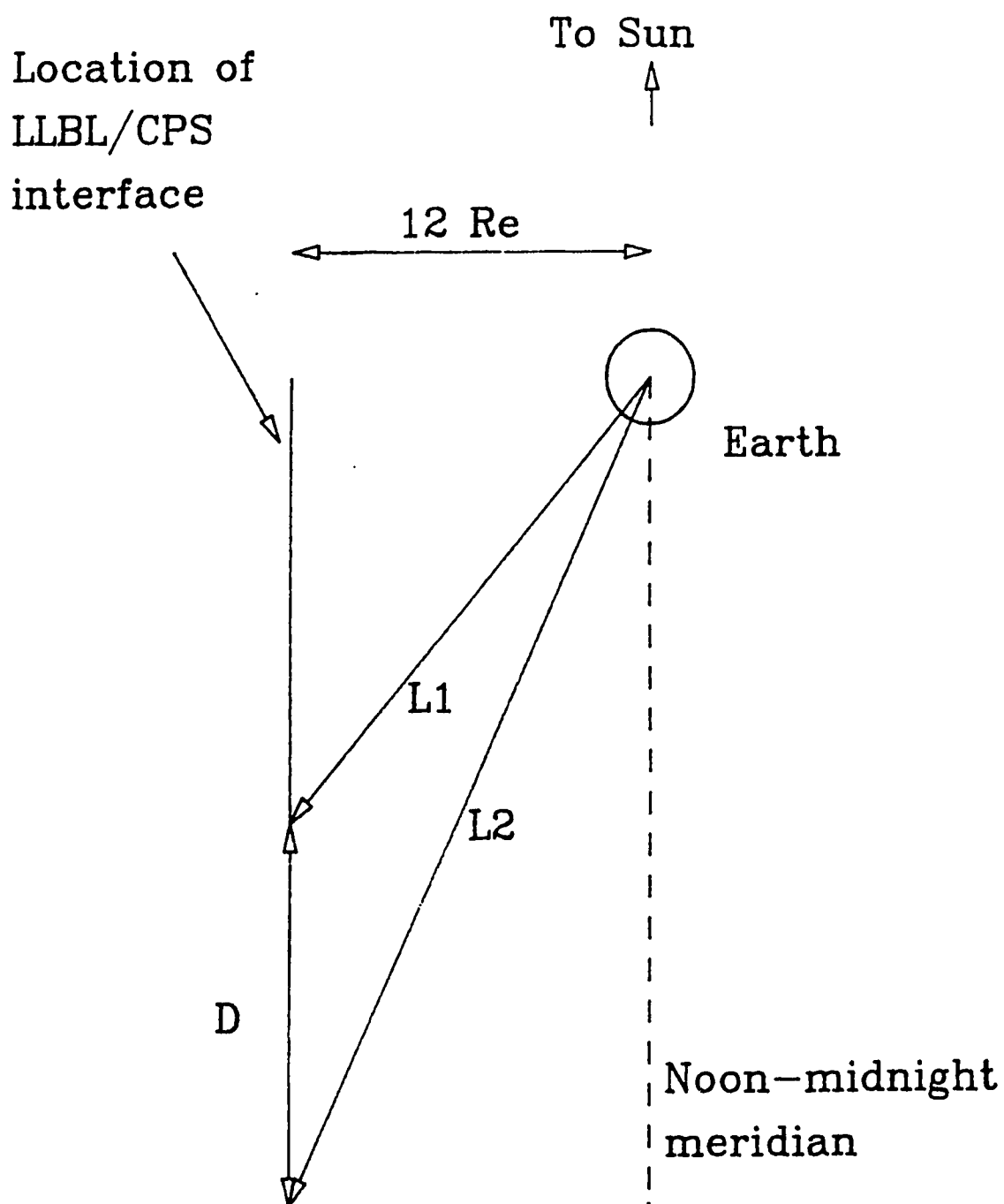


**Figure 4.3** : Geometry of the 'proportional stretching' mapping model developed to determine ionosphere-magnetosphere mapping factors.

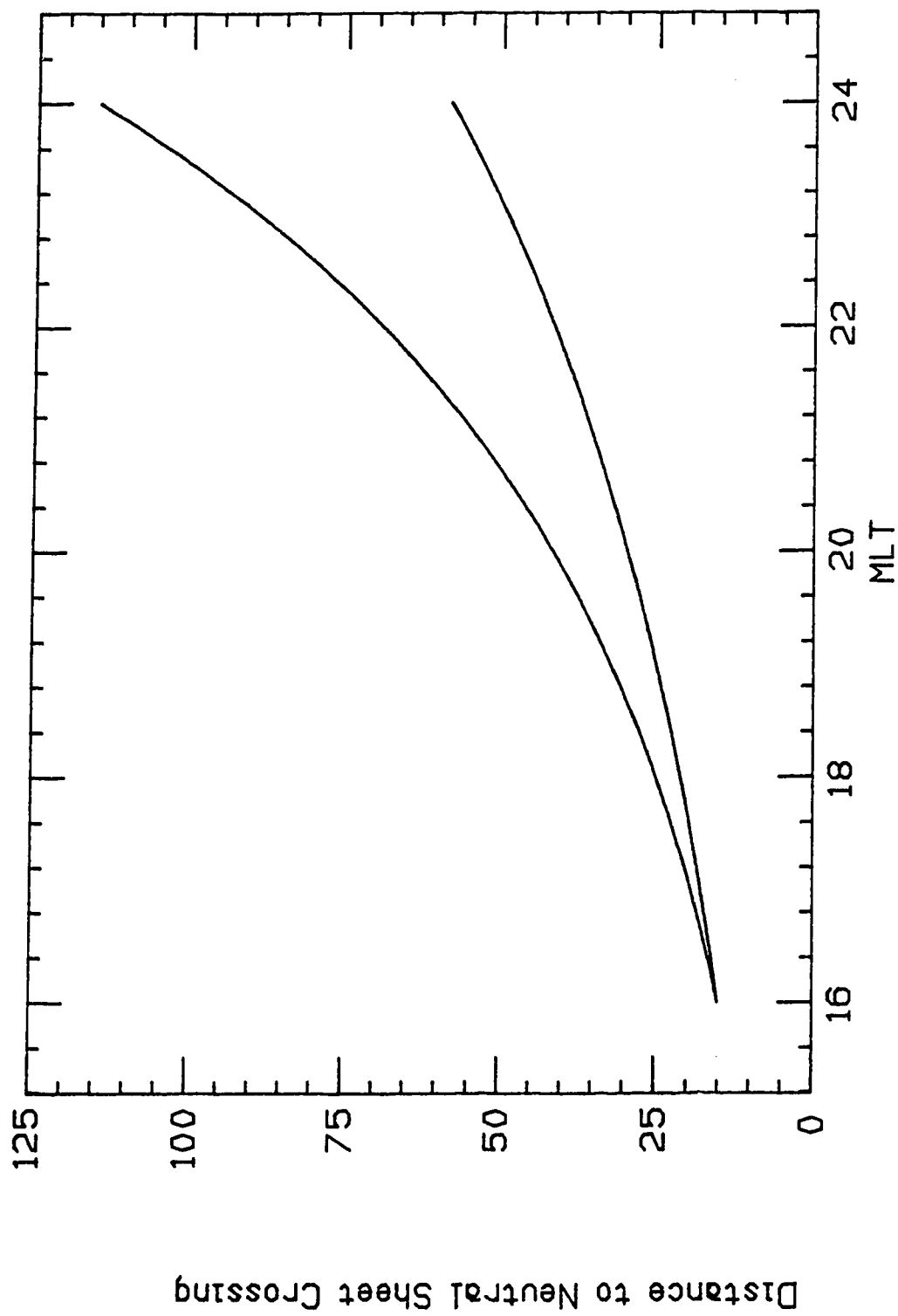


Figure 4.4 : Plot of neutral sheet crossing versus MLT for 2 values of the stretching coefficient  $\alpha$ .

As described in the introductory chapter (§ 1.7), there are a number of parameters that control the growth rate coefficient,  $\gamma$ , of the KHI. In addition to the parameters already discussed, an additional constraint is imposed when finding the maximum  $\gamma$  and this occurs when the region of the KHI has finite width (Walker, 1981), viz.

$$kD \approx 0.6 \quad (\text{Eqn 4.3})$$

where  $k$  is the wave number for the instability and  $D$  is the width of the velocity shear zone.

It is quite possible that surge features are a result of regions of the LLBL/CPS interface that have experienced a maximum growth of the instability, so the  $kD \approx 0.6$  criterion should apply to their generation. Now consider the results of the two dimensional spatial Fourier analysis which yielded typical values of  $\lambda$  in the ionosphere ranging from  $\approx 300$  km to  $\approx 500$  km. Using mapping factors derived from the mapping model described above, Table 4.1 lists various stages in the calculation of the range of  $D$  values that are possible.

| Table 4.1 : Limits of the KHI parameters |                                 |                |  |
|--|---------------------------------|----------------|--|
| Ionospheric Wavelength (km)              | Neutral Line Distance ( $R_E$ ) | Mapping Factor | Width of zone of Instability ( $R_E$ ) |
| 300                                      | 60                              | 84             | $D_{\min} \approx 0.4$                 |
| 500                                      | 115                             | 200            | $D_{\max} \approx 1.5$                 |

The range of possible D values is not unreasonable for the width of a velocity shear zone in the magnetotail, and so one can have expectations of the KHI operating and producing field aligned currents originating in the magnetotail. These currents can then be driven through the ionosphere, producing surges as one of their properties, as discussed in chapter 1 (§1.7).

Unfortunately, the same level of verification and testing that has been demonstrated above for the Boundary Layer Dynamics model of substorms cannot be applied to the Near Earth Neutral Line model. In this model, if surges are generated on a one to one correspondence with plasmoids, then it follows that multiple plasmoids must exist. With the processes of plasmoid formation not yet understood, the Near Earth Neutral Line theory has a long way to go before an explanation of multiple surges can be given. Alternatively, formation of one plasmoid may give rise to multiple surges if the earthward moving electrons are somehow azimuthally arranged into beams, with each beam producing a surge. The discrete nature of the auroral forms seen with VIKING would seem to suggest that this arranging of precipitating electrons takes place close to the earth and may take place at altitudes below the accelerator region. Again, there has not yet been enough development of the theory to suggest any mechanism that can be tested with data.

As a final remark about surge multiplicity, pulsating surge forms which were seen during a number of cases of multiple surge events, could have a variety of causes. These causes fall into the two broad categories of magnetotail causes and near earth (one or two  $R_E$ ) causes. The magnetotail causes include such possible effects as 1) the modulation of the KHI growth coefficient by, say, changing the  $B \cdot k$  damping term; 2) modulation of plasma densities and flow velocities at a neutral line (be it near earth or distant); 3) the modulation of plasma particle pitch angles and thermal velocities, again by varying reconnection. Processes closer to the earth that might be causes are modulations of the electron accelerator, perhaps by the bouncing of Alfvén waves between the ionosphere and the outer magnetosphere, as described by Kan et al. (1988).

#### 4.3 : Discussion of the Distribution of Surges

The result from this thesis that the most likely MLT sector in which to find surges is from 2300 to midnight is consistent with the maximum in geomagnetic bay occurrence (Romana and Cardus, 1962) and from inferences from optical data (Frank and Craven, 1988). However, careful inspection of the graphs of surge distribution hint at some potentially interesting results. The rapid fall off in the number of observations of surges between midnight and 0100 MLT could have several possible causes.



One possibility is that a portion of the auroral oval at 0100 MLT maps to the region of the neutral line and, as a result, little surge activity is observed in this time zone. For this mechanism to work it is necessary for the separator line between open and closed field lines (on which the neutral line is thought to be located in the BLD model) to run across the tail with only a small component of its locus parallel to the interface between the LLBL and CPS. With this geometry, there will be little shear flow adjacent to the neutral line and hence little possibility of generating surges through the KHI.

Alternatively, if it is assumed that a small portion of the auroral oval at *midnight* maps into the magnetotail to the region of the neutral line, then it is possible that the asymmetry in surge distribution is a result of an asymmetry in the magnetotail. One likely candidate is the magnetotail electric field, which is a superposition of the dawn-to-dusk field and the co-rotation electric field. The co-rotation electric field (which is directed radially inwards from the magnetosphere to the earth) is generated because the earth's magnetic field co-rotates with the earth. The resulting potential drop between field lines from the poles of the earth and field lines from the equator is  $\approx 80$  keV (Hines 1974).

Yet another possibility is that field aligned currents flowing between the magnetotail and the ionosphere distort the uniform regular mapping scheme causing asymmetries and irregularities in the mapping. It

is beyond the limits of the data presented in this thesis to try and evaluate the actual cause, or causes, of the distribution of surges. Certainly, more data from the dawn sector would need to be analysed to further the testing of possible causes.

A note of caution should be included here. The discussion of the preceeding paragraphs may have given the impression that in the ionosphere, evening sector MLT's map into the magnetotail on its dusk side and that dawn sector MLT's map to the dawn side. This is not always the case. The data in this thesis are ordered in terms of MLT (which is associated with geomagnetic eccentric dipole coordinates, as described by Hakura (1965)) because it has been found during the evolution of magnetospheric physics in past decades that this coordinate system orders the data better than local time (which is based on geographic coordinates). It is more than likely that during disturbed times (e.g. substorms), the mapping of MLT zones into the magnetotail is distorted from the average state of affairs as described above. An example of this can be seen in plate 2.1(a), where structures originating in the evening sector extend through midnight and into the MLT post-midnight sector of the oval. The degree of continuity of structures between the evening and dawn sectors leads one to conclude that all of the continuous structure shown in plate 2.1(a) map to one side of the magnetotail, namely the dusk side. This is just one of many examples showing that the magnetosphere is a very dynamic structure and that to talk about it having fixed conditions

and parameters can lead to confusion.

The fact that there is a greater likelihood of detecting surges in the 2300-2400 MLT sector means that this region of the auroral oval maps into the region of the magnetotail that is most sensitive to any instability. This is regardless of whether it is plasmoid formation, or a region of KHI. The decrease in the number of surge events observed with decreasing MLT as measured from midnight can again be explained in terms of either model. For the BLD model, generation of the KHI would most likely be reduced at locations closer to the earth than at locations immediately earthward of a distant neutral line. This is because earthward flowing plasma in the CPS will slow down as the CPS thickens earthward of the neutral line. This can be inferred from the continuity equation, which can be stated for incompressible fluid flow as

$$\rho v A = \text{const} \quad (\text{Eqn 4.4})$$

where  $\rho$  is the mass density,  $v$  the flow velocity and  $A$  the cross sectional area of the flow perpendicular to  $v$ . It can be seen that either or both of the mass density and fluid velocity must decrease as the cross sectional area of the flow increases as the plasma moves earthward. This decrease could easily reduce the possibility of growth of the KHI at locations close to the earth (and hence at MLT's at earlier times in the evening sector). A further observation is that closer to the earth,  $B$  becomes closer to being perpendicular to  $k$ . The magnitude of the growth rate coefficient,  $\gamma$ , is reduced by a term

involving  $B \cdot k$ , so it is possible that  $\gamma$  will be larger closer to the earth. However, one should note that  $B$  itself will increase in magnitude closer to the earth. The increasing  $B$  could also cause the plasma fluid velocities to decrease which would reduce the likelihood of generating the KHI. More theoretical work will need to be done to see which of these effects dominates.

The Near Earth Neutral Line model could explain the distribution of surges if one were to suggest that plasmoid formation is more likely to occur at locations close to the noon-midnight meridional plane. This is not unreasonable because the plasma sheet is thinner in its centre than at its flanks.

Before the discussion of the distribution of surges in the evening sector is concluded, some comments are in order for one the features noted in data set B, figure 3.5. This plot has a local maximum at 1900 MLT which does not fit the general trend of the decreasing number of surge events at successively earlier MLT's, nor is there a local maximum observed at such times in the corresponding plot for data set A. In fact, it was discovered, after a review of the data, that the majority of surges recorded at these times were found to be from one orbit. The images from this orbit showed a high degree of atmospheric day glow at local times well into the evening sector, and it was concluded that this glow was raising the observed luminosity of structures in the oval. Thus, some structures and surges

artificially exceeded the threshold level of 180 DN and were recorded. The satellite image display software (SYSTEM) could not make any corrections for this effect and so these contaminated data were included in the data base that was analysed. The reason why more events of this nature might not have been recorded in data set A was because that data set was taken from images that were taken earlier in the year than those of data set B. The time of year (April) meant that for each successive orbit of the satellite, more of the northern hemisphere auroral oval was in daylight.

#### **4.4 : General Comments on Substorm Development**

There were not enough data analysed to accurately determine the development of a substorm from the expansion phase through to the recovery phase. As well, the data obtained usually constituted only part of a substorm sequence because the average length of a substorm is longer than the typical viewing time for which VIKING provided sequential images of substorm development. However, the periods of activity that showed either the western or eastern boundary to move do indicate that changes either in the location of source regions of surges or in the plasma characteristics in regions of potential surge sources occur in the magnetotail during a substorm. Such changes and variations can be interpreted in terms of the boundary layer model as the KHI occurring at various locations along the LLBL/CPS interface. Once initiated, the KHI waveform can propagate earthward

(corresponding to westward motion in the evening sector) or anti-earthward (eastward motion in the evening sector) or remain stationary, depending on the momentum contrast between the LLBL and CPS. If the surge velocities that were observed in §3.8 are mapped to the LLBL/CPS interface using the mapping model described earlier in this chapter (§4.2), then typical earthward phase velocities of the KHI are between  $\approx 30$  km/s and  $\approx 130$  km/s. If it is assumed that the plasma density either side of the LLBL/CPS interface is approximately equal, then these phase velocities correspond to a difference in the magnitude of flow velocity between the LLBL and CPS ranging from  $\approx 60$  km/s to  $\approx 250$  km/s.

As with surge multiplicity, the Near Earth Neutral Line model does not yet have a readily available explanation of the observed features of substorm spreading. However, Birn and Hones (1981) have shown with numerical modelling that changes occur in the width of the near earth neutral line. These changes could manifest themselves as movements of the western and eastern boundaries of surge activity in the auroral oval.

#### 4.5 : Concluding Remarks

The basic characteristics of where and how often surges occur in the evening sector have been compiled from 100 orbital passes of the VIKING satellite over the northern auroral oval. Cross referencing of

surges, defined as UV forms on the VIKING images, with groundbased magnetometer data did not yield conclusive correlations between these two ways of defining surges. More detailed work needs to be carried out on these correlations, particularly work regarding exactly from what altitude the UV emissions viewed by VIKING originate. Also, intensity calibrations relating UV intensities to optical intensities need to be repeated for a variety of observations (only one such study has so far been conducted) before any firm conclusions can be drawn from the nature of ground-satellite correlation studies.

The result of finding the 2300-2400 MLT zone to be the most likely zone in which to find surges in the evening sector was found to be in agreement with earlier analysis of substorm events (discussed in §4.3). This fact lends validity to the definition of a surge as set out in chapter 3 (§3.2) which permitted a surge to have a much smaller scale size than in any previous study. Also by the same token, the intensity threshold that had been set subjectively appears to have been a reasonable choice. The result that surges occur as isolated features only  $\approx 35\%$  of the time is new. No westward travelling surges were found to travel over large distances along the auroral oval, but cases where an active region expanded westward were observed. This could have been what had previously been interpreted as a westward travelling surge.

Explanations of the results are possible with either the Boundary Layer Dynamics model or Near Earth Neutral line model of magnetospheric substorms. However, the BLD explanation of surge multiplicity and distribution arises quite naturally from the model, whereas the Near Earth Neutral Line model cannot yet fully address many of the issues raised by the results.



## REFERENCES

- Akasofu, S. -I., The development of the auroral substorm, *Planet. Space Sci.*, 12, 273, 1964.
- Anger, C. D., S. K. Babey, A. Lyle Broadfoot, R. G. Brown, L. L. Cogger, R. Gattinger, J. W. Haslett, R. A. King, D. J. McEwen, J. S. Murphree, E. H. Richardson, B. R. Sandel, K. Smith and A. Vallance Jones, An auroral imager for the VIKING spacecraft, *Geophys. Res. Lett.*, 14, 378, 1987.
- Axford, W. I., Magnetic field reconnection, *Magnetic reconnection in space and laboratory plasmas*, ed. E. W. Hones Jr., AGU monograph # 30, 1984.
- Axford, W. I., H. E. Petscheck and G. L. Siscoe, Tail of the magnetosphere, *Geophys. Res. Lett.*, 70, 1231, 1965.
- Axford, W. I. and C. O. Hines, A unifying theory of high latitude geophysical phenomena and geomagnetic storms, *Can. J. Phys.*, 39, 1433, 1961.
- Baumjohann, W. and G. Haerendel, in *Solar Wind - Magnetosphere Coupling*, page 415, ed. Y. Kamide and J. Slavin, Terra. Scientific. Pub., Tokyo 1986.
- Beynon, J. D. E. and D. R. Lamb, *Charge-coupled Devices and their Applications*, McGraw Hill, 1980.
- Brandt, J. C., *The Solar Wind*, Freeman and Co., San Francisco, 1970.
- Burch, C. R., Reflecting Microscopes, *Proc. Phys. Soc.*, 59, 41, 1947.
- Chapman, S. and V. C. A. Ferraro, A new theory of magnetic storms, *Terr. Mag. Atmos. Elect.* 36, 77, 1931.
- Clauer, C. R. and R. L. McPherron, Mapping the local time - universal time development of magnetospheric substorms using midlatitude magnetic observatories, *J. Geophys. Res.*, 79, 2811, 1974.
- Dobrin, M. B., in *Introduction to Geophysical Prospecting*, page 449, McGraw Hill, New York, 1988.
- Dungey, J. W., Interplanetary magnetic field and the auroral zones, *Phys. Rev. Lett.*, 6, 47, 1961.
- Fairfield, D. H., Structure of the magnetotail, in *Magnetotail Physics*, ed. A. T. Y. Lui, Johns Hopkins University Press, Baltimore 1987.

Frank, L. A. and J. D. Craven, Imaging results from Dynamics Explorer I, *Rev. of Geophys.*, 26, 249, 1988.

Hakura, Y., Tables and maps of geomagnetic coordinates corrected by higher order spherical harmonic terms, *Rept. Ionos. Space Res. Japan*, 19, 121, 1965.

Hines, C. O., The upper atmosphere in motion, in *The Upper Atmosphere In Motion*, page 14, AGU monograph # 18, Washington, D.C., 1974.

Hones, E. W. Jr., Plasma sheet behaviour during substorms, in *Magnetic Reconnection in Space and Laboratory Plasmas*, ed. E. W. Hones Jr., AGU monograph # 30, 1984.

Howes, M. J. and D. V. Morgan, *Charge Coupled Devices and Systems*, John Wiley and Sons, 1979.

Hundhausen, A. J., Step One : Solar activity in the solar wind (Abstract), *Eos*, 70, 442, 1989.

Hunten, D. M., F. E. Roach and J. W. Chamberlain, A photometric unit for the airglow and aurora, *J. Atmos. and Terra. Phys.*, 8, 345, 1956.

Kawasaki, K. and G. Rostoker, Auroral motions and magnetic variations associated with the onset of geomagnetic substorms, *J. Geophys. Res.*, 84, 7113, 1979.

Kan, J. R. and W. Sun, Simulation of the westward travelling surge and Pi2 pulsations during substorms, *J. Geophys. Res.*, 90, 10911, 1985.

Kan, J. R., L. Zhu and S. -I. Akasofu, A theory of substorms : onset and subsidence, *J. Geophys. Res.*, 93, 5624, 1988.

Kisabeth, J. L. and G. Rostoker, The expansive phase of magnetospheric substorms, 1. Development of the auroral electrojets and auroral arc configuration during a substorm, *J. Geophys. Res.*, 79, 972, 1974.

Lui, A. T. Y., D. Venkatesan, G. Rostoker, J. S. Murphree, C. D. Anger, L. L. Cogger and T. A. Potemra, Dayside auroral intensifications during an auroral substorm, *Geophys. Res. Lett.*, 14, 415, 1987.

Miura, A., Anomalous transport by magnetohydrodynamic Kelvin-Helmholtz instabilities in the solar wind - magnetosphere interaction, *J. Geophys. Res.*, 89, 801, 1984.

Mozer, F. S., C. W. Carlson, M. K. Hudson, R. B. Torbert, B. Parady, J. Yatteau and M. C. Kelly, Observations of paired electrostatic shocks in the polar magnetosphere, *Phys. Rev. Lett.*, 38, 292, 1977.

Montbriand, L. E., A simple method for calculating the local time of corrected geomagnetic midnight, *J. Geophys. Res.*, 75, 5634, 1970.

Neugebauer, M. and C. W. Snyder, Mariner 2 measurements of the solar wind, in *The Solar Wind*, page 3, ed. R. J. Mackin and M. Neugebauer, Pergamon Press, Oxford, 1964.

Nicholson, D. R., *Introduction to Plasma Theory*, John Wiley and Sons, 1983.

Parker, E. N., *Interplanetary Dynamical Processes*, John Wiley and Sons, 1963.

Press, W. H., B. P. Flannery, S. A. Teukolsky and W. T. Vetterling, in *Numerical Recipes*, page 509, Cambridge University Press, 1987.

Pytte, T., R. L. McPherron and S. Kokubun, The ground signatures of the expansive phase during multiple onset substorms, *Planet. Space Sci.*, 24, 1115, 1976.

Rajaram, G., G. Rostoker and J. C. Samson, Wave characteristics of Ps6 magnetic variations and their implications for convective flow in the magnetotail, *Planet. Space Sci.*, 34, 319, 1985.

Roelof, E. C., Energetic neutral atom image of a storm time ring current, *Geophys. Res. Lett.*, 14, ,1987.

Romana, A. and J. O. Cardus, *J. Phys. Soc. Japan*, 17, suppl A-II, 1962.

Rostoker, G., Geomagnetic Indices, *Rev. Geophys. Space Phys.*, 10, 935, 1972.

Rostoker, G., Competing models of auroral substorm processes, *Proceedings of the 1988 Chapman Auroral Physics Conference, Cambridge*, in press, 1989.

Rostoker, G., S. -I. Akasofu, J. Foster, R. A. Greenwald, Y. Kamide, K. Kawasaki, A. T. Y. Lui, R. L. McPherron and C. T. Russell, Magnetospheric substorms - definitions and signatures, *J. Geophys. Res.*, 85, 1663, 1980.

Rostoker, G. and J. C. Samson, Can substorm expansive phase effects and low frequency Pc magnetic perturbations be attributed to the same source mechanism? *Geophys. Res. Lett.*, 11, 251, 1984.

Rostoker, G. and T. D. Phan, Variation of the auroral electrojet spatial location as a function of the level of magnetospheric activity, *J. Geophys. Res.*, 91, 1716, 1986.

Rostoker, G., S. -I. Akasofu, W. Baumjohann, Y. Kamide and R. L. McPherron, The roles of direct energy input of energy from the solar wind and unloading of stored magnetotail energy in driving magnetospheric substorms, *Space Sci. Rev.*, 46, 93, 1987.

Rostoker, G. and T. Eastman, A boundary layer model for magnetospheric substorms, *J. Geophys. Res.*, 92, 12187, 1987.

Russell, C. T. and R. C. Elphic, ISEE observations of flux transfer events at the dayside magnetopause, *Geophys. Res. Lett.*, 6, 33, 1979.

Salingaros, N. A., An ammended magnetohydrodynamic equation which predicts field-aligned current sheets, *Astrophys. and Space Sci.*, 137, 385, 1987.

Sergeev, V. A., Longitudinal localisation of the substorm active region and changes during the substorm, *Planet. Space Sci.*, 1341, 1974.

Singleton, R. C., An algorithm for computing the mixed radix fast Fourier transform, *I.E.E.E. Trans. Audio Electron*, AU-17, 93, 1969.

Slavin, J. A., E. J. Smith, D. G. Sibeck, D. N. Baker, R. D. Zwickl and S. -I. Akasofu, An ISEE 3 study of average and substorm conditions in the distant magnetotail, *J. Geophys. Res.*, 90, 875, 1985.

Stern, D. P. and I. I. Alexeev, Where do field lines go in the quiet magnetosphere ? *Rev. of Geophys.*, 26, 782, 1988.

Thompson, W. B., Parallel electric fields and shear instabilities, *J. Geophys. Res.*, 88, 4805, 1983.

Tighe, W. G. and G. Rostoker, Characteristics of westward travelling surges during magnetic substorms, *J. Geophys.*, 50, 51, 1981.

Tysganenko, N. A., Global quantitative models of geomagnetic field in the cislunar magnetosphere, *Planet. Space Sci.*, 35, 1347, 1987.

Vallance Jones, A., *Aurora*, D. Reidel, Dordrecht, Holland, 1974.

Vallance Jones, A., R. L. Gattinger, F. Creutzberg, R. A. King, P. Prikrýl, L. L. Cogger, D. J. McEwen, F. R. Harris, C. D. Anger, J. S. Murphree and R. A. Koehler, A comparison of CANOPUS ground optical data with images from the VIKING UV camera, *Geophys. Res. Lett.*, 14, 391, 1987.

Walker, A. D. M., The Kelvin-Helmholtz instability in the low latitude boundary layer, *Planet. Space Sci.*, 29, 1119, 1981.

Wiens, R. G. and G. Rostoker, Characteristics of the development of the westward electrojet during the expansive phase of magnetospheric substorms, *J. Geophys. Res.*, 80, 2109, 1975.

## APPENDIX I : DEFINITIONS AND GLOSSARY

### PART 1 : DEFINITIONS OF COORDINATE SYSTEMS

#### *Geocentric Solar Magnetospheric*

The X axis points from the centre of the earth to the sun. The Y axis is perpendicular to the earth's magnetic dipole axis, chosen so that the Z axis completes the orthogonal set by pointing into the hemisphere that contains the geographic north pole.

#### *Geomagnetic Coordinates*

Geomagnetic latitude and longitude are defined about a point at the centre of the earth and a Z axis parallel to the magnetic dipole axis. Zero degrees longitude is defined as the meridian passing through the geographic north pole and Thule, Greenland, where the magnetic dipole axis intersects the surface of the earth. Using the International Geomagnetic Reference Field 1965.0, the dipole axis has a geographic colatitude of  $11.4^{\circ}$  N and a longitude of  $69.8^{\circ}$  W.

#### *Corrected Geomagnetic Coordinates*

This coordinate system takes into account higher order multipole components of the earth's magnetic field and makes corrections to the geomagnetic coordinate system. Hakura (1965) has calculated these corrections.

### *Magnetic Local Time*

Magnetic local time at a given Universal Time, at a point on the earth, is defined in terms of the angle between two planes. One plane passes through the point and the axis of uniform magnetisation and the other passes through the axis of uniform magnetisation and the sun. MLT is normally within  $\pm \frac{1}{2}$  an hour of local time. Montbriand (1970) details precisely how to determine the MLT of a any point on the earth at any time.

## PART 2 : GLOSSARY

### *Alfvén velocity, $V_A$*

is defined algebraically by  $V_A^2 = \frac{B^2}{2\mu_0}$ . Where B is the magnetic field strength. It is an important plasma parameter because  $V_A$  is the maximum velocity at which information can be transmitted by magnetic fluctuations in a magnetised plasma.

### *Debye Length, $\lambda$*

The Debye, or shielding, length in a plasma is the distance beyond which electric fields are screened. It is defined by

$$\lambda^2 = \frac{\epsilon_0 k T}{n_0 e^2}$$

where k is Boltzmann's constant, T is the temperature,  $n_0$ , for a neutral plasma, is the electron or ion density and e is the

electron charge.

*Electron - Ion Collision Frequency,  $\nu_c$*

is the inverse of the time between collisions of an electron with ions. For small scattering angle collisions,

$$\nu_c = \frac{n_o e^4 z_i^2 \ln \Lambda}{2\pi \epsilon_o m_e^2 v_o^3}$$

where  $n_o$  is the density of scattering centres (ions),  $z_i$  is the charge state of the ions,  $\Lambda$  is the plasma parameter (q.v.),  $m_e$  is the electron mass and  $v_o$  is the electron velocity.

*Electron Plasma Frequency,  $\omega_e$*

is the frequency at which electrons perform collective simple harmonic motion about a distribution of ions.

$$\omega_e^2 = \frac{n_o e^2}{\epsilon_o m_e}$$

where  $n_o$ , for a neutral plasma is the density of ions or electrons,  $e$  is the electron charge and  $m_e$  is the electron mass.

*Gyroradius,  $r_s$*

The gyroradius is the radius of a circle, projected onto a plane perpendicular to the magnetic field, of the motion of a species  $s$  when it has a component of its velocity perpendicular to a magnetic field.

$$r_s = \frac{m_s v_{s\perp}}{q_s B_o}$$

where  $B_o$  is the scalar magnitude of the average magnetic field.  $m_s$ ,  $v_{s\perp}$ , and  $q_s$  are the mass, velocity perpendicular to  $B_o$  and charge of species  $s$  respectively.

### *Guiding centre*

Individual particle motions of the constituents of a plasma are complicated. Under some circumstances, it can be useful to think of the total motion as being composed of circular or gyrational motion about a point (the guiding centre) together with the motion of the guiding centre.

### *Neutral Line*

The separator line in the midplane of the magnetotail that separates the regions where field lines originating from the Earth either close or do not close in the Central Plasma Sheet.

### *Plasma Parameter, $\Lambda$*

is defined as the number of particles in a cube with a dimension of the Debye length.

### *Rayleigh, R*

A unit of photometry commonly used in the study of aurora and airglow.  $1R \equiv 10^6$  quanta per  $\text{cm}^{-2}$  per sec (per column). The 'per



column' is specified in the original paper defining the *Rayleigh* by Hunten et al. (1956). It is inserted to indicate that the quantity actually measured when determining auroral intensity is a volume emissivity rate (modified by absorption effects), integrated along a column along the line of sight from a detector.

## APPENDIX II : MHD EQUATIONS

### II.1 : Introduction

The fluid treatment of plasmas enables an alternative description to the individual particle model of plasmas. Where the latter model concentrates on the kinetics of the plasma population, the fluid model treats the plasma as two interpenetrating fluids : an electron fluid and an ion fluid. The gain advantage in using such a fluid description is that the number of independent variables required to describe the plasma is decreased, leading to a reduction in the complexity of describing the plasma and its behaviour. This gain is balanced on the other hand by realising velocity dependent effects cannot be treated and that the fluid approach does not apply to all plasma regimes.

In very general terms, derivation of the fluid equations centres on taking velocity moments of the kinetic equation (also known as the Boltzmann equation), which in turn describes the evolution of a distribution function  $f_s(r,v,t)$ , where  $s$  is the species of particles (electrons or ions),  $r$  is position,  $v$  is velocity and  $t$  is time.  $f_s$  can be interpreted as being the number of particles in a differential element of six dimensional phase space  $drdv$ , located at  $(r,v)$  and normalised by that same volume of phase space. When the equations resulting from taking the first two velocity moments of the kinetic equation are combined with Maxwell's equations, a unique solution to the arguments of the distribution function  $(r,v,t)$  can be found. This

approach is described in many books that give an introduction to the treatment plasmas and the outline given here follows that of Nicholson (1983)

In order to justify using a fluid description of plasma, some criterion is necessary for deciding when collective effects, as opposed to collisional effects between particles, dominate the plasma behaviour. This occurs when

$$\frac{\nu_c}{\omega_e} \approx \frac{1}{\Lambda} \quad (\text{Eqn II.1})$$

where  $\nu_c$  is the electron - ion collision frequency,  $\omega_e$  is the *electron plasma frequency* and  $\Lambda$  is the *plasma parameter*. Furthermore, a fluid description is only valid when it is describing phenomena of characteristic frequency  $\omega$  such that  $\nu_c \ll \omega$ .

## II.2 : Development of the MHD Equations

The kinetic equation is

$$\frac{\partial f_s(r, v, t)}{\partial t} + v \cdot \nabla f_s(r, v, t) + \frac{F}{m_s} \cdot \nabla_v f_s(r, v, t) = \left[ \frac{\partial f_s(r, v, t)}{\partial t} \right]_{\text{coll}}$$

(Eqn II.2)

where  $F = q (E + v \times B)$  the Lorentz force, with  $E$  and  $B$  the *average*

electric and magnetic fields respectively, and  $m_s$  is the mass of the plasma species. The term on the right hand side of this equation represents the time rate of change of the distribution function due to collisional effects.

By integrating equation II.2 over all of velocity space and neglecting the collision terms, which are assumed to be small, the continuity equation is recovered, viz

$$\frac{\partial n_s(r,t)}{\partial t} + \nabla \cdot [V_s n_s(r,t)] = 0 \quad (\text{Eqn II.3})$$

where  $n_s(r,t)$  is the number of particles (of species  $s$ ) per unit volume inside an elemental volume of space at position  $r$  and time  $t$  and  $V_s$  is the velocity of the fluid.

Multiplication of equation II.2 by  $v$  and then integration over all of velocity space leads to the momentum equation, also sometimes called the force equation.

$$m_s n_s(r,t) \left( \frac{\partial V_s}{\partial t} + [V_s \cdot \nabla] V_s \right) = - \nabla P_s + q_s n_s(r,t) \left( E + V_s \times B \right) + K_s(r) \quad (\text{Eqn II.4})$$

where  $P_s$  is the gas pressure for species  $s$  and  $K_s(r)$  is a term representing collisions. Nicholson gives arguments to show that  $K_e(r)$

$= -K_i(r)$ , where the subscripts e and i refer to the cases of electron and ion fluid respectively.

Until now, the plasma has been treated as a two fluid mixture. By defining a combined mass density  $\rho_H = m_e n_e + m_i n_i$ , centre of mass velocity  $V = (m_i n_i V_i + m_e n_e V_e) / \rho_H$ , current density  $J = q_i n_i V_i + q_e n_e V_e$  and total pressure  $P = P_i + P_e$  of both fluids, various linear combinations of equations II.3 and II.4 for both electrons and ions then lead to

$$\frac{\partial \rho_H}{\partial t} + \nabla \cdot (\rho_H V) = 0 \quad (\text{Eqn II.5})$$

which is the equation of mass conservation,

$$\frac{\partial \rho_c}{\partial t} + \nabla \cdot J = 0 \quad (\text{Eqn II.6})$$

which is the charge conservation law where  $\rho_c$  is the charge density, and

$$\rho_H \frac{dV}{dt} = -\nabla P + \rho_c E + J \times B \quad (\text{Eqn II.7})$$

which is the momentum equation. For a neutral fluid, this is simplified further by setting  $\rho_c = 0$ . Finally, the last equation to complete the set of MHD equations is called the generalised Ohm's law and is

$$\frac{m_e m_i}{\rho_H e^2} \frac{\partial J}{\partial t} = \frac{m_i}{2\rho_H e} \nabla P + E + V \times B - \frac{m_i}{\rho_H e} J \times B - \frac{J}{\sigma}$$

(Eqn II.8)

where  $e$  is the magnitude of the electronic charge and  $\sigma$  is the conductivity. When only the dominant terms of this equation are taken, then equation II.8 reduces to  $J = \sigma E$ .

When combined with Maxwell's equations

$$\nabla \times E = - \frac{\partial B}{\partial t} \quad \text{and} \quad \nabla \times B = \mu_0 J + \mu_0 \epsilon \frac{\partial E}{\partial t}$$

where  $\epsilon = \epsilon_0 (1 + v_A^2 / c^2)$ , equations II.5 to II.8 form a complete set of equations with as many equations as unknowns.

Further simplifications and approximations can be made, namely for equation II.8, if the time variations of  $J$  are small; the temperature low enough so that the  $\nabla P$  term can be ignored; the current small enough so that the  $J \times B$  term is much smaller than the  $V \times B$  term and  $\sigma \rightarrow \infty$  for a collisionless plasma, then equation II.8 becomes

$$E = - V \times B \quad \text{(Eqn II.9)}$$

Under these *ideal* MHD conditions, the complete set of equations becomes

$$\frac{\partial \rho_H}{\partial t} + \nabla \cdot (\rho_H \mathbf{V}) = 0 \quad (\text{Eqn II.10})$$

$$\rho_H \frac{d \mathbf{V}}{d t} = - \nabla P + \mathbf{J} \times \mathbf{B} \quad (\text{Eqn II.11})$$

$$\nabla \times \left[ \mathbf{V} \times \mathbf{B} \right] = \frac{\partial \mathbf{B}}{\partial t} \quad (\text{Eqn II.12})$$

$$\nabla \times \mathbf{B} = \mu_0 \mathbf{J} \quad (\text{Eqn II.13})$$

Equation II.9 implies *frozen field* (Axford, 1984), so that under ideal MHD conditions one can think of the plasma being tied to magnetic field lines so that when the field moves, it will take the plasma with it.

## APPENDIX III : 2-D Spatial Fourier Transforms

### III.1 : Introduction

Many of the ideas and techniques used in calculating and working with 1-D Fourier transforms (FT's) can be carried over into higher dimensions. For example, the need to remove linear trends from data and the need to pad data out to the nearest integer power of 2 when Fast Fourier Transform (FFT) algorithms are used to evaluate the transforms apply equally well to any dimension of Fourier transform. However, one of the major differences between 1-D and higher dimensions of transforms is that the interpretation of the latter is much more difficult.

For the 2-D FT's calculated as part of the work for this thesis, a number of steps were taken before the transforms were actually calculated and these were as follows. Linear trends in the data were removed. The data were windowed and then multiplied by a comb function before being padded; then finally the 2-D FT was calculated. For an image consisting of a set of points  $I(x,y)$ ,  $0 \leq x \leq N_1-1$ ,  $0 \leq y \leq N_2-1$ , each of these steps is explained in detail below.

### III.2 : Removal of Linear Trends

In order to determine any linear trends in the set of image points  $I(x,y)$ , the best fitting plane  $z = Ax + By + C$ , was found. The



coefficients A, B and C were determined by the method of least squares as follows. (Based on a method given by Dobrin (1988).)

$R(x,y)$  is defined as the residual function which yields the difference between a general plane passing through a set of image points and the image points themselves :

$$R(x,y) = I(x,y) - z$$

$$R(x,y) = I(x,y) - (Ax + By + C)$$

A measure of how good a fit the plane is can be obtained by calculating the quantity  $\sum_{x,y} R^2(x,y)$ . The smaller this quantity is, the better the fit of the plane through the image. In order to find the best fitting plane,  $\sum_{x,y} R^2(x,y)$  must be minimised with respect to A, B and C :

$$\sum_{x,y} \frac{\partial}{\partial K_j} \left[ R^2(x,y) \right] = 0 \quad , \quad K_j = A, B \text{ and } C \text{ in turn.}$$

Working now only with  $K_j = A$  and dropping the x,y terms on the summations, which are now all assumed to be the double sums  $\sum_{x=0}^{N-1} \sum_{y=0}^{N-1}$

we get

$$\sum \frac{\partial}{\partial A} \left[ R^2(x,y) \right] = 0$$

$$2 \sum R(x,y) \frac{\partial}{\partial A} R(x,y) = 0$$

which implies the  $\sum$  term must = 0. Now,

$$R(x,y) \frac{\partial}{\partial A} R(x,y) = -x \left[ I(x,y) - (Ax + By + C) \right]$$

and so the minimisation requirement with respect to A becomes

$$\sum Ax^2 + \sum Bxy + \sum Cx = \sum I(x,y) x$$

similarly, when  $K_j = B$  then  $C$ , two further equations are obtained :

$$\sum Axy + \sum By^2 + \sum Cy = \sum I(x,y) y$$

$$\sum Ax + \sum By + \sum C = \sum I(x,y)$$

This set of equations can be rewritten in matrix form :

$$\begin{bmatrix} \sum x^2 & \sum xy & \sum x \\ \sum xy & \sum y^2 & \sum y \\ \sum x & \sum y & N_1 N_2 \end{bmatrix} \begin{bmatrix} A \\ B \\ C \end{bmatrix} = \begin{bmatrix} \sum I(x,y)x \\ \sum I(x,y)y \\ \sum I(x,y) \end{bmatrix}$$

The solution to this matrix equation requires the 3 x 3 matrix on the left hand side of the equation to be inverted. Unfortunately, the standard methods of matrix inversion (e.g. Gauss - Jordan elimination and LU decomposition) do not work well with this matrix because it is close to being singular due to the relative sizes of its elements : the  $N_1 N_2$  term is much smaller than any of the other matrix elements. The method of matrix inversion that was adopted - single value decomposition - was that suggested by Press et. al (1987) and is often used to invert matrices that result from the least squares approach to the modelling of data. Press et al. also present a FORTRAN routine to perform the matrix inversion and so made it possible to find the values of A, B and C.

Once the constants A, B and C had been determined for the best fitting plane through a set of image points, it was a simple matter to

subtract the plane  $z = Ax + By + C$  from the image.

### III.3 : Windowing The Image Data

As with 1-D transforms, windowing of data is necessary to reduce contamination of the Fourier transform with frequencies associated with the replication frequency of the data. A commonly used window in 1-D is the cosine bell function, also known as the Hamming window function. For the image  $I(x,y)$  as defined in section III.1 of this appendix, this function modifies  $I(x,y)$  according to

$$I^*(x,y) = I(x,y) \left[ \frac{1}{2} \left[ 1 - \cos \left( \frac{2\pi x}{N_1-1} \right) \right] \right] \left[ \frac{1}{2} \left[ 1 - \cos \left( \frac{2\pi y}{N_2-1} \right) \right] \right]$$

This 2-D function tapers the data smoothly to zero all around its perimeter, but it also affects the Fourier transform in a number of ways. By multiplying image data in the spatial domain by a function, the Fourier transform of the modified data is the convolution of the transform of the original data with the transform of the function. (This is just another way of stating the convolution theorem.) Also affected is the amplitude of peaks in the transform associated with periodicity in the original data. For well behaved data and window functions, these effects are small and were neglected in the final analysis of the transforms.

### III.4 : Frequency Shifting of Fourier Transforms

When the 2-D Fourier transform of a rectangular (or square) image is computed using standard FFT routines, the results of the transform in the Fourier domain are ordered in a slightly peculiar way, as shown in figure III.1 To make interpretation of the transforms easier, it is useful to make their (zero frequency) origins occur in the middle of the transform. This is done by a shift of origin, but the shift of origin is applied to the data *before* being transformed rather than trying to unravel and shift the transform itself. In order to achieve this shift of origin, the data are multiplied in the spatial domain by a function of unit amplitude that is at the Nyquist frequency of the data (which is half the spatial sampling frequency of the data). By the convolution theorem, this corresponds to shifting the transform in the positive direction along both axes by the Nyquist frequency, which is exactly the shift required to locate the origin of the transform in the middle of the output and produce what is called the optical transform of the data.

The function used to multiply the data and cause a shift of the Nyquist frequency in 1-D resembles a comb. In two dimensions, the function modifies the data according to  $I^*(x,y) = I(x,y) (-1)^{(x+y)}$ .

### III.5 : Calculating the 2-D Fourier Transform

The two dimensional Fourier transform of a function  $I(x,y)$ ,  $\mathcal{I}(m,n)$  can be defined in many ways, so long as the inverse (or reverse) transform is defined and normalised in such a way that the

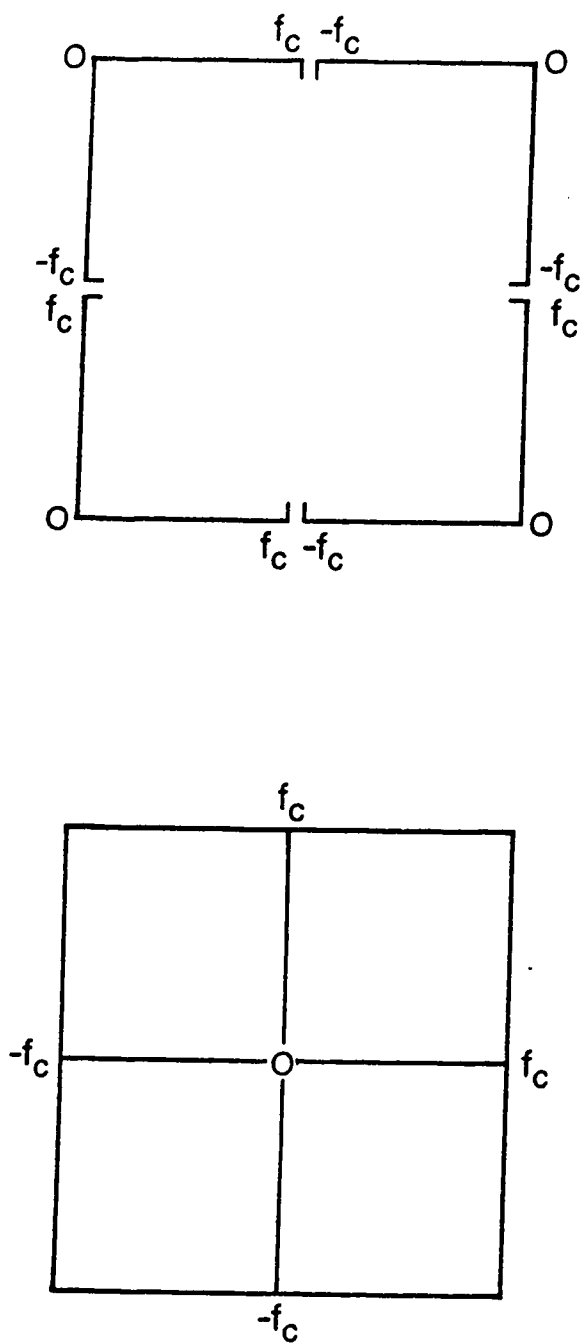


Figure III.1 : Arrangement of 2-D Fourier transform data before and after the coordinate shift is applied.  $f_c$  is the Nyquist frequency.

(forward) transform and its inverse form a transform pair. In the work conducted for this thesis, only forward transforms were required and so inverse transforms were not needed. The forward transform was defined as

$$I(m,n) = \sum_{x=0}^{N_1-1} \sum_{y=0}^{N_2-1} I(x,y) e^{2\pi i m x / N_1} e^{2\pi i n y / N_2}$$

It can be shown (e.g. see Press et al.) that the 2-D transform can be thought of as the 1-D Fourier transform of each row in the image being calculated, then taking the 1-D Fourier transform along each of the columns (which now contain the results of the first set of FT's) being calculated. As long as the length of the rows and columns is an integer power of 2 (which often requires padding of data with zeros to the next integer power of 2 in length), then all the required 1-D transforms can be calculated using the FFT algorithm. This indeed was the method employed by the FORTRAN subroutines that were used as part of the analysis and they were taken from the public domain, IBM written, Scientific Subroutines Package.